The Pennsylvania State University

The Graduate School

Intercollege Program in Materials Science and Engineering

POLARIZATION ORIENTATION DEPENDENCE OF PIEZOELECTRIC LOSS AND PROPOSED CRYSTALLOGRAPHIC CHARACTERIZATION METHODOLOGY

A Dissertation in

Materials Science and Engineering

by

Minkyu Choi

Submitted in Partial Fulfillment
of the Requirements
for the Degree of

Doctor of Philosophy

December 2018

The dissertation of Minkyu Choi was reviewed and approved* by the following:

Kenji Uchino
Professor of Electrical Engineering
Dissertation Advisor
Chair of Committee

Clive A. Randall
Professor of Materials Science and Engineering

Susan E. Trolier-McKinstry
Professor of Materials Science and Engineering

Wenwu Cao
Professor of Mathematics

Suzanne Mohney
Professor of Materials Science and Engineering
Intercollege Graduate Degree Program Chair

*Signatures are on file in the Graduate School

ABSTRACT

Piezoelectric materials are widely utilized in small devices, and low loss is essential for further miniaturization with desired power density. Due to large piezoelectric loss, the mechanical quality factor of $Pb(Zr,Ti)O_3$ (PZT) ceramics at antiresonance frequency is much higher than the one at resonance frequency. Thus, driving the piezoelectric resonator at the antiresonance frequency is recommended to reduce the required electric power for generating the same level of mechanical vibration. Unfortunately, piezoelectric loss has not been studied intensively, and the physical origin is yet unclear. Assuming the origin of loss is from domain dynamics, it is essential to understand the piezoelectric loss behavior by polarization orientation.

The change in the piezoelectric loss factors by polarization orientation was investigated using a conventional characterization method with effective k_{31} and k_{33} mode structures. 1% Nb-doped PZT ceramics (PNZT) were prepared in tetragonal rhombohedral and MPB structure with 0, 15, 30, 45, 60, 75 and 90 degree polarization angles in collaboration with PI Ceramics, Germany. As a result, it was determined that the intensive piezoelectric loss increases more than intensive dielectric and elastic losses by angling the polarization. However, two serious issues were found in the k_{33} structure with small motional capacitance, which are:

1. Large relative error from indirect calculation and large structural impedance of the k_{33} rod.

2. Error in 3dB method used to define the mechanical quality factor.

Consequently, a new analysis procedure to obtain anisotropic loss tensors is proposed using effective vibration modes of ceramic bar with canted polarization. The proposed methodology contains 1) off-resonance dielectric measurements, 2) effective k_{31} mode analysis, 3) off-resonance d_{33} measurements and 4) effective k_{15} mode analysis. The effective k_{31} and k_{15} vibration mode should be separated from other modes to use the method.

A bandwidth between maximum and minimum susceptance and reactance, which is known as the quadrantal bandwidth, is suggested as the half-power bandwidth to determine the mechanical quality factors at resonance and antiresonance, respectively. ATILA/FEA (Micromechatronics Inc., PA, USA) simulation was made with the change of piezoelectric *d* constant. The new method showed better accuracy of the quality factor and loss determination especially in the low coupling condition.

The independent intensive properties of prepared PNZT are obtained with the suggested methodology. Piezoelectric loss showed larger anisotropy in all structures compared to the dielectric or elastic loss. Using the rotation matrix, polarization angle dependent effective properties were calculated. Although the elastic and piezoelectric properties differ from the result obtained with the conventional method, the piezoelectric loss showed the largest changes by canting the polarization.

Considering 3-dimensionally clamped and electrically open-circuited condition of material, extensive loss parameters were additionally obtained. Negative extensive piezoelectric loss was discovered in a tetragonal PNZT with largely angled polarization and electric field, for both k_{31} and k_{15} vibration mode. In is known that positive piezoelectric loss is considered to compensate the dielectric and elastic losses, thus the heat generation under anti-resonant drive is less than the one under resonant drive when the piezoelectric loss is large. The negative extensive piezoelectric loss contributes to the overall phase lag, which could be observed in the contribution of extensive loss factors to the intensive elastic loss.

The negative piezoelectric loss may be related with the domain wall dynamics and could motivate theoretical physicists to a new understanding.

TABLE OF CONTENTS

LIST OF FIGURES

LIST OF TABLES

ACKNOWLEDGEMENTS

Foremost, I would like to express my deepest gratitude to my advisor, Dr. Kenji Uchino for his invaluable support and guidance. He has been a great academic and personal mentor all along and was always available when I needed his advice or encouragement. It was a great honor and pleasure to learn from him. I would also like to thank the Office of Naval Research for supporting this study with their funding through Dr. Kenji Uchino.

I would like to extend my sincere appreciation to my Ph.D. dissertation committee members: Dr. Susan Trolier-McKinstry, Dr. Clive A. Randall and Dr. Wenwu Cao, for their valuable comments and suggestions. Their critiques and encouragements made this dissertation possible.

I greatly appreciate Mr. Eberhard Hennig and Dr. Timo Scholehwar from PI Ceramics for providing the piezoelectric ceramics and having great discussions whenever I needed.

I am also grateful to my ICAT colleagues: Dr. Erkan Gurdal, Dr. Husain Shekhani, Tianning Liu, Dr. Weijia Shi, Dr. Jong-Kyu Park, Dr. Lei Qin, Dr. Yuting Ma, Dr. Xiao-Xiao Dong, Dr. Tao Yuan, Dr. Shengjun Shi, Dr. Sinan Dursun, Maryam Majzoubi and Anushka Bansal for their support, feedback, cooperation and friendship. I would also like to thank my current ICAT colleagues: Hossein Daneshpajooh and Yoon-Sang Park, for their stimulating discussions and the sleepless nights we've spent.

Last but not the least, I would like to thank my family: my dad Seung-Bok Choi, my mom Yeon-Ok Kim and my sister Karen Choi for their incredible support and warm love. Thank you, my sons Aaron and Aiden, for filling love in my heart. And beyond all, I would like to thank my wife Yeon Hee Wang for standing by me through all these years and giving me strength when needed.

Chapter 1

Background

1.1 Piezoelectricity

The piezoelectric effect is a linear conversion effect between mechanical and electrical energy. The direct effect was discovered by Pierre and Jacques Curie in 1880 [1] and the converse effect was demonstrated by Gabriel Lippmann in 1881 [2]. In 1947, Shepard Roberts observed longitudinal and transverse piezoelectricity in electrically-poled $BaTiO_3$ polycrystalline ceramics [3]. With following studies on similar perovskite ABO_3 structures, $Pb(Zr,Ti)O_3$ (PZT) was developed in 1954 by Bernard M. Jaffe [4]. With high piezoelectricity and Curie temperature, PZT-based ceramics have been widely utilized in various applications [5]–[11].

Piezoelectricity originates from the symmetry of crystalline matter. Under applied stress (*X*), the uneven displacement of cations and anions results in charge development (dielectric displacement, *D*), that is the direct piezoelectric effect. Under an applied electric field (*E*), the equilibrium position of the positively (anions) and negatively charged atoms (cations) changes leading to elastic deformation (strain, *x*), that is converse piezoelectric effect [12].

Assuming only temperature (*T*), entropy (*S*), *E, D, X*, and *x* determines the thermal, dielectric and elastic behavior of the piezoelectric materials, the differential forms of thermodynamic potentials can be expressed using the following equations, where *U* is the internal energy, *H* the enthalpy, *A* the Helmholtz free energy and *G* the Gibbs free energy [13].

$$dU = TdS + EdD + Xdx \tag{1.1.1}$$

$$dH = TdS - DdE - xdX \tag{1.1.2}$$

$$dA = -SDT + EdD + Xdx \tag{1.1.3}$$

$$dG = -SDT - DdE - xdX \tag{1.1.4}$$

Assuming infinitesimal change of properties, linear equations of state can be considered. To discuss intensive properties which are scale invariant, assume *T*, *X* and *E* are independent variables. Then, the appropriate thermodynamic potential is the Gibbs free energy and the variables become:

$$-S = \left(\frac{\partial G}{\partial T}\right)_{X,E}, \qquad -D = \left(\frac{\partial G}{\partial E}\right)_{T,X}, \qquad -x = \left(\frac{\partial G}{\partial X}\right)_{T,E} \tag{1.1.5}$$

The differential form of the variables become:

$$\mathrm{d}S = \left(\frac{\partial S}{\partial T}\right)_{X,E} \mathrm{d}T + \left(\frac{\partial S}{\partial E}\right)_{T,X} \mathrm{d}X + \left(\frac{\partial S}{\partial X}\right)_{T,E} \mathrm{d}X \tag{1.1.6}$$

$$\mathrm{d}D = \left(\frac{\partial D}{\partial T}\right)_{X,E} \mathrm{d}T + \left(\frac{\partial D}{\partial E}\right)_{T,X} \mathrm{d}E + \left(\frac{\partial D}{\partial X}\right)_{T,E} \mathrm{d}X \tag{1.1.7}$$

$$\mathrm{d}x = \left(\frac{\partial x}{\partial T}\right)_{X,E} \mathrm{d}T + \left(\frac{\partial x}{\partial E}\right)_{T,X} \mathrm{d}E + \left(\frac{\partial x}{\partial X}\right)_{T,E} \mathrm{d}X \tag{1.1.8}$$

Considering isothermal conditions (no temperature change), the constitutive equations for the direct and converse piezoelectric effect can be expressed in addition to the dielectric and elastic behavior as equations 1.1.9 and 1.1.10, respectively.

$$D_i = \varepsilon_0 {\varepsilon_{il}}^X E_l + d_{ijk} X_{jk} \tag{1.1.9}$$

$$x_{mn} = d_{lmn} E_l + s^E_{mnjk} X_{jk} \tag{1.1.10}$$

Here ε_0 is the vacuum permittivity, ε^X the relative dielectric permittivity under constant stress (mechanically-free condition), s^E the elastic compliance under constant electric field (electrically short-circuited condition) and d the piezoelectric charge or strain constant. The tensors in the equations are governed by following equations. Note that when $i=l$, $j=m$ and $k=n$, equations 1.1.13 and 1.1.14 are equivalent.

$$\varepsilon_0 {\varepsilon_{il}}^X = \left(\frac{\partial D_i}{\partial E_l}\right)_{T,X} = \left(\frac{\partial G^2}{\partial E_i \partial E_l}\right)_{T,X} \tag{1.1.11}$$

$$s^E_{mnjk} = \left(\frac{\partial x_{mn}}{\partial X_{jk}}\right)_{T,E} = \left(\frac{\partial G^2}{\partial X_{mn} \partial X_{jk}}\right)_{T,E} \tag{1.1.12}$$

$$d_{ijk} = \left(\frac{\partial D_i}{\partial X_{jk}}\right)_{T,E} = \left(\frac{\partial G^2}{\partial E_i \partial X_{jk}}\right)_{T} \tag{1.1.13}$$

$$d_{lmn} = \left(\frac{\partial x_{mn}}{\partial E_l}\right)_{T,X} = \left(\frac{\partial G^2}{\partial E_l \partial X_{mn}}\right)_{T} \tag{1.1.14}$$

By contrast, extensive properties which are directly proportional to the system size can also be considered. Assuming *T*, *x* and *D* are independent variables, the appropriate thermodynamic potential is the Helmholtz free energy and the variables become:

$$-S = \left(\frac{\partial A}{\partial T}\right)_{x,D}, \qquad E = \left(\frac{\partial A}{\partial D}\right)_{T,x}, \qquad X = \left(\frac{\partial A}{\partial x}\right)_{T,D} \tag{1.1.15}$$

The differential form of the variables become:

$$\mathrm{d}S = \left(\frac{\partial S}{\partial T}\right)_{x,D} \mathrm{d}T + \left(\frac{\partial S}{\partial D}\right)_{T,x} \mathrm{d}D + \left(\frac{\partial S}{\partial x}\right)_{T,D} \mathrm{d}x \tag{1.1.16}$$

$$\mathrm{d}E = \left(\frac{\partial E}{\partial T}\right)_{x,D} \mathrm{d}T + \left(\frac{\partial E}{\partial D}\right)_{T,x} \mathrm{d}D + \left(\frac{\partial E}{\partial x}\right)_{T,D} \mathrm{d}x \tag{1.1.17}$$

$$\mathrm{d}X = \left(\frac{\partial X}{\partial T}\right)_{x,D} \mathrm{d}T + \left(\frac{\partial X}{\partial D}\right)_{T,x} \mathrm{d}D + \left(\frac{\partial X}{\partial x}\right)_{T,D} \mathrm{d}x \tag{1.1.18}$$

For isothermal conditions, the piezoelectric constitutive equations can be additionally expressed as equations 1.1.19 and 1.1.20, respectively.

$$E_i = (\kappa_{il}{}^{x}/\varepsilon_0)D_l - h_{ijk}x_{jk} \tag{1.1.19}$$

$$X_{mn} = -h_{lmn}D_l + c^{D}_{mnjk}x_{jk} \tag{1.1.20}$$

Here κ^x is the inverse dielectric permittivity under constant strain (mechanically-clamped condition), c^D the elastic stiffness under constant dielectric displacement (electrically open-

circuited condition), and h the inverse piezoelectric constant. Note the negative sign in the piezoelectric coupling term. The tensors in the equations are governed by following equations. Note that when $i=l$, $j=m$ and $k=n$, equations 1.1.23 and 1.1.24 are equivalent.

$$\kappa_{il}{}^{x}/\varepsilon_0 = \left(\frac{\partial E_i}{\partial D_l}\right)_{T,x} = \left(\frac{\partial A^2}{\partial D_i \partial D_l}\right)_{T,x} \tag{1.1.21}$$

$$c^{D}_{mnjk} = \left(\frac{\partial X_{mn}}{\partial x_{jk}}\right)_{T,D} = \left(\frac{\partial A^2}{\partial x_{mn} \partial x_{jk}}\right)_{T,D} \tag{1.1.22}$$

$$h_{ijk} = -\left(\frac{\partial E_i}{\partial x_{jk}}\right)_{T,D} = -\left(\frac{\partial A^2}{\partial D_i \partial x_{jk}}\right)_{T} \tag{1.1.23}$$

$$h_{lmn} = -\left(\frac{\partial X_{mn}}{\partial D_l}\right)_{T,x} = -\left(\frac{\partial A^2}{\partial D_l \partial x_{mn}}\right)_{T} \tag{1.1.24}$$

The linear relations in isentropic condition can also be considered using the internal energy or enthalpy.

To numerically determine the efficiency of energy conversion, the electro-mechanical coupling factor k^2 is defined as stored converted energy per input energy. Thus, k is always smaller than 1. Considering an applied electric field that is converted to mechanical strain ($x_{jk} = d_{ijk}E_i$), electric field and dielectric displacement in the same direction ($D_i = \varepsilon_{ii}E_i$), and stress and strain in the same direction ($X_{jk} = s_{jkjk}x_{jk}$), the coupling factor can be represented as:

$$k_{ijk}^2 = \frac{\frac{1}{2}\frac{x_{jk}^2}{s_{jkjk}^E}}{\frac{1}{2}\varepsilon_0\varepsilon_{ii}^X E_i^2} = \frac{d_{ijk}^2}{\varepsilon_0\varepsilon_{ii}^X s_{jkjk}^E} \tag{1.1.25}$$

Considering the direct effect ($D_i = d_{ijk}X_{jk}$),, the coupling factor can also be defined as:

$$k_{ijk}^2 = \frac{\frac{1}{2}\frac{D_i^2}{\varepsilon_0\varepsilon_{ii}^X}}{\frac{1}{2}s_{jkjk}^E X_{jk}^2} = \frac{d_{ijk}^2}{\varepsilon_0\varepsilon_{ii}^X s_{jkjk}^E} \tag{1.1.26}$$

Similarly, taking into account $X_{jk} = -h_{ijk}D_i$ or $E_i = -h_{ijk}x_{jk}$ under constant x and D condition, the electro-mechanical coupling factor becomes as shown in equation 1.1.27.

$$k_{ijk}^2 = \frac{\frac{1}{2}\frac{X_{jk}^2}{c_{jkjk}^D}}{\frac{1}{2}\frac{\kappa_{ij}{}^x}{\varepsilon_0}D_i^2} = \frac{\frac{1}{2}\frac{\varepsilon_0}{\kappa_{ij}{}^x}E_i^2}{\frac{1}{2}c_{jkjk}^D x_{jk}^2} = \frac{h_{ijk}^2}{(\kappa_{ii}^x/\varepsilon_0)\cdot c_{jkjk}^D} \tag{1.1.27}$$

Unlike purely dielectric materials, there exists two mechanical resonance states in piezoelectric materials which are known as A- (resonance frequency, f_A) and B-type resonance (antiresonance frequency, f_B) as shown in Figure 1.1.1.

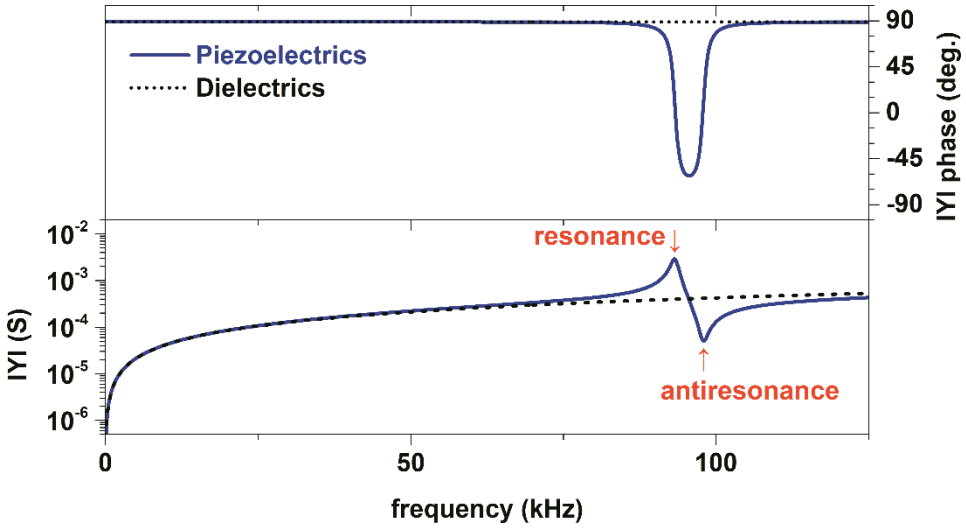

Figure 1.1.1. Illustration of typical admittance and phase spectrum for dielectric and piezoelectric materials

Figure 1.1.2 (a) and (b) shows the ideal displacement and strain distribution along the length direction (x_{11}) of a k_{311} mode bar with large electro-mechanical coupling ($k_{311} \approx 1$) at fundamental resonance and antiresonance, respectively. When loss is neglected, the resonance is achieved where the admittance becomes infinite while the antiresonance is achieved where the admittance becomes zero. Considering zero displacement at the center by the symmetry, tip displacement is maximum at the resonance frequency, creating a half wavelength along the vibration direction from induced motional capacitance, which is the capacitance change due to the generated strain. In contrast, the motional capacitance at the antiresonance frequency cancels out due to the created full wavelength along the vibration direction resulting in a tip displacement of zero. For a typical electro-mechanical coupling for PZT ceramics ($k_{311} \approx 0.3$), relatively large damped (static) capacitance partially compensates the motional capacitance and the displacement distribution becomes closer to the resonance mode, as shown in Figure 1.1.2 (c). Thus, the antiresonance frequency vibration is determined by the resonance frequency and the electro-mechanical coupling factor for the k_{311} mode resonator.

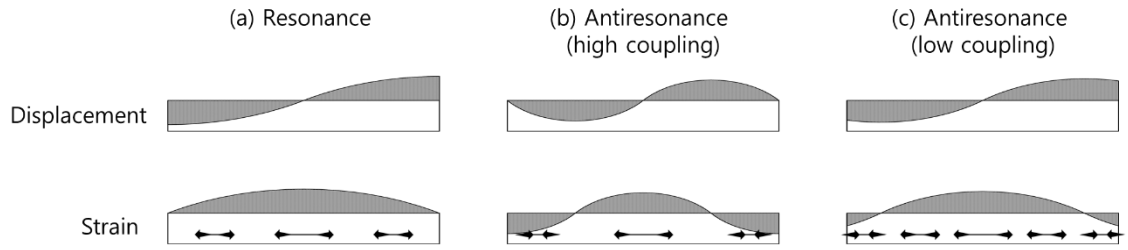

Figure 1.1.2. Illustration of displacement and strain distribution of k_{311} resonator in resonant or antiresonant state.

1.2 Non-zero properties by symmetry

Ferroelectric polycrystalline ceramics have P6mm equivalent symmetry where the rotation axis is parallel to the remanent polarization. A 60 degree transformation matrix A_{ij} for the 6-fold rotational symmetry is provided as equation 1.2.1.

$$A_{ij} = \begin{pmatrix} \cos\frac{\pi}{3} & \sin\frac{\pi}{3} & 0 \\ -\sin\frac{\pi}{3} & \cos\frac{\pi}{3} & 0 \\ 0 & 0 & 1 \end{pmatrix} \tag{1.2.1}$$

With the matrix element a_{ij}, the dielectric, elastic and piezoelectric tensor component satisfies the following condition with 60 degree rotated coordinates.

$$\varepsilon_{ij}^{X} = \sum_{k,l} a_{ik} a_{jl} \varepsilon_{kl}^{X} \tag{1.2.2}$$

$$d_{ijk} = \sum_{l,m,n} a_{il} a_{jm} a_{kn} d_{lmn} \tag{1.2.3}$$

$$s_{ijkl}^{E} = \sum_{m,n,o,p} a_{im} a_{jn} a_{ko} a_{lp} s_{mnop}^{E} \tag{1.2.4}$$

Since physical properties along crystallographically equivalent directions should be the same, the independent tensor parameters can be reduced by the symmetry. In addition to the reduction, the tensor suffixes for stress and strain can be simplified in matrices as shown in Table 1.2.1 for convenience. For instance, X_1=X_{11} and X_5=2X_{13}. Note the matrix notation for shear properties (i.e. X_5) connotes two equivalent tensors (X_{13}=X_{31}) [14].

Table 1.2.1. Matrix notation for stress and strain tensors.

Tensor notation	11	22	33	23, 32	13, 31	12, 21
Matrix notation	1	2	3	4	5	6

The independent tensor properties of the piezoelectric polycrystalline is shown in the following three matrices.

$$\varepsilon^{X} = \begin{bmatrix} \varepsilon_{11}^{X} & 0 & 0 \\ 0 & \varepsilon_{11}^{X} & 0 \\ 0 & 0 & \varepsilon_{33}^{X} \end{bmatrix} \tag{1.2.5}$$

$$d = \begin{bmatrix} 0 & 0 & 0 & 0 & d_{15} & 0 \\ 0 & 0 & 0 & d_{15} & 0 & 0 \\ d_{31} & d_{31} & d_{33} & 0 & 0 & 0 \end{bmatrix} \tag{1.2.6}$$

$$s^E = \begin{bmatrix} s_{11}^E & s_{12}^E & s_{13}^E & 0 & 0 & 0 \\ s_{12}^E & s_{11}^E & s_{13}^E & 0 & 0 & 0 \\ s_{13}^E & s_{13}^E & s_{33}^E & 0 & 0 & 0 \\ 0 & 0 & 0 & s_{55}^E & 0 & 0 \\ 0 & 0 & 0 & 0 & s_{55}^E & 0 \\ 0 & 0 & 0 & 0 & 0 & 2(s_{11}^E - s_{12}^E) \end{bmatrix} \quad (1.2.7)$$

Piezoelectric vibrators have different vibration modes upon the geometry and dimension. Typical geometries for the reduced piezoelectric *d* constant in equation 1.2.6 are illustrated in Table 1.2.2 with the primary properties and boundary conditions.

Table 1.2.2. The primary properties for various vibration modes.

	(a) k_{31} mode	(b) k_{33} mode	(c) k_{15} mode
	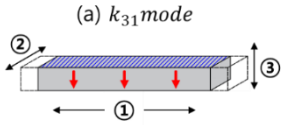	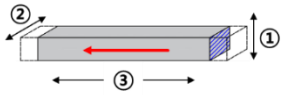	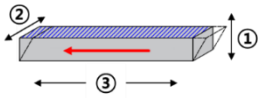
Dielectric permittivity	ε_{33}^X	$\varepsilon_{33}^{x\_3}$	ε_{11}^X
Elastic compliance	s_{11}^E	s_{33}^D	s_{55}^D
EM coupling factor	$k_{31}^2 = \frac{d_{31}^2}{\varepsilon_0 \varepsilon_{33}^X s_{11}^E}$	$k_{33}^2 = \frac{d_{33}^2}{\varepsilon_0 \varepsilon_{33}^X s_{33}^E}$	$k_{15}^2 = \frac{d_{15}^2}{\varepsilon_0 \varepsilon_{11}^X s_{55}^E}$
Frequency parameter Ω	$\Omega_{B,31} = \frac{\pi}{2}\frac{f_{B,31}}{f_{A,31}}$	$\Omega_{A,33} = \frac{\pi}{2}\frac{f_{A,33}}{f_{B,33}}$	$\Omega_{A,15} = \frac{\pi}{2}\frac{f_{A,15}}{f_{B,15}}$
Effective coupling	$\frac{k_{31}^2}{1-k_{31}^2} = -\Omega_{B,31}\cot\Omega_{B,31}$	$k_{33}^2 = \Omega_{A,33}\cot\Omega_{A,33}$	$k_{15}^2 = \Omega_{A,15}\cot\Omega_{A,15}$

The relations for different boundary conditions are shown in Figure 1.2.1 [15]. For the converse piezoelectric effect, the applied electric energy is equivalent to the sum of the electrical energy from purely dielectric behavior under mechanically clamped conditions (constant *x*) and the converted mechanical energy, as expressed in equation 1.2.8.

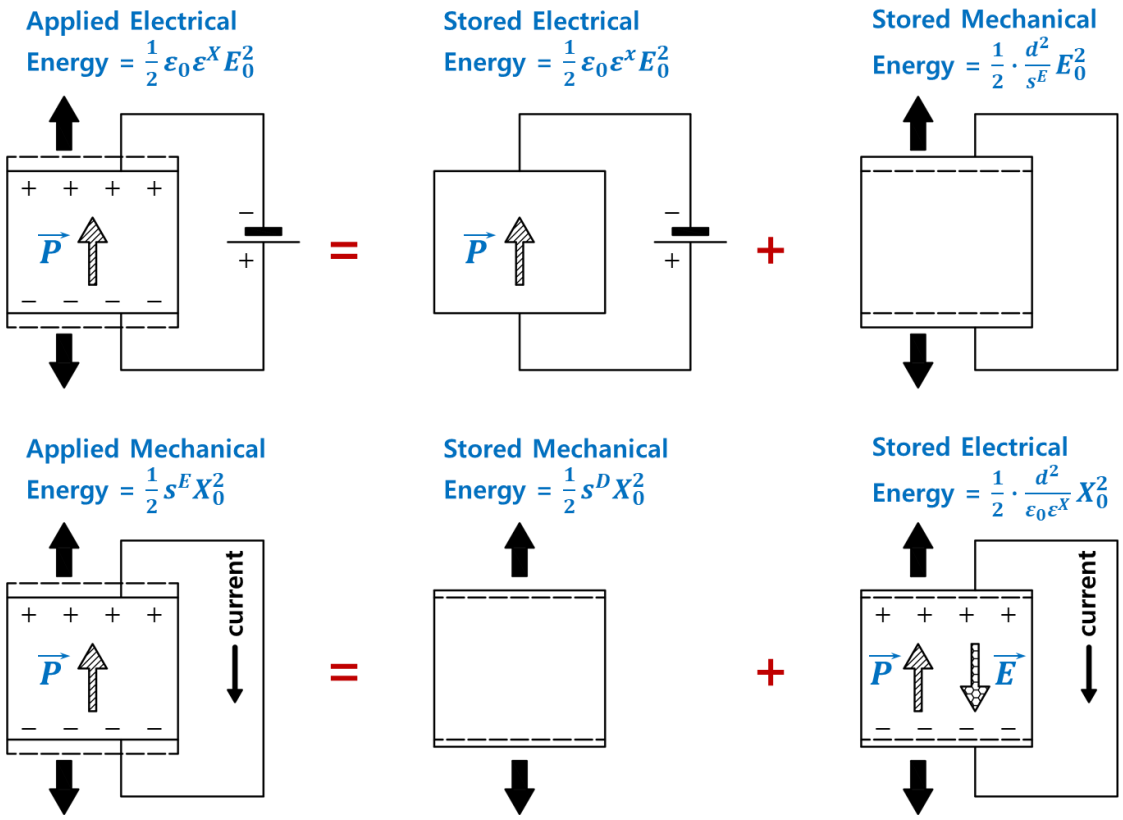

Figure 1.2.1. Conceptual figures for explaining the relation of properties in different boundary conditions.

$$\varepsilon_0\varepsilon^X = \varepsilon_0\varepsilon^x + \frac{d^2}{s^E} \tag{1.2.8}$$

Consequently, for the direct piezoelectric effect, the applied mechanical energy is equivalent to the sum of mechanical energy from purely elastic behavior where dielectric displacement is constant (electrically open-circuited) and the converted electrical energy, as expressed in equation 1.2.9.

$$s^E = s^D + \frac{d^2}{\varepsilon_0\varepsilon^X} \tag{1.2.9}$$

Hence, following relations with the electro-mechanical coupling factor can be obtained.

$$\frac{\varepsilon^x}{\varepsilon^X} = 1 - k^2 \tag{1.2.10}$$

$$\frac{s^D}{s^E} = 1 - k^2 \tag{1.2.11}$$

From the directly-obtainable physical properties, the definition of electro-mechanical coupling factor for the k_{33} or k_{15} mode in Figure 1.2.1 can be rewritten as equation 1.2.12.

$$\frac{k^2}{(1-k^2)^2} = \frac{d^2}{\varepsilon_0 \varepsilon_{33}^x s_{33}^D} \tag{1.2.12}$$

1.3 Mechanical quality factor and the loss factors

The mechanical quality factor (Q_m) is a dimensionless parameter indicating how the resonator damps, which is defined as equation 1.3.1. When the quality factor is large, the damping is small.

$$Q_\mathrm{m} = 2\pi \cdot \frac{\text{Energy stored/cycle}}{\text{Energy lost/cycle}} = \frac{\text{resonance frequency}}{\text{half power bandwidth}} \tag{1.3.1}$$

It is known that energy loss is dissipated as a form of heat and is inversely proportional to the Q_m [16]. The losses in piezoelectric ceramics in the ferroelectric region (below the Curie temperature) are mainly believed to occur from domain wall motion [17]–[22]. The energy loss is

hypothesized to have three components due to the dielectric, elastic and piezoelectric behaviors [23]–[27]. In general, the electrical and mechanical losses are described using equations 1.3.2 and 1.3.3, respectively.

$$\varepsilon^{X*} = \varepsilon^{X}(1 - j\tan\delta') \tag{1.3.2}$$

$$s^{E*} = s^{E}(1 - j\tan\phi') \tag{1.3.3}$$

Here j is the imaginary notation, tanδ' the intensive dielectric loss and tanϕ' the intensive elastic loss. Note the extrinsic parameters such as X or E are constant. The piezoelectric loss is generally neglected, assuming no phase lag of the piezoelectric constant [28], as indicated in the IEEE standard of piezoelectricity. It seems reasonable for Rochelle salt [29]. However, a large piezoelectric phase lag was discovered in PZT-based ceramics [30]–[32] and efforts to represent the piezoelectric loss in equivalent circuits have been made [33], [34]. The piezoelectric loss tanθ' can be treated as equation 1.3.4.

$$d^{*} = d(1 - j\tan\theta') \tag{1.3.4}$$

The phase delay of each behavior is indicated in each hysteresis loop sketched in Figure 1.3.1. The area of the dielectric and elastic hysteresis loops corresponds to energy density units (J/m^3). However, a scale factor should be multiplied to the area of the piezoelectric hysteresis to reach energy density units. Thus, the piezoelectric loss should be coupled with other loss factors. The scale unit for x-E and D-X loop is d/s and $d/\varepsilon_0\varepsilon$, respectively. Then, the coupled loss for d^2/s and $d^2/\varepsilon_0\varepsilon$ becomes 2tanθ'- tanϕ' and 2tanθ'- tanδ', respectively.

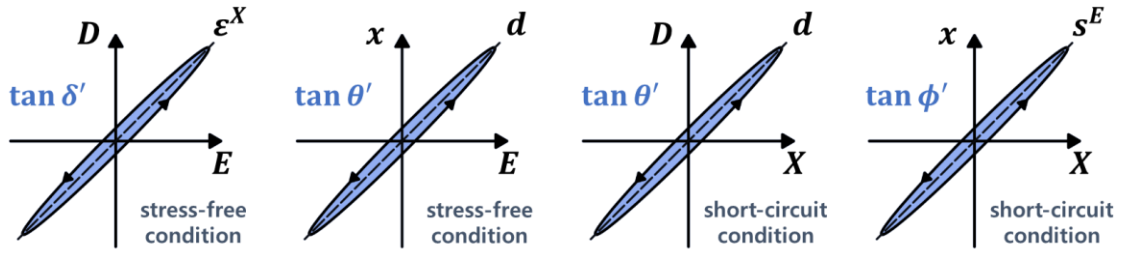

Figure 1.3.1. Conceptual representations of intensive loss parameters in hysteresis curves.

Considering the completely clamped condition for a state inside a material, the extensive loss parameters are introduced as:

$$\kappa^{x*} = \kappa^{x}(1 + j\tan\delta) \tag{1.3.5}$$

$$c^{D*} = c^{D}(1 + j\tan\phi) \tag{1.3.6}$$

$$h^{*} = h(1 + j\tan\theta) \tag{1.3.7}$$

Here tanδ is the extensive dielectric loss, tanϕ the extensive elastic loss and tanθ the extensive piezoelectric loss. The negative phase lags (+ sign) are set to indicate D or x is induced by the applied E or X. The schematic hysteresis loops of extensive loss parameters are shown in Figure 1.3.2. Here, the scale factors for E-x and X-D loops should be $h\varepsilon_0/\kappa$ and h/c and the coupled loss becomes 2tanθ- tanδ and 2tanθ- tanϕ, respectively.

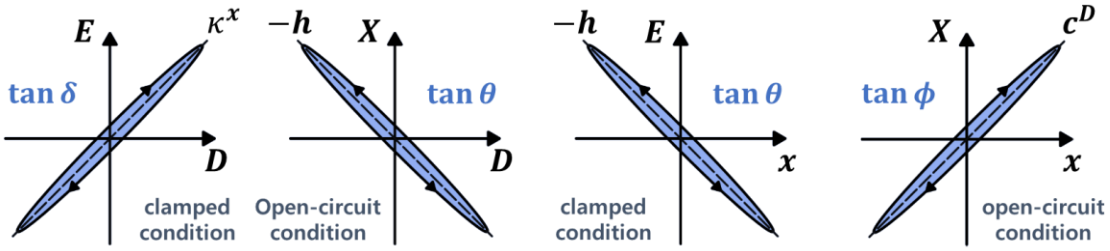

Figure 1.3.2. Conceptual representations of extensive loss parameters in hysteresis curves.

In lead-based piezoelectric resonators, the quality factor in B-type resonance (Q_B) is much higher than the one in A-type resonance (Q_A) due to the large intensive piezoelectric loss [31], [32]. This means that it could be more efficient to drive piezoelectric transducers at antiresonance frequency rather than at the resonance frequency [35], [36]. Integrating all loss factors in the admittance equation, Yuan Zhuang et al. proposed a loss determination methodology to derive all loss factors in various structures from the off-resonance dielectric properties, A- and B-type resonance frequencies and the corresponding quality factors [37]–[39]. A typical structure for a mechanically free condition is the k_{31} vibration mode. The relations of $Q_{A,31}$ and $Q_{B,31}$ are shown in equation 1.3.9 with the intensive loss parameters.

$$\frac{1}{Q_{A,31}} = \frac{1}{\tan \phi'_{31}} \tag{1.3.8}$$

$$\frac{1}{Q_{B,31}} = \frac{1}{Q_{A,31}} - \frac{2}{1 + \left(\frac{1}{k_{31}} - k_{31}\right)^2 \Omega^2_{B,31}} \cdot (2 \tan \theta'_{31} - \tan \phi'_{31} - \tan \delta'_{31}) \tag{1.3.9}$$

A typical structure for a mechanically clamped condition is the k_{15} vibration mode with wave propagation along the thickness direction (thickness shear). The relations of $Q_{A,15}$ and $Q_{B,15}$ are shown in equation 1.3.11 along with the extensive loss parameters.

$$\frac{1}{Q_{A,15}} = \frac{1}{\tan\phi_{55}} \tag{1.3.10}$$

$$\frac{1}{Q_{A,15}} = \frac{1}{Q_{B,15}} + \frac{2}{k_{15}^2 - 1 + \frac{\Omega_{A,15}^2}{k_{15}^2}} \cdot (\tan\phi_{55} + \tan\delta_{11} - 2\tan\theta_{15}) \tag{1.3.11}$$

Considering a one-dimensional model, the intensive and extensive loss parameters satisfy the following relationship where *K* is an involutory matrix.

$$\begin{bmatrix} \tan\delta' \\ \tan\phi' \\ \tan\theta' \end{bmatrix} = K \begin{bmatrix} \tan\delta \\ \tan\phi \\ \tan\theta \end{bmatrix} \tag{1.3.12}$$

$$K = \frac{1}{1-k^2} \begin{bmatrix} 1 & k^2 & -2k^2 \\ k^2 & 1 & -2k^2 \\ 1 & 1 & -1-k^2 \end{bmatrix} \tag{1.3.13}$$

1.4 Piezoelectricity with canted polarization

In 1982, Jun Kuwata et al. reported large piezoelectricity of $0.91Pb(Zn_{1/3}Nb_{2/3})O_3 - 0.09PbTiO_3$ single crystals when it is in rhombohedral symmetry poled along a pseudo-cubic [001] axis [40]. The enhancement was explained with conversion coordinates in section 1.2. Xiao-Hong Du et al. reported a similar enhancement of piezoelectricity with canted-polarization in rhombohedral PZT single crystals [41] and polycrystalline ceramics with strong shear properties [42]. This phenomena can be observed not only in PZT-based materials, but also in various compositions [43]–[47].

Although the electro-mechanical coupling can be enhanced with canted polarization, recent studies on rhombohedral piezoelectric single crystals indicates larger loss with electric field angled from the remanent polarization direction. Shujun Zhang et al. reported higher electrical and mechanical losses in a <001> oriented rhombohedral single crystal compared to a <111> oriented one. [48]. However, the piezoelectric loss has not been discussed yet in terms of polarization orientation due to its uncertainty of physical origin.

Chapter 2

Dissertation objectives and structures

2.1 Objectives

Due to the existence of large piezoelectric loss, driving the piezoelectric resonator at antiresonance frequency is recommended for high power applications. Unfortunately, the physical origin of the piezoelectric loss is yet unclear. Assuming the origin of losses arise from domain dynamics, it is essential to understand the piezoelectric loss behavior as a function of polarization orientation.

Tetragonal, rhombohedral and morphotropic phase boundary (MPB) PZT exhibit different anisotropy of properties, thus it is anticipated that the polarization orientation dependence could vary. In this study, the polarization orientation dependence of piezoelectric loss of 1% Nb-doped PZT (PNZT) near MPB was studied with respect to their anisotropic properties.

One of the most important requisites for the study is reliable analysis. There has been strong interest in the piezoelectric society to determine the complex piezoelectric parameters accurately, and various methods were proposed [49]–[54].

2.2 Structures

This first chapter describes the fundamental background related to the dissertation, including an introduction to piezoelectricity, property anisotropy and loss factors. Research on polarization-canted structures is also introduced. Based on the background, this chapter provides objectives of this study with its constituent elements.

Chapter 3 shows the preliminary research on the polarization orientation dependence of the piezoelectric properties. The PNZT polycrystalline ceramics with canted polarization were prepared in collaboration with PI Ceramics, Germany. The IEEE standard of piezoelectricity and conventional 3dB method were used to analyze real and imaginary parameters for effective k_{31} and k_{33} mode vibration. A linear fitting was made for the changes of loss factors in terms of the polarization-canted angle. A large change of piezoelectric loss was observed with angled polarization compared to other losses, especially in tetragonal PNZT.

The preliminary research induces several arguments on the analysis reliability. Chapter 4 discusses the arguments, including the measurement error in k_{33} mode structures due to the indirect calculation, definition of mechanical quality factor and spurious modes near the shear mode. In addition to the discussion, solutions are proposed to overcome the issues.

Using the solution provided, a new methodology to obtain anisotropic properties in polycrystalline ceramic is provided in chapter 5. Three polarization-canted k_{31} structures are needed in the method. With off-resonance, near k_{31} mode and near k_{15} mode analysis, all necessary parameters for k_{31}, k_{33} and k_{15} vibration modes could be derived.

Chapter 6 presents the anisotropic properties obtained with the proposed analysis method. Vibration mode separation was additionally studied to support the method. Based on the anisotropic properties, the polarization orientation dependence of properties is reconsidered.

In chapter 7, extensive loss parameters are calculated to represent the completely clamped condition inside of a material. The contribution of extensive loss factors on the intensive elastic loss is provided for discussion. A negative loss phenomenon is discovered in tetragonal PNZT and a clockwise hysteresis model is provided for an explanation.

The final chapter summarizes the contents of the dissertation. In addition, a possible future work is suggested.

Chapter 3

Polarization dependence of properties in k_{31} and k_{33} vibration mode

3.1 Preparation of the polarization canted structure

In collaboration with PI Ceramics GmbH (Germany), 1% Nb-doped PZT ceramics (PNZT) were prepared. A soft material composition with low Q_m was chosen to enhance the loss change with polarization angle. The $PbZrO_3$ (PZ) to $PbTiO_3$ (PT) ratio was controlled to be (50/50), (53/47) or (56/44) to obtain tetragonal, MPB and rhombohedral structures; these were verified with x-ray diffraction patterns recorded on an Empyrean XRD with Cu-Kα radiation (λ = 1.5406 A) over a 2θ range of 20 to 60 degrees as shown in Figure 3.1.1.

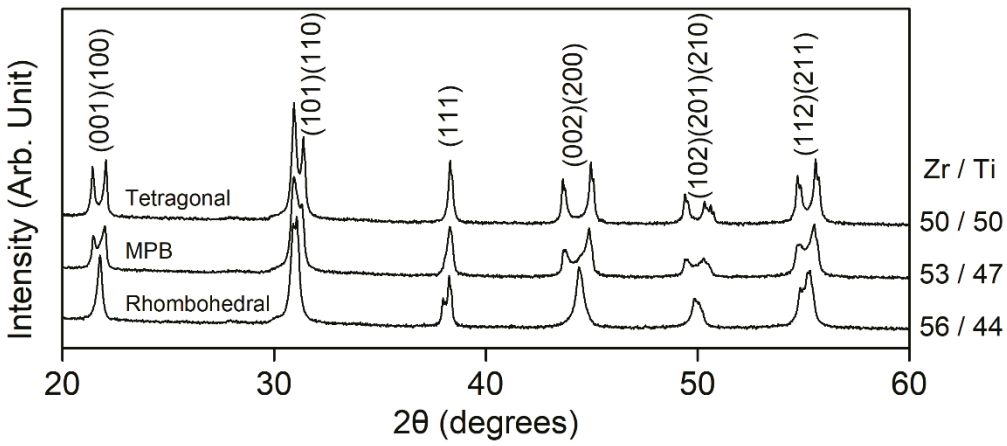

Figure 3.1.1. X-ray diffraction patterns of the prepared 1% Nb doped PZT ceramics.

A flow chart for conventional ceramic processing and the post processing to produce polarization-canted structures is shown in Figure 3.1.2. Piezoelectric blocks were prepared in a dimension of 44x20x23mm and poled under 4kV/mm DC field in an oil bath. The blocks were then

diced into 1×3×15mm bars with water-cooled diamond tools to have polarization-canted angles of 0, 15, 30, 45, 60, 75 and 90 degrees. Finally, 50nm Cr and 600nm CuNi45 electrodes were sputtered at 100mbar and 100°C to demonstrate effective k_{33} and k_{31} vibration modes. Consequently, ten of each geometry illustrated in Figure 3.1.3 were produced.

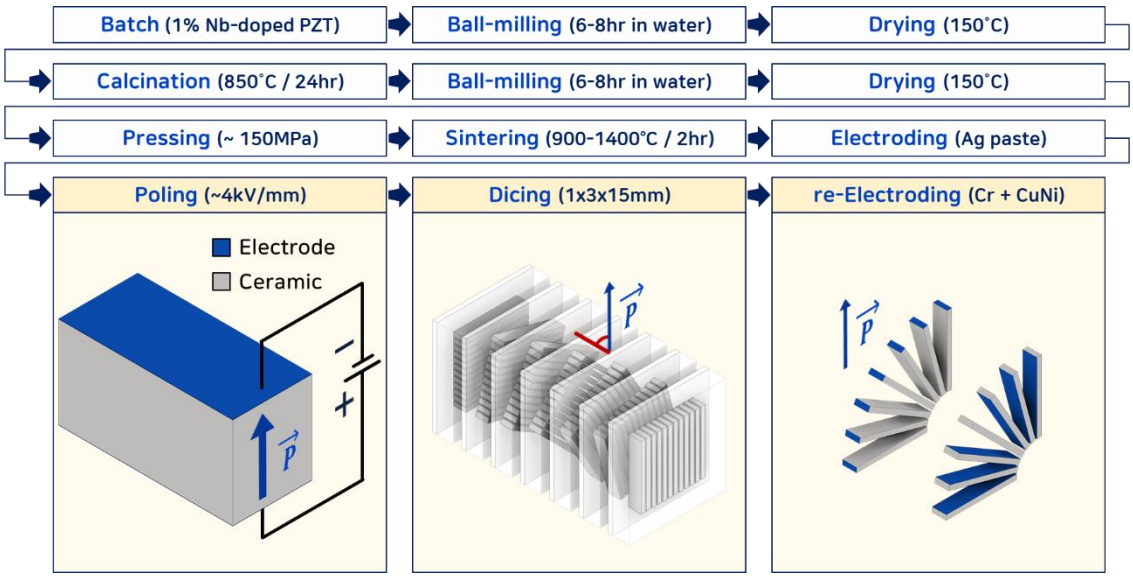

Figure 3.1.2. Schematic diagram of polarization-canted sample preparation process conducted with PI Ceramics GmbH, Germany.

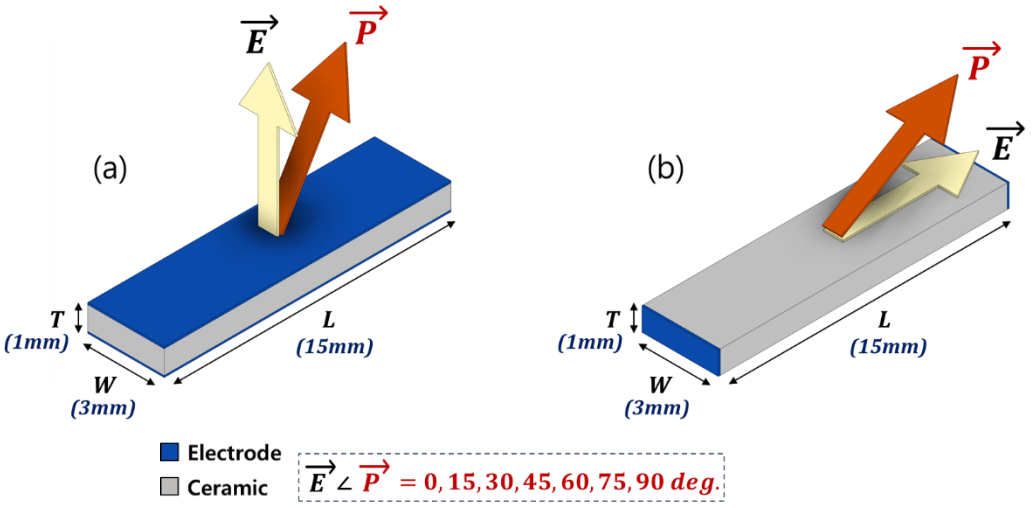

Figure 3.1.3. Illustration of produced (a) effective k_{31} and (b) k_{33} mode structures.

Due to a concern about potential damage during post-dicing processing, ATILA/GiD (Micromechatronics Inc., PA, USA) finite element simulations were conducted to help quantify any impact from damaged surfaces. 20 micron thick damaged layers with no piezoelectricity were applied to the general k_{31} structure with standard PZT5A properties as shown in Figure 3.1.4. The dielectric and elastic loss factors are exaggerated to be 120% of the undamaged properties to simulate the worst conditions.

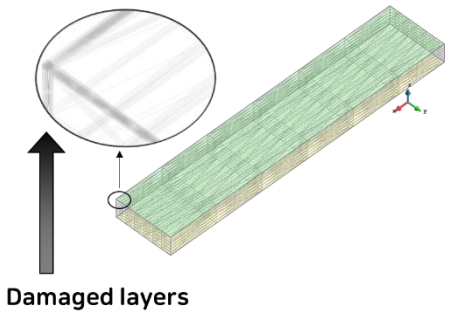

Figure 3.1.4. FEA model with damaged surfaces.

The results with damaged surfaces are compared to the undamaged ones in Table 3.1.1. Considering errors from sample process and the exaggerated condition, the damage is negligible.

Table 3.1.1. FEA simulation results of k_{31} mode PZT5A with and without damaged surfaces.

	Q_A	Q_B	s_{11}^E	k_{31}
Damaged surface	76.2	83.3	1.64E-11	55.3%
Undamaged sample	77.0	83.2	1.65E-11	56.3%

The densities of the ceramics (ρ) were measured by a water-immersion technique (ASTM STD C373-72). All samples were boiled in distilled water and cooled down before the measurement. Table 3.1.2 shows the obtained density from equation 3.1.1.

Table 3.1.2. Measured density of 1% Nb-doped PZT near MPB.

Structure	Tetragonal	MPB	Rhombohedral
Density (kg/m^3)	7700	7670	7640
Relative density (%)	96.1	95.6	95.0

$$\rho = \frac{W_d}{W_f - W_w} \cdot \rho_w \tag{3.1.1}$$

Here, ρ_w is the density of the deionized-water, W_w the wet weight measured in the water, W_f the filled weight measured out of the water before drying (where pores are filled with water), and W_d the weight dried measured out of the water after being completely dried.

The impedance spectrum and its phase are analyzed from 50kHz to 1.5MHz with impedance analyzer HP4294A (Agilent Technologies, CA, USA) to assure vibration mode separation. The effective transvers (k_{31}) or longitudinal (k_{33}) vibration modes were observed around 100kHz while the effective shear (k_{15}) vibration mode was observed near 1MHz range, as shown in Figure 3.1.5. Since the effective vibration modes are well separated due to the designed

dimensions, it is possible to analyze the effective properties of each mode, in terms of the angle between polarization and applied electric field.

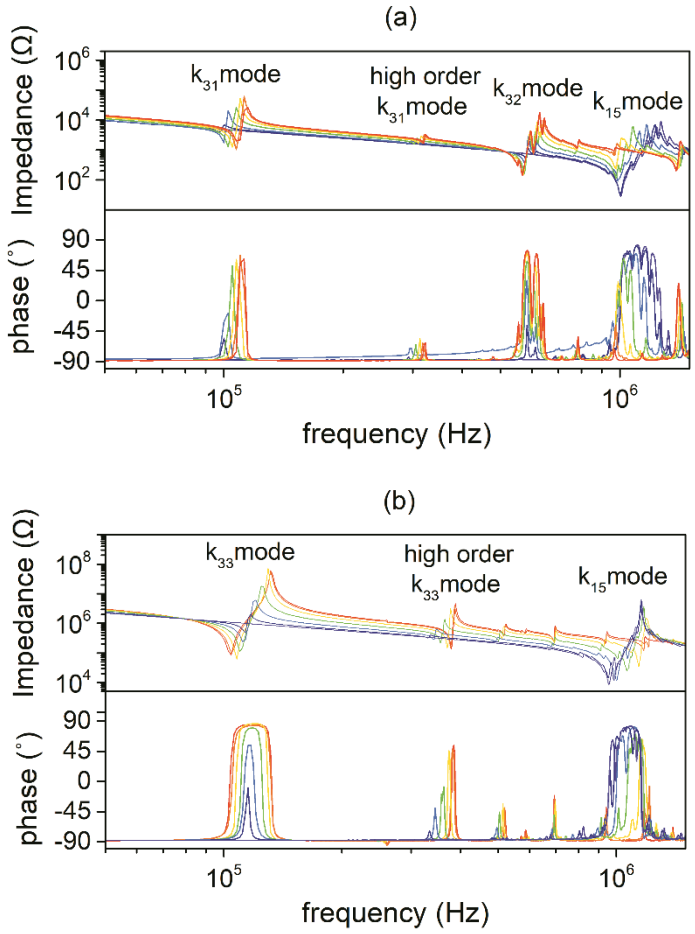

Figure 3.1.5. Vibration mode separation of (a) transverse and (b) longitudinal modes (~100 kHz) from shear mode (~1 MHz).

3.2 Experimental procedure and results

By excluding the k_{15} mode with spurious peaks, the k_{31} and k_{33} mode properties were analyzed. The capacitance under constant stress and intensive dielectric loss of effective k_{31}-k_{15}

samples were measured under 100 Hz with an LCR meter SR715 (Stanford Research Systems Inc., CA, USA), because the dielectric properties near resonance are similar to the off-resonance properties[55]. The obtained dielectric permittivity and loss are shown in Figure 3.2.1. The box chart indicates minimum, maximum, quartiles and median values for ten of each sample per geometry.

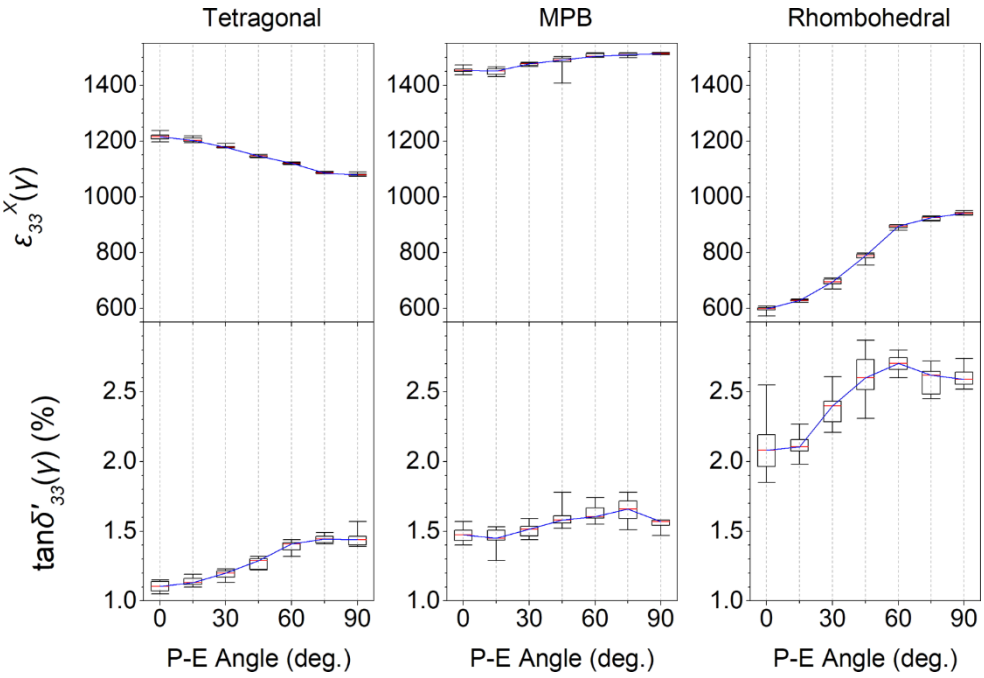

Figure 3.2.1. (a) Effective dielectric permittivity and (b) corresponding loss under constant stress condition.

The MPB structure shows the highest compliance property (highest permittivity) as expected [56]. Compared to the permittivity perpendicular to the polarization, the permittivity along the polarization is larger in tetragonal PNZT and smaller in rhombohedral PNZT, similar to previously reported PZT ceramics [57]–[59]. The phenomenology is generally understood in terms of domain clamping mechanism from remaining domains. When the structure exhibits low domains clamping in the unpoled state, the permittivity along the poling direction decreases,

resulting in the lower permittivity along the polarization than the perpendicular one [60]. When the structure exhibits significant amount of 180° domains clamping in unpoled state, most of the 180° domains along the polarization direction are removed upon poling, while a large amount remains perpendicular to the polarization. Consequently, the permittivity along the net polarization direction could be higher than the perpendicular one [61], [62]. It is interesting to note that the dielectric loss is always higher with larger polarization-canted angle, regardless of the real parameters.

The impedance spectra near 100kHz were obtained with an impedance analyzer HP4294A (Agilent Technologies, CA, USA). The resonance and antiresonance frequencies were determined from the minimum and maximum peak of impedance magnitude. The corresponding quality factors were obtained from the 3dB up/down method [38]. The frequencies and quality factors for effective k_{31} and k_{33} mode vibration are shown in Figure 3.2.2 (a) and (b), respectively. Note that some of the parameters cannot be obtained for higher angle ranges, because the resonance and antiresonance peaks are too small.

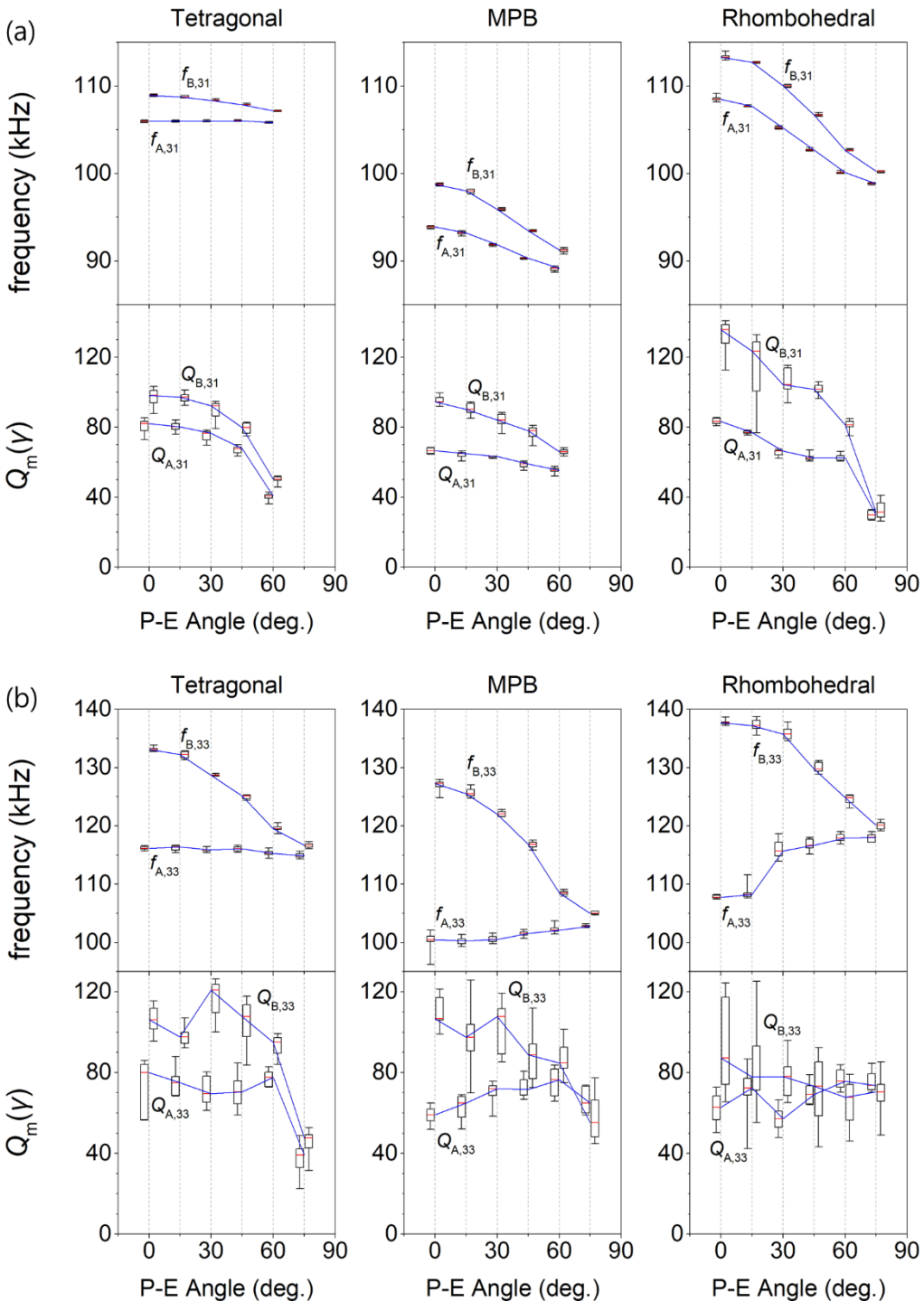

Figure 3.2.2. Resonance frequencies and quality factors for (a) Effective k_{31} and (b) k_{33} mode.

With diminished electro-mechanical coupling from canted polarization, the resonance and antiresonance frequencies become closer to each other. The declining tendency of the resonance frequency f_A in the k_{31} mode and antiresonance frequency f_B in the k_{33} mode is due to a higher elastic compliance with canted polarization. The Q_B is larger than Q_A regardless of the polarization angle in the k_{31} vibration mode. The Q_A and Q_B gets closer to each other with the canted polarization due to the diminution of the effective coupling factor, leaving only the intensive elastic loss to result in the quality factors. It can be predicted that $Q_A = Q_B$ when the coupling factor is zero using equation 1.3.8 or 1.3.9. A large measurement error is suspected for the k_{33} mode due to the small capacitance. The error will be discussed in section 4.1.

The effective elastic compliance of the effective k_{31} and k_{33} modes were obtained with equations in Table 1.2.2 with respect to their boundary condition. The effective elastic compliances were calculated as follows:

$$s^E_{11,\mathrm{eff}}(\gamma) = \frac{v^2_{11,\mathrm{eff}}(\gamma)}{\rho} = \frac{1}{4f^2_{\mathrm{A},31,\mathrm{eff}}(\gamma)L^2\rho} \tag{3.2.1}$$

$$s^D_{33,\mathrm{eff}}(\gamma) = \frac{v^2_{33,\mathrm{eff}}(\gamma)}{\rho} = \frac{1}{4f^2_{\mathrm{b},33,\mathrm{eff}}(\gamma)T^2\rho} \tag{3.2.2}$$

$$s^E_{33,\mathrm{eff}}(\gamma) = \frac{s^D_{33,\mathrm{eff}}(\gamma)}{1 - k^2_{33,\mathrm{eff}}(\gamma)} \tag{3.2.3}$$

Here $v_{11,\mathrm{eff}}(\gamma)$ and $v_{33,\mathrm{eff}}(\gamma)$ is the effective sound velocity along the vibration direction of each mode. The corresponding intensive elastic losses are obtained as:

$$\tan \phi'_{11,\text{eff}}(\gamma) = \frac{1}{Q_{A,31,\text{eff}}(\gamma)} \tag{3.2.4}$$

$$\tan \phi'_{33,\text{eff}}(\gamma) = \frac{1}{Q_{B,33,\text{eff}}(\gamma)} + \left(\frac{1}{Q_{A,33,\text{eff}}(\gamma)} - \frac{1}{Q_{B,33,\text{eff}}(\gamma)}\right) \cdot \frac{k^4_{33,\text{eff}}(\gamma) - k^2_{33,\text{eff}}(\gamma) + \Omega^2_{A,33,\text{eff}}(\gamma)}{2\left(1 - k^2_{33,\text{eff}}(\gamma)\right)} \tag{3.2.5}$$

The obtained elastic properties are shown in Figure 3.2.3.

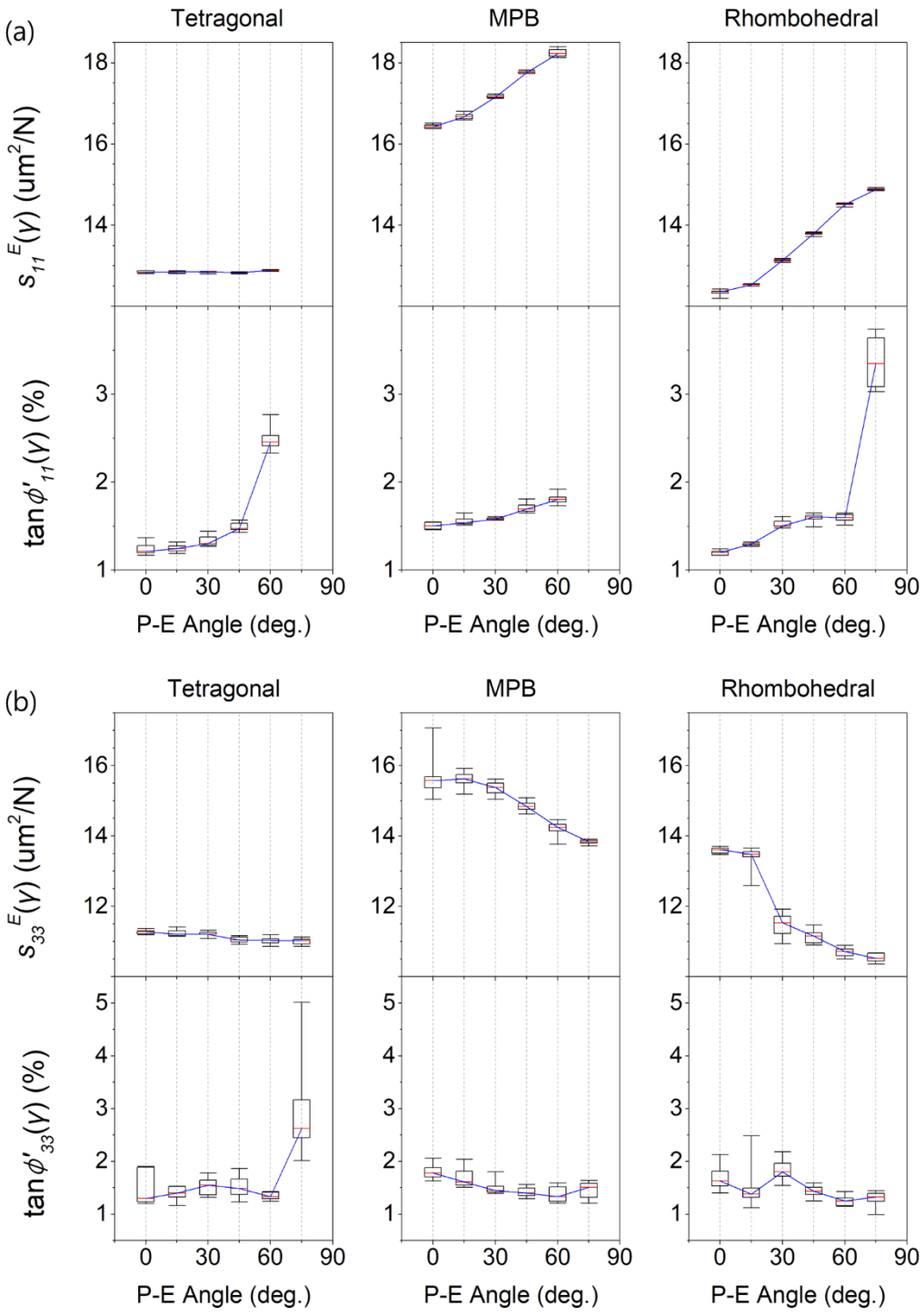

Figure 3.2.3. Elastic compliance and corresponding loss under constant electric field condition for (a) Effective k_{31} and (b) k_{33} mode.

Here, the MPB shows the most compliant properties while tetragonal structures are the stiffest. The effective elastic compliance for the k_{31} mode changes from s_{11}^{E} to s_{33}^{E} with increase in the canting angle. The elastic loss is in a similar range excluding the samples with largely canted polarization.

The electro-mechanical coupling factor for both effective k_{31} and k_{33} modes were calculated at the resonance and antiresonance frequencies. Figure 3.2.4 (a) and (b) shows the degradation of the effective coupling factor with angled polarization in effective k_{31} and k_{33} vibration modes, respectively. Here, the coupling enhancement by canted polarization for rhombohedral PNZT was observed only in the effective k_{31} mode but not in the effective k_{33} mode.

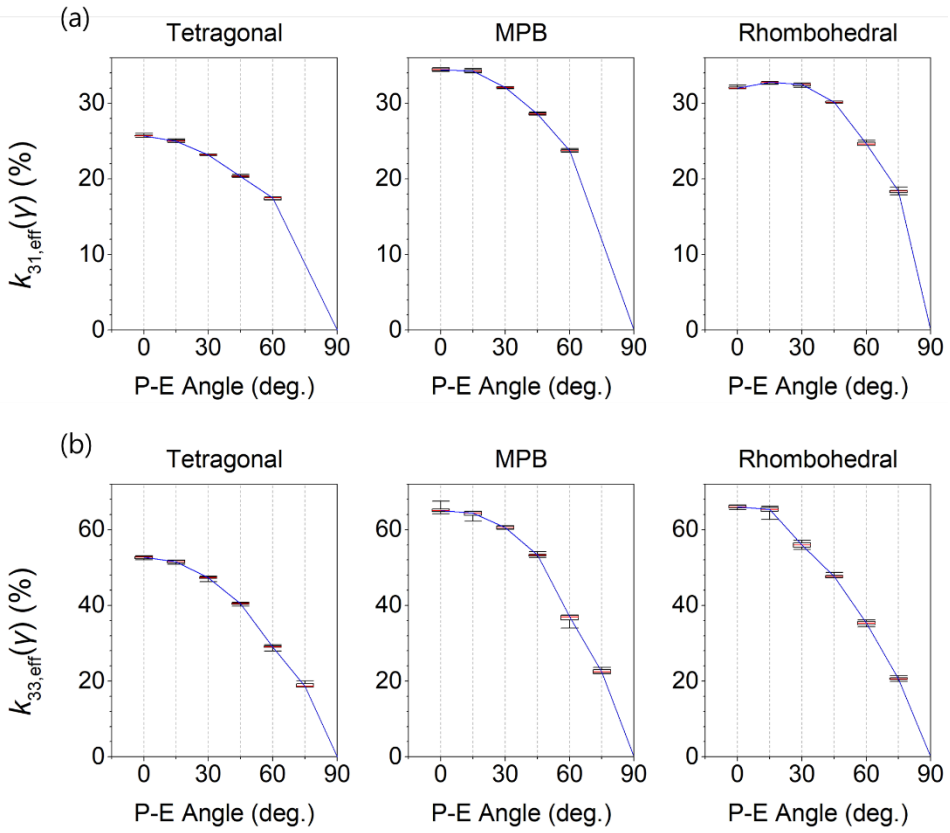

Figure 3.2.4. Effective electro-mechanical coupling factors with angled polarization in tetragonal, MPB and rhombohedral PNZT for the (a) k_{31} and (b) k_{33} vibration modes.

The piezoelectric *d* constant and corresponding losses are calculated as:

$$d_{31,\mathrm{eff}}(\gamma) = -\sqrt{k_{31,\mathrm{eff}}^2(\gamma) s_{11,\mathrm{eff}}^E(\gamma) \varepsilon_0 \varepsilon_{33,\mathrm{eff}}^X(\gamma)} \tag{3.2.6}$$

$$\tan\theta'_{31,\mathrm{eff}}(\gamma) = \left(\frac{1}{Q_{A,31,\mathrm{eff}}(\gamma)} - \frac{1}{Q_{B,31,\mathrm{eff}}(\gamma)}\right) \cdot \frac{1 + \left(\frac{1 - k_{31,\mathrm{eff}}^2(\gamma)}{k_{31,\mathrm{eff}}(\gamma)}\right)^2 \cdot \Omega_{B,31,\mathrm{eff}}^2(\gamma)}{4} + \frac{\tan\phi'_{11,\mathrm{eff}}(\gamma) + \tan\delta'_{33,\mathrm{eff}}(\gamma)}{2} \tag{3.2.7}$$

$$d_{33,\mathrm{eff}}(\gamma) = \sqrt{k_{33,\mathrm{eff}}^2(\gamma) s_{33,\mathrm{eff}}^E(\gamma) \varepsilon_0 \varepsilon_{33,\mathrm{eff}}^X(\gamma)} \tag{3.2.8}$$

$$\tan\theta'_{33,\mathrm{eff}}(\gamma) = \frac{\tan\phi'_{33,\mathrm{eff}}(\gamma)}{2k_{33,\mathrm{eff}}^2(\gamma)} + \frac{\tan\delta'_{33,\mathrm{eff}}(\gamma)}{2} - \frac{1 - k_{33,\mathrm{eff}}^2(\gamma)}{2k_{33,\mathrm{eff}}^2(\gamma) \cdot Q_{B,33,\mathrm{eff}}(\gamma)} \tag{3.2.9}$$

The obtained piezoelectric parameters are shown in Figure 3.2.5. An enhancement of piezoelectric *d* constant in rhombohedral PNZT could be found in both k_{31} and k_{33} modes, unlike the electro-mechanical coupling factor. The major reason for the different phenomena is due to the increase of dielectric permittivity and elastic compliance with angled polarization. With largely canted polarization, the effective *d* constant degrades and become zero when the polarization is perpendicular to the applied electric field. In the k_{31} vibration mode, the piezoelectric loss dramatically increases on changing the angle (more than 50% when 45 degree canted). In the k_{33} vibration mode, larger piezoelectric loss with canted polarization could only be observed in tetragonal PNZT.

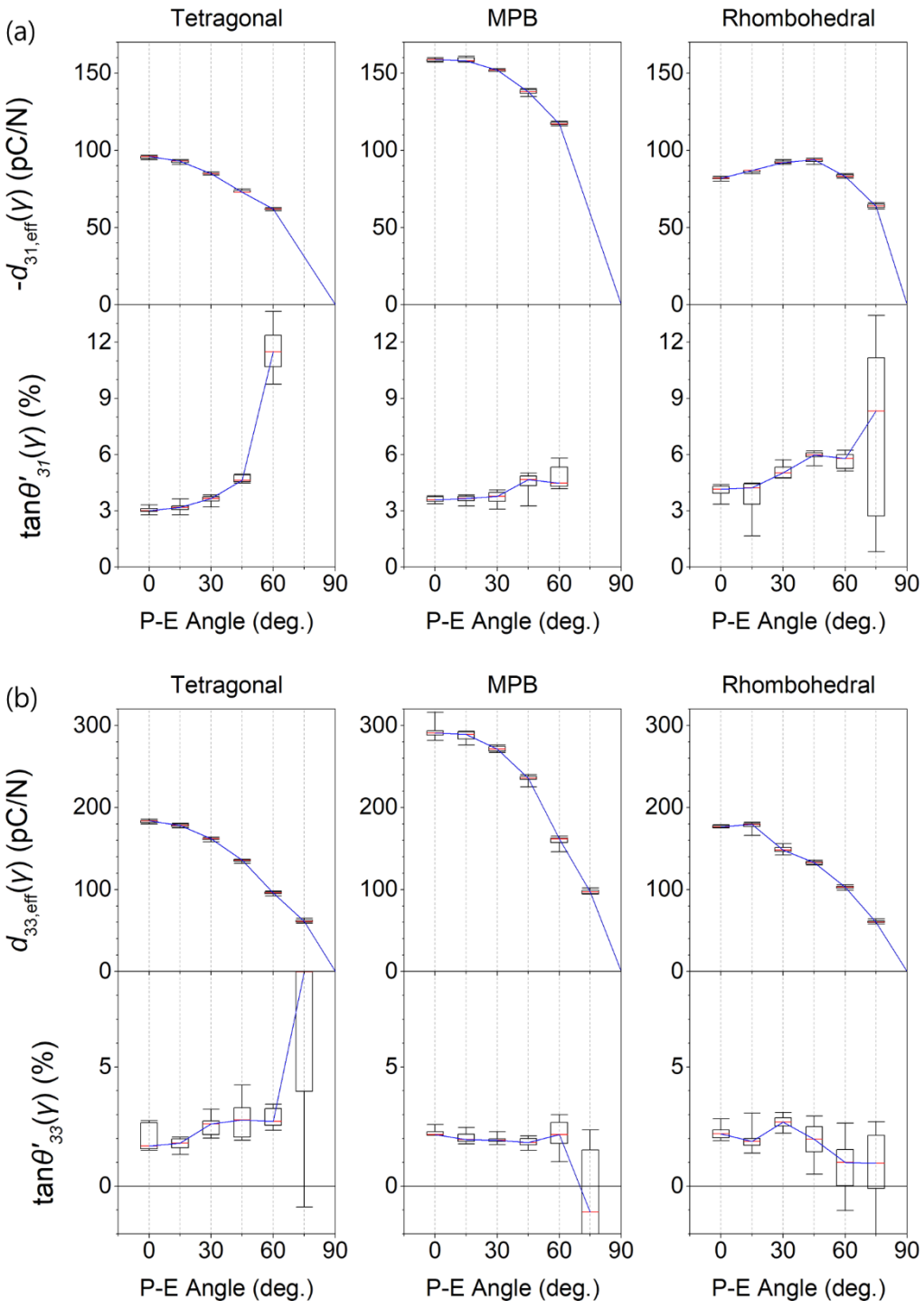

Figure 3.2.5. Effective piezoelectric parameters under (a) k_{31} and (b) k_{33} vibration mode.

Finally, all three loss factors are plotted together in Figure 3.2.6 with a linear fitting curve. The change of intensive piezoelectric loss is dominant compared to other loss factors by canting the polarization, meaning that the piezoelectric loss depends more on the polarization angle than the dielectric or elastic losses. Comparing the ceramics, the piezoelectric loss change is largest for the tetragonal PNZT [63].

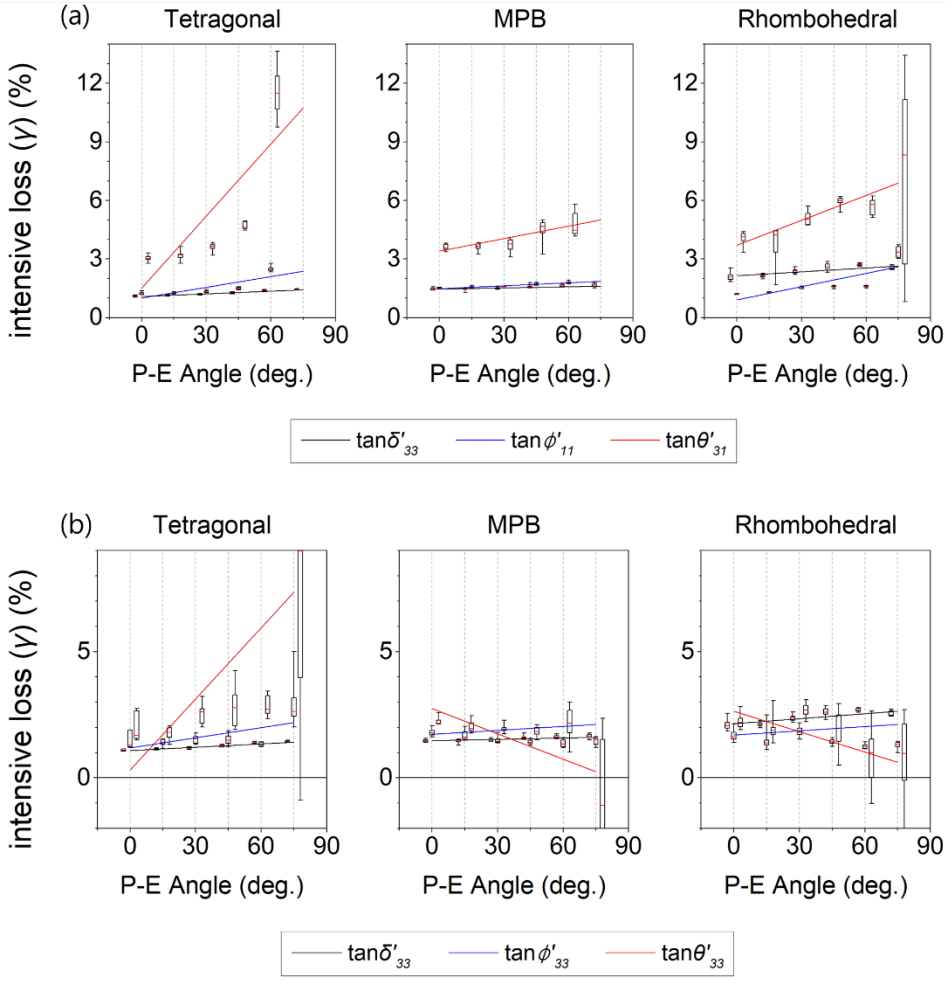

Figure 3.2.6. Intensive loss factors by polarization orientation under (a) k_{31} and (b) k_{33} vibration mode.

Chapter 4

Review on the conventional characterization method

In Chapter 3, a significant change of piezoelectric loss with polarization orientation was observed. However, the result induces several questions. Since accurate analysis is essential to discuss material behavior [64], this chapter introduces the issues with proposed solutions.

4.1 Ambiguity in elastic compliance and losses

In general, the elastic properties are obtained from the sound velocity calculated from the resonance frequency of k_{31} mode structure and the antiresonance frequency of k_{33} mode structure where the half-wave is generated along the vibration direction. However, by structural constraint, a significant difficulty is experienced occasionally in determining the intensive elastic compliance and the corresponding loss in the k_{33} mode [65]–[67]. The error can be easily found in the polarization-canted structure. As illustrated in Figure 4.1.1, the elastic compliance along the 11-direction with canted polarization of $90 - \gamma$ degrees should be the same as the compliance along the 33-direction with canted polarization of γ degrees. Note the s_{33}^{E} should be indirectly calculated from s_{33}^{D} and the electro-mechanical coupling factor as shown in equation 3.2.3.

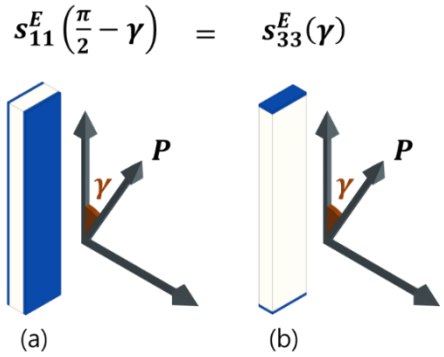

Figure 4.1.1. Illustration of the elastic compliance of effective (a) k_{31} and (b) k_{33} vibration mode.

Figure 4.1.2 shows the s_{33}^E obtained from the effective (a) k_{31} and (b) k_{33} modes for rhombohedral PNZT.

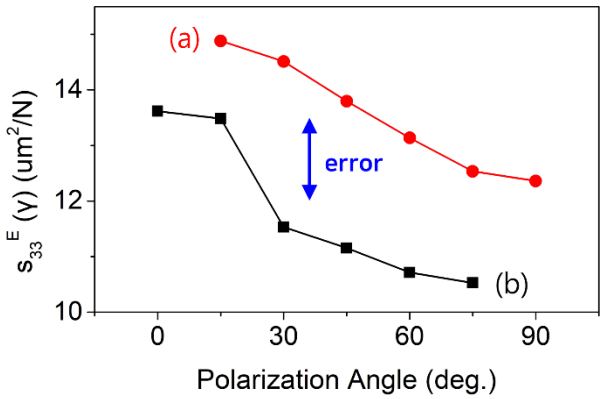

Figure 4.1.2. The s_{33}^E of rhombohedral PNZT obtained from effective (a) k_{31} and (b) k_{33} vibration modes.

Large measurement error necessarily comes from the sample structure due to a very small current and capacitance compared to effective k_{31} mode samples. The high structural impedance from the low capacitance induces large measurement error in the overall electrical response. The errors are amplified due to indirect calculation of the properties from the assumed boundary conditions which are mechanically-free condition along the 3 axis (stress X_3 constant) or an

electrically-open circuit (electric displacement D_3 constant) condition. The relative error in the elastic compliance and loss for a standard k_{33} mode rod is shown in equation 4.1.1 and 4.1.2, respectively [67].

$$\frac{\Delta s_{33}^{E}}{s_{33}^{E}} = \frac{\Delta s_{33}^{D}}{s_{33}^{D}} + 2\left(\frac{\Delta k_{33}}{k_{33}}\right)\left(\frac{k_{33}^2}{1-k_{33}^2}\right) \tag{4.1.1}$$

$$\frac{\Delta \tan\phi'_{33}}{\tan\phi'_{33}} \approx -\frac{\Delta \tan\delta'_{33}}{\tan\delta'_{33}} - 2\left(\frac{\Delta k_{33}}{k_{33}}\right)\left(\frac{1}{1-k_{33}^2}\right) \tag{4.1.2}$$

Any error in the electro-mechanical coupling factor dramatically increases the error of s_{33}^{E} and $\tan\phi'_{33}$. Note that the relative errors from the electro-mechanical coupling factor in real and imaginary parameters have opposite signs. Although the relative error must be accepted inevitably at present using the conventional rod geometry, higher accuracy in the real and imaginary parameters is needed.

A solution to obtain k_{33} mode properties can be provided using standard k_{31} mode structures in addition to γ and π/2- γ degree polarization-canted structures where $0<\gamma<\pi/4$ as illustrated in Figure 4.1.3 [67].

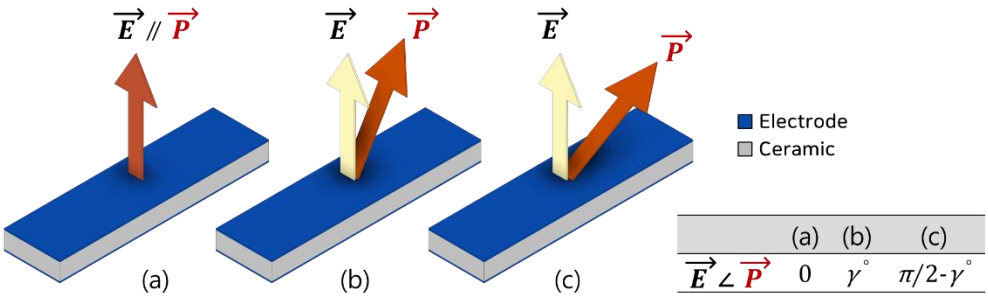

Figure 4.1.3. Illustration of essential structures of proposed method to obtain k_{33} mode elastic properties.

The canted polarization can be expressed in rotated coordinates with the transformation matrix in equation 4.1.3. Thus, the effective elastic compliance with canted polarization in k_{31} mode shown in Figure 4.1.3 (b) is given by equation 4.1.4.

$$A = \begin{pmatrix} \cos\gamma & 0 & \sin\gamma \\ 0 & 1 & 0 \\ -\sin\gamma & 0 & \cos\gamma \end{pmatrix} \tag{4.1.3}$$

$$s^{\mathrm{E}}_{11,\mathrm{eff}}(\gamma) = \cos^4(\gamma)s^{\mathrm{E}}_{11} + \cos^2(\gamma)\sin^2(\gamma)\left(2s^{\mathrm{E}}_{13} + s^{\mathrm{E}}_{55}\right) + \sin^4(\gamma)s^{\mathrm{E}}_{33} \tag{4.1.4}$$

From the difference of Figure 4.1.3 (b) and (c), the elastic compliance s_{13}^{E} and s_{55}^{E} can be canceled out, leaving only s_{11}^{E} and s_{33}^{E}. s_{11}^{E}, $s_{11,\mathrm{eff}}^{\mathrm{E}}(\pi/2\text{-}\gamma)$ and $s_{11,\mathrm{eff}}^{\mathrm{E}}(\gamma)$ can be obtained from measured resonance frequencies of the effective k_{31} modes and the elastic compliance s_{33}^{E} becomes:

$$s^{\mathrm{E}}_{33} = s^{\mathrm{E}}_{11} + \frac{s^{\mathrm{E}}_{11,\mathrm{eff}}\left(\frac{\pi}{2} - \gamma\right) - s^{\mathrm{E}}_{11,\mathrm{eff}}(\gamma)}{\cos 2\gamma} \tag{4.1.5}$$

Taking into account the phase lag in equation 4.1.6, the effective elastic loss with canted polarization in the k_{31} mode can be expressed as shown in equation 4.1.7:

$$s^{\mathrm{E},*}_{\mathrm{eff}}(\theta) = s^{\mathrm{E}}_{\mathrm{eff}}(\theta)\left(1 - j\tan\phi'_{\mathrm{eff}}(\theta)\right) \tag{4.1.6}$$

$$\tan\phi'_{11,\mathrm{eff}}(\theta) = \frac{\begin{bmatrix}\cos^4\theta s^{\mathrm{E}}_{11}\tan\phi'_{11} + \sin^4\theta s^{\mathrm{E}}_{33}\tan\phi'_{33} \\ +\cos^2\theta\sin^2\theta\left(2s^{\mathrm{E}}_{13}\tan\phi'_{13} + s^{\mathrm{E}}_{55}\tan\phi'_{55}\right)\end{bmatrix}}{s^{\mathrm{E}}_{11,\mathrm{eff}}(\theta)} \tag{4.1.7}$$

Accordingly, from Figure 4.1.3 (b) and (c) samples, $\tan\phi'_{13}$ and $\tan\phi'_{55}$ can be canceled out and the intensive elastic loss in k_{33} mode ($\tan\phi'_{33}$) can be derived from measured effective parameters as in equation 4.1.8:

$$\tan\phi'_{33} = \frac{s^{E}_{11}\tan\phi'_{11} + \frac{\left[\begin{bmatrix} s^{E}_{11,\mathrm{eff}}\left(\frac{\pi}{2}-\gamma\right)\tan\phi'_{11,\mathrm{eff}}\left(\frac{\pi}{2}-\gamma\right) \\ -s^{E}_{11,\mathrm{eff}}(\gamma)\tan\phi'_{11,\mathrm{eff}}(\gamma) \end{bmatrix}\right]}{\cos 2\gamma}}{s^{E}_{33}} \tag{4.1.8}$$

Therefore, the real and imaginary intensive elastic parameters of k_{33} vibration mode are obtainable from measurements of effective k_{31} samples. The feasibility of the proposed method was checked for the rhombohedral PNZT samples prepared as described in chapter 3. The sample capacitance of k_{31} mode structure, 0.24 nF, is L^2/t^2 times higher than 1.0 pF of the k_{33} mode sample; thus structural impedance can be neglected.

Frequency vs. voltage/current response was observed with a high-power characterization system (HiPoCS™) at a constant vibration velocity of 5 mm/sec where the heat generation is low enough to prevent peak distortion near the resonance and antiresonance frequencies [68], [69]. A schematic diagram of the HiPoCS™ is shown in Figure 4.1.4.

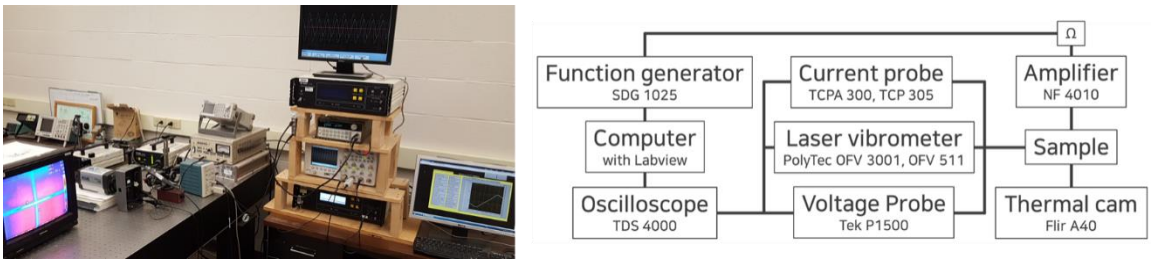

Figure 4.1.4. HiPoCS™ developed in International Center for Actuators and Transducers.

The effective elastic compliance and loss were derived from the measured resonance frequency and corresponding 3dB bandwidth on the voltage spectrum and compared with the results in chapter 3. The predicted effective elastic compliances by angled polarization along with the 95% confidence intervals are plotted in Figure 4.1.5 (a) (b) and (c) with the measured parameters in Figure 4.1.5 (b). Note the effective elastic compliance for k_{31} vibration mode changes from s_{11}^E to s_{33}^E. The s_{33}^E calculated with IEEE standard is plotted in Figure 4.1.5 (d) for comparison. The s_{33}^E derived from the proposed method and IEEE standard is 14.82 μm^2/N ±0.13% and 13.59 μm^2/N ±0.43%, respectively. The relative error found in the real parameter was -8.3%; the IEEE Standard underestimates the elastic compliance.

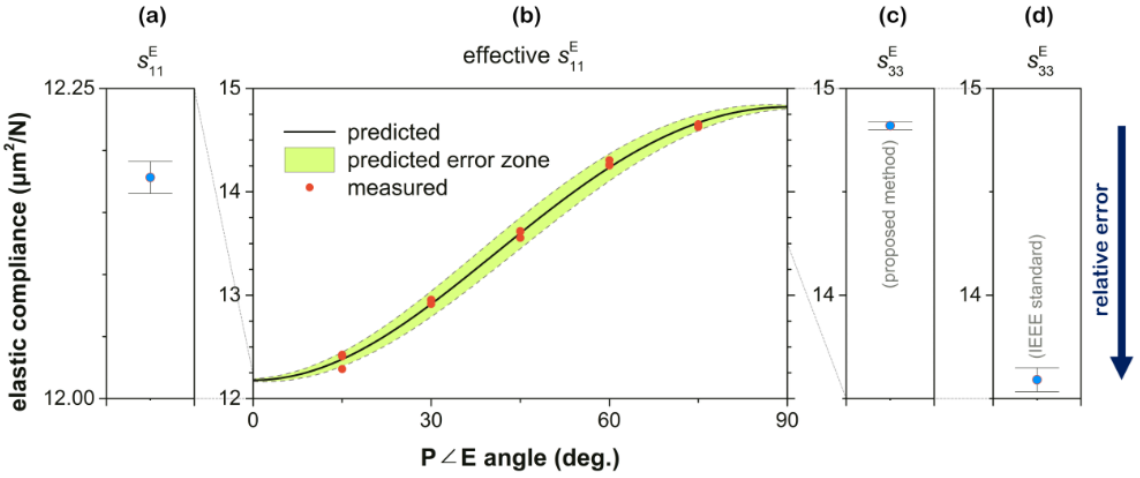

Figure 4.1.5. Elastic compliance (a) s_{11}^E, (b) effective s_{11}^E by polarization angle, (c) s_{33}^E derived from the proposed method and (d) s_{33}^E calculated with IEEE standard.

Figure 4.1.6 (a), (b) and (c) shows the predicted effective elastic loss with angled polarization in 95% confidence intervals. In comparison with, the loss calculated from the k_{33} geometry is plotted in Figure 4.1.6 (d). The tanϕ'$_{33}$ derived from the proposed method is 0.0096 ±0.0003 (2.6%) where the loss with the conventional method is 0.017 ± 0.002 (9.1%). The relative

error found in the imaginary parameter was 74%; the conventional method overestimates the elastic loss.

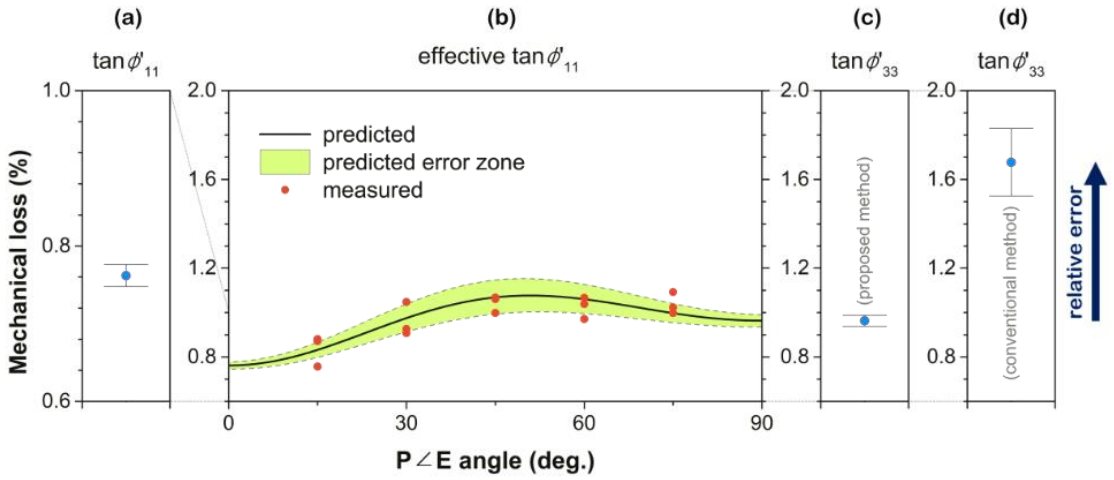

Figure 4.1.6. Elastic loss (a) tanϕ'$_{11}$, (b) effective tanϕ'$_{11}$ by polarization angle, (c) tanϕ'$_{33}$ derived from the proposed method and (d) tanϕ'$_{33}$ calculated with conventional method.

The relative error in the real and imaginary parts of the intensive elastic parameter have opposite signs, as predicted in the calculation of relative error. The measured effective elastic parameters mostly fit in the 95% confidence zone. Considering the material property deviation in each sample from ceramic processing, the deviation of derived method is acceptable and the accuracy of the obtained elastic parameters is high.

4.2 Errors of mechanical quality factors

Although there exists controversy in determination of quality factors [51]–[54], [70], 3dB down and up bandwidth from the maximum and minimum peak of admittance spectra is

conventionally utilized to calculate the half-power bandwidth for Q_A and Q_B, respectively. The problem is, the definition of half-power bandwidth contains an error when the electro-mechanical coupling is small where the damped capacitance cannot be neglected with respect to the small motional capacitance. In the case, the 3dB bandwidth doesn't provide half of the motional admittance or impedance, but overestimates the bandwidth as shown in Figure 4.2.1.

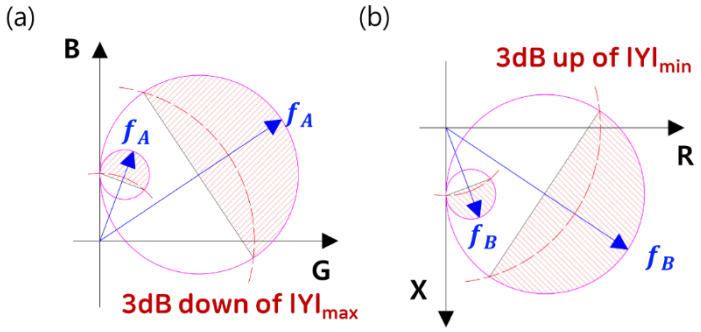

Figure 4.2.1. 3dB bandwidth in low and high coupling condition shown in (a) lYl and (b) lZl circle for Q_A and Q_B, respectively.

The problem can be encountered in some recent research focused on piezoelectric polymers, composites, thin films or lead-free materials with low electro-mechanical coupling factors [71]. Since the polarization-canted samples also have low electro-mechanical coupling with largely canted angle where the effective polarization is small, the error should not be neglected to accurately analyze the effect of polarization orientation on piezoelectric properties.

As a solution, using the quadrantal bandwidth from the admittance or impedance circle is proposed. This gives the frequency bandwidth in between the maximum and minimum susceptance B or reactance X as shown in Figure 4.2.2.

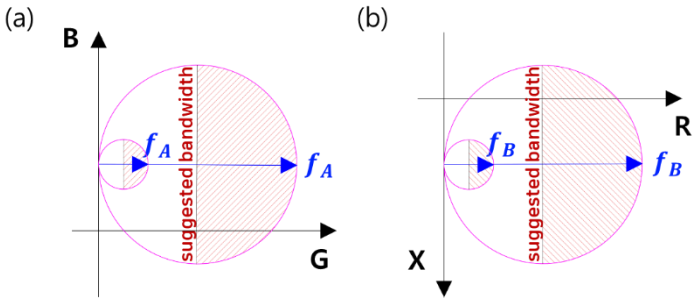

Figure 4.2.2. Suggested quadrantal bandwidth in (a) lYl and (b) lZl circle for Q_A and Q_B, respectively.

ATILA/GiD finite element simulation of PZT5A in k_{31} mode was conducted with controlled inputs of piezoelectric d_{31} constant and fixed loss parameters to demonstrate the errors in conventional compared to the suggested bandwidth in low coupling conditions. The elastic and piezoelectric loss calculated from the conventional 3dB method and proposed quadrantal method are shown in Figure 4.2.3 with respect to the piezoelectric d_{31} constant.

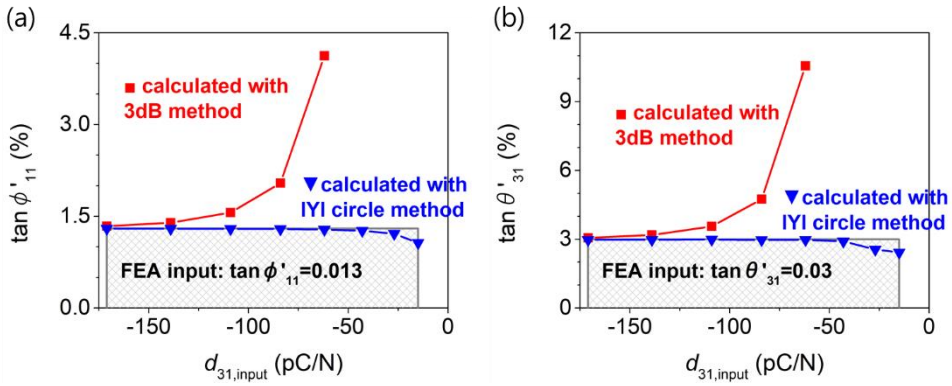

Figure 4.2.3. (a) Elastic and (b) piezoelectric loss calculated from conventional 3dB method and the proposed quadrantal method.

Owing to the overestimated half power bandwidth in the conventional 3dB method, the mechanical quality factor is underestimated; thus the elastic loss is overestimated. Similarly, the piezoelectric loss is also overestimated with the conventional method. Some difficulties of loss reproduction in FEA simulations are reported in several studies [72], [73].

The analysis result shows that the proposed quadrantal method is much more accurate and the FEA can reproduce the losses accurately even when the electro-mechanical coupling is small.

4.3 Spurious modes near the shear vibration

The most challenging issue in k_{15} mode analysis is the spurious peaks appearing near the shear vibration mode. With the spurious peaks, the resonance/antiresonance frequencies and corresponding half-power bandwidth cannot be accurately obtained. However, with various polarization-canted structures, the issue can be resolved. With the change of effective elastic properties and coupling factor for samples with canted polarization, the resonance or antiresonance frequency can be moved far from the spurious peaks. To verify this idea, ATILA/GiD simulation was made for PZT5A with the parameters in Table 4.3.1.

Table 4.3.1. PZT5A properties used to simulate spurious modes near the shear vibration mode in ATILA/GiD software.

ρ	s_{11}^E	s_{12}^E	s_{13}^E	s_{33}^E	s_{55}^E	$\tan\phi$ ’
7750 kg/m^3	16.4 μm^2/N	-5.74 μm^2/N	-7.22 μm^2/N	18.8 μm^2/N	47.5 μm^2/N	0.010
d_{15}	d_{31}	d_{33}	$\tan\theta$ ’	ε_{11}^X	ε_{33}^X	$\tan\delta$ ’
584 pC/N	-171 pC/N	374 pC/N	0.015	1730	1700	0.020

The loss factors are set as isotropic parameters for the convenience of calculation. The piezoelectric loss was set as the average of dielectric and elastic loss as indicated in the IEEE

standard of piezoelectricity. Thus, regardless of the polarization orientation, the quality factors should be given by equation 4.3.1.

$$Q_{\mathrm{A},15} = Q_{\mathrm{B},15} = \frac{1}{\tan\phi'} = 100 \tag{4.3.1}$$

The dimensions were set to 15, 3 and 1mm for the length, width and thickness, the same as the measured samples. For various polarization orientations, the admittance/impedance was simulated from 600 to 1100 kHz. The result shows that spurious peaks could be separated from the motional admittance / impedance by changing the polarization angle, as shown in Figure 4.3.1 (a) and (b).

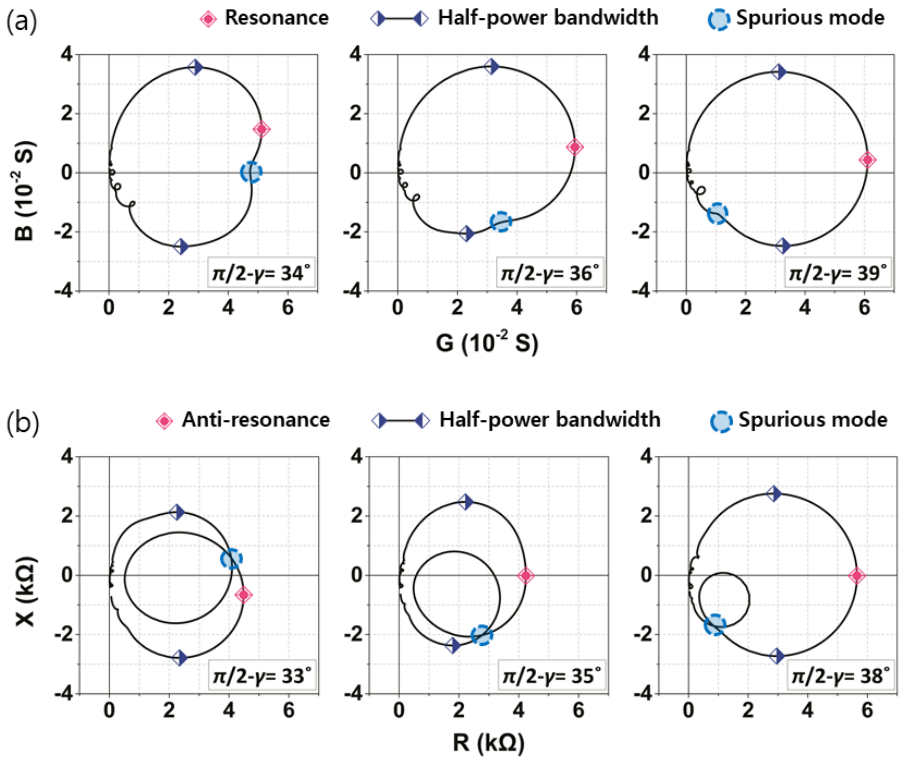

Figure 4.3.1. Spurious peaks separating from the (a) motional admittance and (b) impedance by changing the polarization orientation.

To verify the assumption that there is no distortion of the shear vibration when the spurious mode is moved away from the motional admittance / impedance forming clean half-circle, $Q_{A,15}$ and $Q_{B,15}$ were calculated for the various orientations in Figure 4.3.1. The results are shown in Table 4.3.2.

Table 4.3.2. Calculated Q_A and Q_B with various polarization orientations in Figure 4.3.1.

$\pi/2-\gamma$	34°	36°	39°
$Q_{A,15}$	55.4	62.6	102

$\pi/2-\gamma$	33°	35°	38°
$Q_{B,15}$	19.8	18.1	99.6

With the spurious mode separated from the half-power bandwidth of the shear vibration (39 degrees for the resonance peak and 38 degrees for the antiresonance peak), the quality factors could be accurately calculated with less than 2 percent error. Finding the most undistorted half-circles are essential for further analysis.

Chapter 5

Proposed characterization method

5.1 Introduction

Resolving the characterization issues with the solutions provided in Chapter 4, an advanced characterization method is proposed to obtain the anisotropic intensive parameters for the k_{31}, k_{33} and k_{15} vibration modes. Effective k_{31}-k_{15} structures with canted polarization as illustrated in Figure 5.1.1 are suggested for the characterization. More than three different geometries of canting angle ($\gamma_1 \neq \gamma_2 \neq \gamma_3$) are necessary. The proposed methodology contains 1) off-resonance dielectric measurements, 2) effective k_{31} mode analysis, 3) off-resonance d_{33} measurements and 4) effective k_{15} mode analysis.

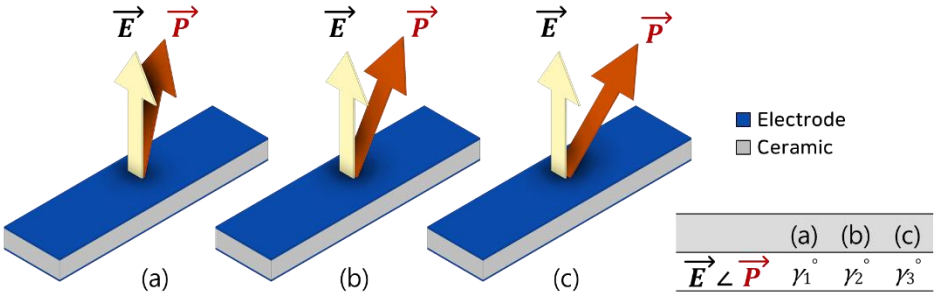

Figure 5.1.1. Illustration of effective k_{31}-k_{15} structure with canted polarization.

The effective dielectric, elastic and piezoelectric properties for the structure can be expressed with the independent parameters in equations 5.1.2 to 5.1.4 using the rotational transition matrix A. From analysis of the effective parameters, independent material properties can be obtained.

$$\mathrm{A} = \left(a_{ij}\right) = \begin{pmatrix} \cos\gamma & 0 & \sin\gamma \\ 0 & 1 & 0 \\ -\sin\gamma & 0 & \cos\gamma \end{pmatrix} \tag{5.1.1}$$

$$\varepsilon^{*,X}_{ij,eff}(\gamma) = \sum_{k,l} a_{ik}a_{jl}\varepsilon^{X}_{kl}\left(1 - j\tan\delta'_{kl}\right) \tag{5.1.2}$$

$$s^{*,E}_{ijkl,eff}(\gamma) = \sum_{m,n,o,p} a_{im}a_{jl}a_{ko}a_{lp}s^{E}_{mnop}\left(1 - j\tan\phi'_{mnop}\right) \tag{5.1.3}$$

$$d^{*}_{ijk,eff}(\gamma) = \sum_{l,m,n} a_{il}a_{jm}a_{kn}d_{lmn}\left(1 - j\tan\theta'_{lmn}\right) \tag{5.1.4}$$

5.2 Off-resonance dielectric measurements

There is no issue in the IEEE standard of piezoelectricity for the dielectric measurements. However, the reliability of the measurements can be dramatically enhanced with additional analysis. Using the effective k_{31}-k_{15} structure, the intensive dielectric permittivity and corresponding losses along the 33-direction and 11-direction can be obtained with the following equations, where $0 \le \gamma_1 < \gamma_2 \le \pi/2$.

$$\varepsilon^{X}_{33} = \frac{\sin^2(\gamma_2)\,\varepsilon^{X}_{33,eff}(\gamma_1) - \sin^2(\gamma_1)\,\varepsilon^{X}_{33,eff}(\gamma_2)}{\sin(\gamma_2+\gamma_1)\sin(\gamma_2-\gamma_1)} \tag{5.2.1}$$

$$\varepsilon^{X}_{11} = \frac{\cos^2(\gamma_1)\,\varepsilon^{X}_{33,eff}(\gamma_2) - \cos^2(\gamma_2)\,\varepsilon^{X}_{33,eff}(\gamma_1)}{\sin(\gamma_2+\gamma_1)\sin(\gamma_2-\gamma_1)} \tag{5.2.2}$$

$$\tan\delta'_{33} = \frac{\begin{bmatrix}\sin^2(\gamma_2)\,\varepsilon^X_{33,eff}(\gamma_1)\tan\delta'_{33,eff}(\gamma_1) \\ -\sin^2(\gamma_1)\,\varepsilon^X_{33,eff}(\gamma_2)\tan\delta'_{33,eff}(\gamma_2)\end{bmatrix}}{\varepsilon^X_{33}\,\sin(\gamma_2+\gamma_1)\sin(\gamma_2-\gamma_1)} \tag{5.2.3}$$

$$\tan\delta'_{11} = \frac{\begin{bmatrix}\cos^2(\gamma_1)\,\varepsilon^X_{33,eff}(\gamma_2)\tan\delta'_{33,eff}(\gamma_2) \\ -\cos^2(\gamma_2)\,\varepsilon^X_{33,eff}(\gamma_1)\tan\delta'_{33,eff}(\gamma_1)\end{bmatrix}}{\varepsilon^X_{11}\,\sin(\gamma_2+\gamma_1)\sin(\gamma_2-\gamma_1)} \tag{5.2.4}$$

5.3 Effective k_{31} mode analysis

The next step is to analyze the effective k_{31} vibration mode. Defining the effective quadrantal resonance frequency ($f_{\mathrm{Aq},31,\mathrm{eff}}(\gamma)$) where the conductivity G is maximum [12], [74], the effective s_{11}^E with γ degree canted polarization ($s_{11,\mathrm{eff}}^{\mathrm{E}}(\gamma)$) can be obtained via equation 5.3.1. When setting the vibration length to 15mm, the effective k_{31} mode should occur near 100kHz for typical PZT-based ceramics, similar to the results in Chapter 3.

$$s^E_{11,\mathrm{eff}}(\gamma) = \frac{v^2_{11,\mathrm{eff}}(\gamma)}{\rho} = \frac{1}{4f^2_{\mathrm{Aq},31,\mathrm{eff}}(\gamma)L^2\rho} \tag{5.3.1}$$

The elastic compliance along the 11- and 33- directions can be obtained from equation 5.3.2 and 5.3.3 where $0\leq\gamma_1<\gamma_2<\gamma_3<\pi/2$. Here ($i$) mod (n) is a modulus function which is equal to the remainder of i divided by n, where i, n and (i) mode (n) are natural numbers. The modulus function is used to simplify the equations. Although the s_{11}^{E} can be directly obtained from standard k_{31} mode structure, the equations below give more reliability in the analysis.

$$s_{11}^{E} = \frac{\sum_{i=1}^{3} \begin{bmatrix} \sin^2(\gamma_{(i)mod(3)+1}) \sin^2(\gamma_{(i+1)mod(3)+1}) \\ \cdot \sin(\gamma_{(i+1)mod(3)+1} + \gamma_{(i)mod(3)+1}) \\ \cdot \sin(\gamma_{(i+1)mod(3)+1} - \gamma_{(i)mod(3)+1}) \, s_{11,eff}^{E}(\gamma_i) \end{bmatrix}}{\sum_{i=1}^{3} \begin{bmatrix} \cos^4(\gamma_{(i+1)mod(3)+1}) \sin^2(\gamma_i) \sin^2(\gamma_{(i)mod(3)+1}) \\ \cdot \sin(\gamma_{(i)mod(3)+1} + \gamma_i) \sin(\gamma_{(i)mod(3)+1} - \gamma_i) \end{bmatrix}} \tag{5.3.2}$$

$$s_{33}^{E} = \frac{\sum_{i=1}^{3} \begin{bmatrix} \cos^2(\gamma_{(i)mod(3)+1}) \cos^2(\gamma_{(i+1)mod(3)+1}) \\ \cdot \sin(\gamma_{(i+1)mod(3)+1} + \gamma_{(i)mod(3)+1}) \\ \cdot \sin(\gamma_{(i+1)mod(3)+1} - \gamma_{(i)mod(3)+1}) \, s_{11,eff}^{E}(\gamma_i) \end{bmatrix}}{\sum_{i=1}^{3} \begin{bmatrix} \cos^4(\gamma_{(i+1)mod(3)+1}) \sin^2(\gamma_i) \sin^2(\gamma_{(i)mod(3)+1}) \\ \cdot \sin(\gamma_{(i)mod(3)+1} + \gamma_i) \sin(\gamma_{(i)mod(3)+1} - \gamma_i) \end{bmatrix}} \tag{5.3.3}$$

The simplified solution in Chapter 4 is identical with the above equations when $\gamma_1=0$ and $\gamma=\gamma_2=\pi/2-\gamma_3$.

The next step is to obtain the piezoelectric d_{31} constant. The effective electro-mechanical coupling factor can be calculated, thus the effective piezoelectric d_{31} constant can be obtained. The piezoelectric d_{31} constant can be calculated with equation 5.3.4 where $0 \leq \gamma_1 < \gamma_2 < \pi/2$.

$$d_{31} = \frac{\begin{bmatrix} \cos(\gamma_2) \sin^2(\gamma_2) \, d_{31,eff}(\gamma_1) \\ -\cos(\gamma_1) \sin^2(\gamma_1) \, d_{31,eff}(\gamma_2) \end{bmatrix}}{\cos(\gamma_1) \cos(\gamma_2) \sin(\gamma_2 + \gamma_1) \sin(\gamma_2 - \gamma_1)} \tag{5.3.4}$$

Additionally, the following values can be obtained for further analysis.

$$2s_{13}^{E}+s_{55}^{E}=\frac{\sum_{i=1}^{3}\begin{bmatrix}\{\sin^{4}(\gamma_{(i+1)mod(3)+1})\cos^{4}(\gamma_{(i)mod(3)+1})\\-\sin^{4}(\gamma_{(i)mod(3)+1})\cos^{4}(\gamma_{(i+1)mod(3)+1})\}\\\cdot s_{11,eff}^{E}(\gamma_{i})\end{bmatrix}}{\sum_{i=1}^{3}\begin{bmatrix}\cos^{2}(\gamma_{(i)mod(3)+1})\cos^{2}(\gamma_{(i+1)mod(3)+1})\\\cdot\sin^{4}(\gamma_{(i)})\sin(\gamma_{(i)mod(3)+1}+\gamma_{(i+1)mod(3)+1})\\\cdot\sin(\gamma_{(i)mod(3)+1}-\gamma_{(i+1)mod(3)+1})\end{bmatrix}} \tag{5.3.5}$$

$$d_{33}-d_{15}=\frac{\cos^{3}(\gamma_{2})\,d_{31,eff}(\gamma_{1})-\cos^{3}(\gamma_{1})\,d_{31,eff}(\gamma_{2})}{\cos(\gamma_{1})\cos(\gamma_{2})\sin(\gamma_{1}+\gamma_{2})\sin(\gamma_{1}-\gamma_{2})} \tag{5.3.6}$$

Next, the loss factors were analyzed. From the effective $Q_{A,31}$, the effective intensive elastic loss along 11-direction can be calculated as:

$$\tan\phi'_{11,eff}(\gamma)=\frac{1}{Q_{A,31,eff}(\gamma)} \tag{5.3.7}$$

Then, the independent elastic loss parameter along the 11- and 33-directions can be obtained with equation 5.3.8 and 5.3.9 respectively where $0\leq\gamma_1<\gamma_2<\gamma_3<\pi/2$.

$$\tan\phi'_{11}=\frac{\sum_{i=1}^{3}\begin{bmatrix}\sin^{2}(\gamma_{(i)mod(3)+1})\sin^{2}(\gamma_{(i+1)mod(3)+1})\\\cdot\sin(\gamma_{(i+1)mod(3)+1}+\gamma_{(i)mod(3)+1})\\\cdot\sin(\gamma_{(i+1)mod(3)+1}-\gamma_{(i)mod(3)+1})\\\cdot s_{11,eff}^{E}(\gamma_{i})\tan\phi'_{11,eff}(\gamma_{i})\end{bmatrix}}{s_{11}^{E}\sum_{i=1}^{3}\begin{bmatrix}\cos^{4}(\gamma_{(i+1)mod(3)+1})\sin^{2}(\gamma_{i})\sin^{2}(\gamma_{(i)mod(3)+1})\\\cdot\sin(\gamma_{(i)mod(3)+1}+\gamma_{i})\sin(\gamma_{(i)mod(3)+1}-\gamma_{i})\end{bmatrix}} \tag{5.3.8}$$

$$\tan\phi'_{33} = \frac{\sum_{i=1}^{3}\begin{bmatrix}\cos^2\left(\gamma_{(i)mod(3)+1}\right)\cos^2\left(\gamma_{(i+1)mod(3)+1}\right)\\ \cdot \sin\left(\gamma_{(i+1)mod(3)+1}+\gamma_{(i)mod(3)+1}\right)\\ \cdot \sin\left(\gamma_{(i+1)mod(3)+1}-\gamma_{(i)mod(3)+1}\right)\\ \cdot s^{E}_{11,eff}(\gamma_i)\tan\phi'_{11,eff}(\gamma_i)\end{bmatrix}}{s^{E}_{33}\sum_{i=1}^{3}\begin{bmatrix}\cos^4\left(\gamma_{(i+1)mod(3)+1}\right)\sin^2(\gamma_i)\sin^2\left(\gamma_{(i)mod(3)+1}\right)\\ \cdot \sin\left(\gamma_{(i)mod(3)+1}+\gamma_i\right)\sin\left(\gamma_{(i)mod(3)+1}-\gamma_i\right)\end{bmatrix}} \tag{5.3.9}$$

From the effective $Q_{B,31}$, the effective piezoelectric loss for effective k_{31} vibration can be calculated. Then, the independent piezoelectric loss tangent can be calculated with (5.3.10) where $0 \le \gamma_1 < \gamma_2 < \pi/2$.

$$\tan\theta'_{31} = \frac{\begin{bmatrix}\cos(\gamma_2)\sin^2(\gamma_2)\,d_{31,eff}(\gamma_1)\tan\theta'_{31,eff}(\gamma_1)\\ -\cos(\gamma_1)\sin^2(\gamma_1)\,d_{31,eff}(\gamma_2)\tan\theta'_{31,eff}(\gamma_2)\end{bmatrix}}{d_{31}\cos(\gamma_1)\cos(\gamma_2)\sin(\gamma_2+\gamma_1)\sin(\gamma_2-\gamma_1)} \tag{5.3.10}$$

The following values can be obtained for further analysis.

$$2s^{E}_{13}\tan\phi'_{13} + s^{E}_{55}\tan\phi'_{55} = \frac{\sum_{i=1}^{3}\begin{bmatrix}\{\sin^4\left(\gamma_{(i+1)mod(3)+1}\right)\cos^4\left(\gamma_{(i)mod(3)+1}\right)\\ -\sin^4\left(\gamma_{(i)mod(3)+1}\right)\cos^4\left(\gamma_{(i+1)mod(3)+1}\right)\}\\ \cdot s^{E}_{11,eff}(\gamma_i)\ \tan\phi'_{11,eff}(\gamma_i)\end{bmatrix}}{\sum_{i=1}^{3}\begin{bmatrix}\cos^2\left(\gamma_{(i)mod(3)+1}\right)\cos^2\left(\gamma_{(i+1)mod(3)+1}\right)\\ \cdot \sin^4\left(\gamma_{(i)}\right)\sin\left(\gamma_{(i)mod(3)+1}+\gamma_{(i+1)mod(3)+1}\right)\\ \cdot \sin\left(\gamma_{(i)mod(3)+1}-\gamma_{(i+1)mod(3)+1}\right)\end{bmatrix}} \tag{5.3.11}$$

$$d_{33}\tan\theta'_{33} - d_{15}\tan\theta'_{15} = \frac{\begin{bmatrix}\cos^3(\gamma_2)\,d_{31,eff}(\gamma_1)\tan\theta'_{31,eff}(\gamma_1)\\ -\cos^3(\gamma_1)\,d_{31,eff}(\gamma_2)\tan\theta'_{31,eff}(\gamma_2)\end{bmatrix}}{\cos(\gamma_1)\cos(\gamma_2)\sin(\gamma_1+\gamma_2)\sin(\gamma_1-\gamma_2)} \tag{5.3.12}$$

5.4 Effective d_{33} measurement

Next, with measurement of the effective d_{33} constant in the effective k_{31}-k_{15} geometry, the d_{33} constant can be obtained using equation 5.4.1.

$$d_{33} = d_{33,eff}(0) = \frac{\begin{bmatrix}\cos(\gamma_2)\sin^2(\gamma_2)\, d_{33,eff}(\gamma_1) \\ -\cos(\gamma_1)\sin^2(\gamma_1)\, d_{33,eff}(\gamma_2)\end{bmatrix}}{\cos(\gamma_1)\cos(\gamma_2)\sin(\gamma_1+\gamma_2)\sin(\gamma_1-\gamma_2)} \tag{5.4.1}$$

Then, the piezoelectric d_{15} constant can be obtained with equation 5.3.6 or 5.4.2.

$$d_{15} = -d_{31} + \frac{\cos^2(\gamma_2)\, d_{33,eff}(\gamma_1) - \cos^2(\gamma_1)\, d_{33,eff}(\gamma_2)}{\cos(\gamma_1)\cos(\gamma_2)\sin(\gamma_2+\gamma_1)\sin(\gamma_2-\gamma_1)} \tag{5.4.2}$$

In this way, all the real parameters essential for the k_{31}, k_{33} and k_{15} vibration modes are obtained. The next step is to analyze the imaginary parameters.

5.5 Effective k_{15} analysis

Assume that a clear half-circle of motional admittance and impedance could be obtained at polarization angles of γ_A and γ_B, respectively. At first, with the obtained antiresonance frequency of the effective shear vibration with γ_B canted polarization, the effective electro-mechanical coupling factor can be obtained from equation 5.5.2.

$$s^D_{55,eff}(\gamma_B) = \frac{1}{4t^2\rho f^2_{B,eff}(\gamma_B)} \tag{5.5.1}$$

$$\frac{k_{15,eff}^2(\gamma_B)}{1-k_{15,eff}^2(\gamma_B)} = \frac{d_{15,eff}^2(\gamma_B)}{\varepsilon_0 \varepsilon_{11,eff}^X(\gamma_B) \cdot s_{55,eff}^D(\gamma_B)} \tag{5.5.2}$$

Then, s_{13}^E and s_{55}^E can be obtained from equation 5.3.5 and 5.5.3.

$$\frac{s_{55,eff}^D(\gamma_B)}{1-k_{15,eff}^2(\gamma_B)} = \sin^2(2\gamma_B)\,(s_{11}^E + s_{33}^E - 2s_{13}^E) + \cos^2(2\gamma_B)\, s_{55}^E \tag{5.5.3}$$

The effective $Q_B(\gamma_B)$ satisfies the following relation with the effective coupling factor and loss parameters.

$$\frac{1-k_{15,eff}^2(\gamma_B)}{k_{15,eff}^2(\gamma_B)} \cdot \frac{1}{Q_{B,eff}(\gamma_B)} = \tan\delta'_{11,eff}(\gamma_B) - 2\tan\theta'_{15,eff}(\gamma_B) + \frac{\tan\phi'_{55,eff}(\gamma_B)}{k_{15,eff}^2(\gamma_B)} \tag{5.5.4}$$

From the resonance frequency obtained from the γ_A polarization-canted structure, the corresponding anti-resonance frequency can be predicted from equations 5.5.5 and 5.5.6. Thus, the effective electro-mechanical coupling factor can be obtained.

$$k_{15,eff}^2(\gamma_A) = \frac{d_{15,eff}^2(\gamma_A) 4t^2 \rho f_{B,eff}^2(\gamma_A)}{d_{15,eff}^2(\gamma_A) 4t^2 \rho f_{B,eff}^2(\gamma_A) + \varepsilon_0 \varepsilon_{11,eff}^X(\gamma_A)} \tag{5.5.5}$$

$$k_{15,eff}^2(\gamma_A) = \frac{\pi}{2}\frac{f_{A,eff}(\gamma_A)}{f_{B,eff}(\gamma_A)} \cot\left[\frac{\pi}{2}\frac{f_{A,eff}(\gamma_A)}{f_{B,eff}(\gamma_A)}\right] \tag{5.5.6}$$

Then, the effective $Q_A(\gamma_A)$ satisfies the following relation as a function of the effective coupling factor, A- and B-type resonance frequencies and loss parameters.

$$\frac{1-k_{15,eff}^2(\gamma_A)}{Q_{A,eff}(\gamma_A)}\cdot\left[k_{15,eff}^2(\gamma_A)-1+\tan^2\left\{\frac{\pi}{2}\frac{f_{A,eff}(\gamma_A)}{f_{B,eff}(\gamma_A)}\right\}\right]$$

$$=\left[k_{15,eff}^4(\gamma_A)+k_{15,eff}^2(\gamma_A)+\left\{\frac{\pi}{2}\frac{f_{A,eff}(\gamma_A)}{f_{B,eff}(\gamma_A)}\right\}^2-2\right]\tan\delta'_{11,eff}(\gamma_B)$$

$$+\left[3k_{15,eff}^2(\gamma_A)+\tan^2\left\{\frac{\pi}{2}\frac{f_{A,eff}(\gamma_A)}{f_{B,eff}(\gamma_A)}\right\}-3\right]\tan\phi'_{55,eff}(\gamma_B)$$

$$+\Bigg[4-2k_{15,eff}^4(\gamma_A)-2k_{15,eff}^2(\gamma_A)$$

$$-2\left\{\frac{\pi}{2}\frac{f_{A,eff}(\gamma_A)}{f_{B,eff}(\gamma_A)}\right\}^2\Bigg]\tan\theta'_{15,eff}(\gamma_B) \qquad (5.5.7)$$

Since the effective loss parameters are functions of the independent loss parameters as indicated in equation 5.1.2 to 5.1.4, tanϕ'$_{13}$, tanϕ'$_{55}$, tanθ'$_{33}$ and tanθ'$_{15}$ can be obtained from equation 5.3.11, 5.3.12, 5.5.4 and 5.5.7. Resultingly, the intensive loss parameters for k_{31}, k_{33} and k_{15} vibration mode can be separately derived.

Chapter 6

Anisotropic properties with proposed methodology

6.1 The vibration mode separation

As a prerequisite of the proposed analysis, it should be verified that mode coupling does not occur near the effective k_{31} and k_{15} vibrations [75], [76]. An intensive study of each vibration mode was conducted. Impedance and phase spectrum were analyzed from 50kHz to 4MHz (5.2MHz for rhombohedral PNZT) with the HiPoCS™ under a constant voltage of 0.5V for each structure as shown in Figure 6.1.1 (a), (b) and (c).

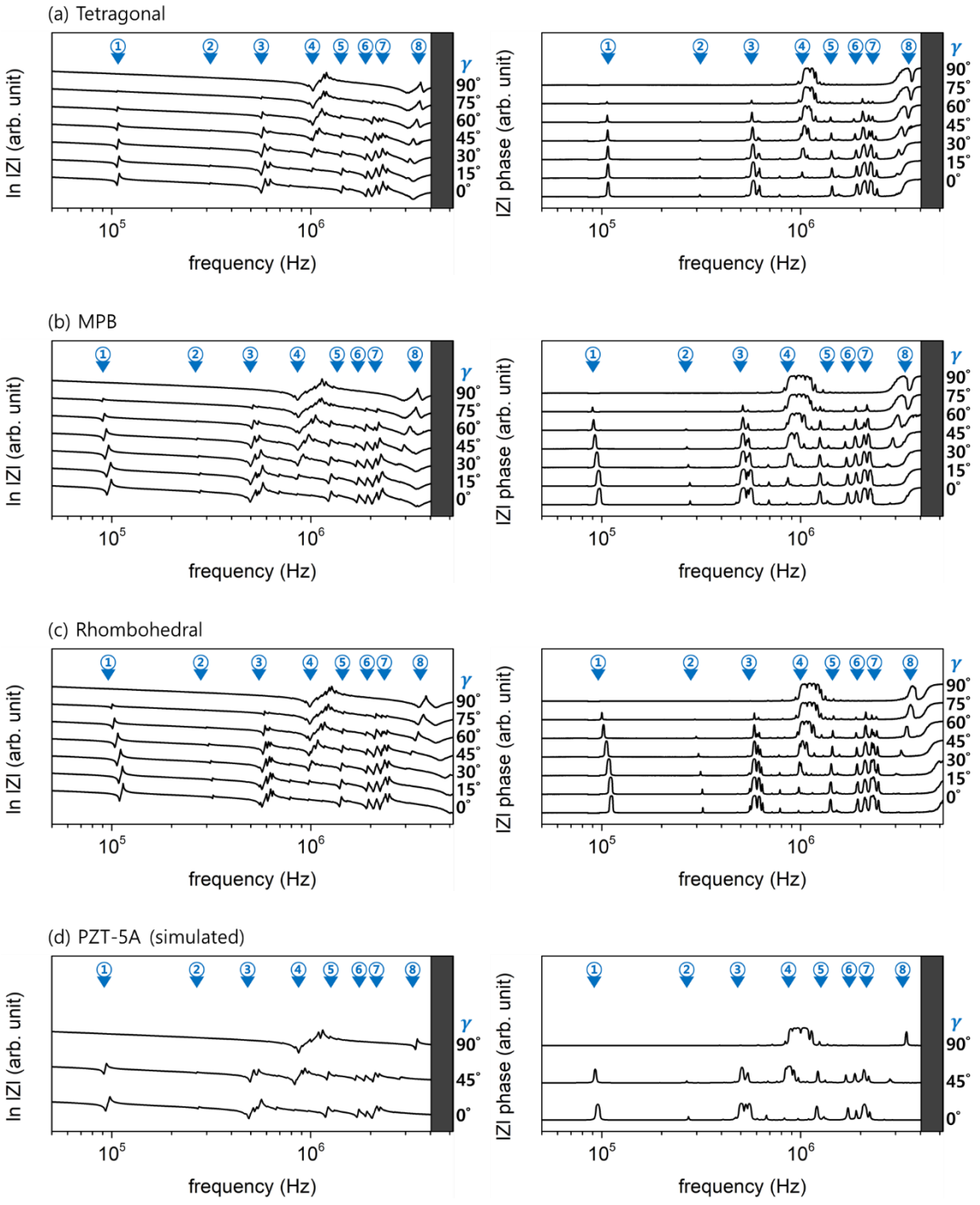

Figure 6.1.1. Impedance and phase spectrum of (a) tetragonal, (b) MPB and (c) rhombohedral PNZT measured with HiPoCS™ and (d) PZT5A simulated with ATILA/GiD.

ATILA/GiD simulations of PZT-5A were conducted to analyze the vibration modes as shown in Figure 6.1.1 (d). The vibration modes are consistent in simulation and measurements and the effective k_{31} and k_{15} mode were separated from other vibration modes. The effective vibration modes labeled in Figure 6.1.1 are the ① k_{31} mode, ② 2nd order k_{31} mode, ③ k_{32} mode, ④ k_{15} mode, ⑤ sub-mode of coupled k_t and 2nd order k_{32} mode, ⑥ 2nd order k_{32} mode, ⑦ k_t mode and ⑧ 2nd order k_{15} mode. The 2nd order k_{32} mode and k_t mode are calculated to occur at higher frequency than the k_{15} mode, however it is interesting to observe a sub-vibration mode which is a coupled mode of k_t and the 2nd order k_{32} mode. The displacement distribution of important vibration modes are simulated with ATILA/GiD software as shown in Figure 6.1.2. Since the necessary vibration modes are separated, further analysis could be made.

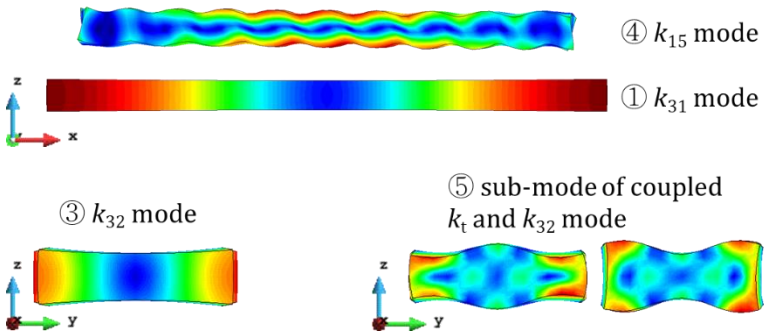

Figure 6.1.2. Simulated displacement distributions of vibration modes shown in Figure 6.1.1.

6.2 The independent parameters

Now, the anisotropic properties were obtained with the proposed methodology in Chapter 5. Figure 6.2.1 shows the obtained dielectric properties. The results of dielectric properties are in good agreement with the measured data in Chapter 3.

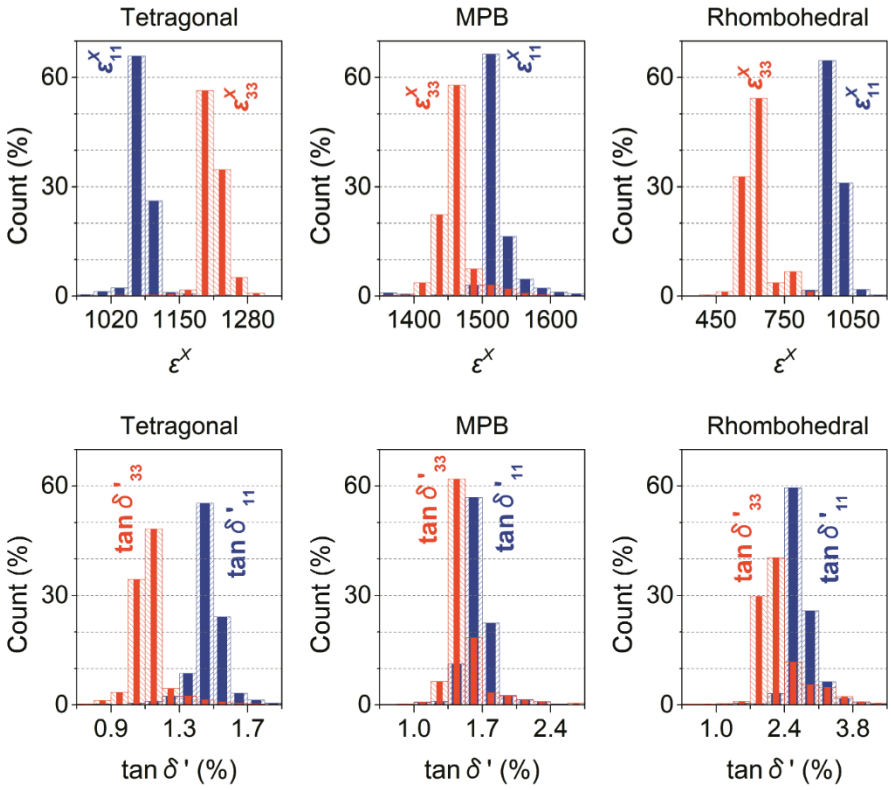

Figure 6.2.1. Histogram of dielectric properties obtained with the proposed method.

The elastic properties calculated from the effective k_{31} mode data are shown in Figure 6.2.2. The elastic compliance along the polarization direction is higher than the one perpendicular to the polarization especially in MPB and rhombohedral PNZT. It is usual for PZT ceramics that $s_{55}>s_{33}>s_{11}$ due to the P6mm symmetry achieved from poling [77]. It is known that poled rhombohedral ceramics have greater elastic anisotropy than the tetragonal ceramics in spite of the smaller distortion of the crystal from cubic symmetry [58], [78]–[80]. The intensive elastic loss shows larger anisotropy in the rhombohedral than tetragonal phase, similar to the real parameter. However, the elastic loss could be considered as constant for the two directions regardless of the structure, compared to the dielectric loss anisotropy.

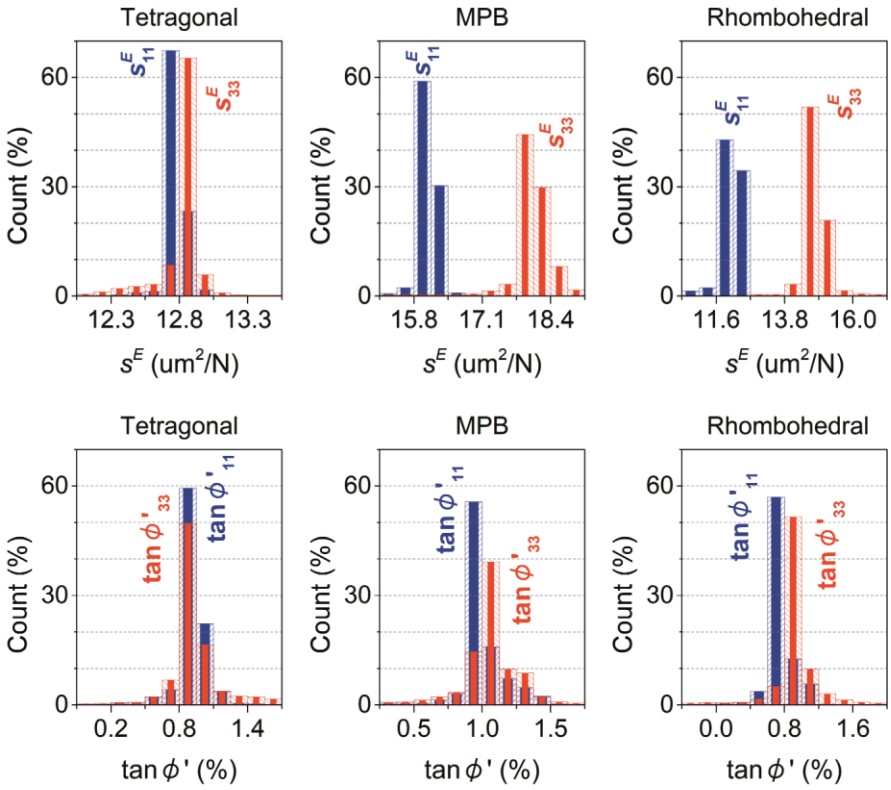

Figure 6.2.2. Histogram of elastic properties obtained from effective k_{31} structures.

Next, the effective d_{33} were measured at 110Hz with a PM200 d_{33} meter (Piezotest, UK) under a static force of 10N and dynamic force of 0.25N. Consequently, the piezoelectric d constants could be obtained as shown in Figure 6.2.3. The piezoelectric anisotropy is largest in rhombohedral and smallest in tetragonal PNZT as shown in Table 6.2.1.

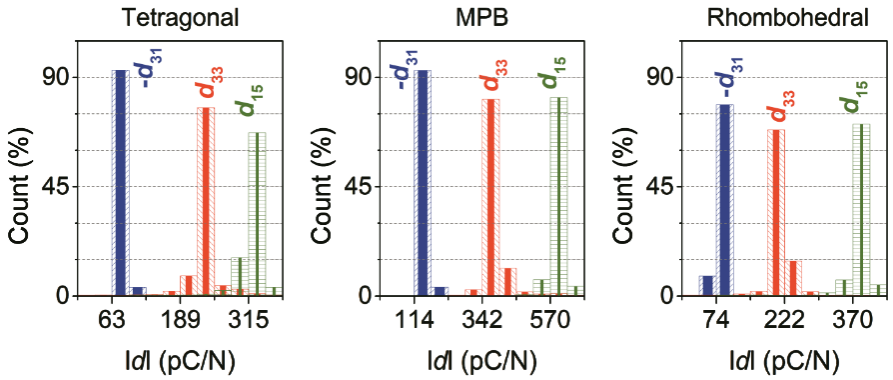

Figure 6.2.3. Histogram of obtained piezoelectric *d* constants.

Table 6.2.1. Piezoelectric anisotropy ratios of PNZT.

	Tetragonal	MPB	Rhombohedral
d_{15}/d_{33}	1.38	1.52	1.77
$-d_{15}/d_{31}$	3.59	4.01	4.95
$-d_{33}/d_{31}$	2.60	2.64	2.80

The intensive piezoelectric loss for k_{31} mode is shown in Figure 6.2.4. The transverse piezoelectric loss is largest in rhombohedral and smallest in tetragonal PNZT. Considering the dielectric and elastic loss factors, the mechanical quality factor difference between the transverse resonance and antiresonance frequencies is the highest for rhombohedral PNZT due to the large piezoelectric loss.

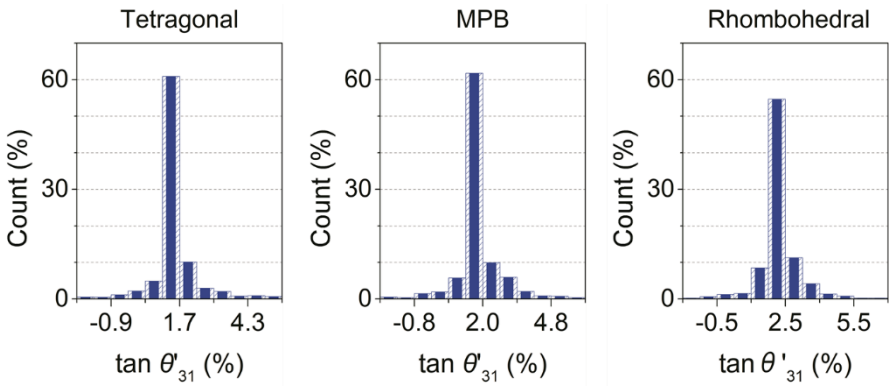

Figure 6.2.4. Histogram of obtained piezoelectric loss tanθ'$_{31}$.

Now, the independent elastic and piezoelectric loss of k_{15} and k_{33} mode should be obtained. The effective shear modes were analyzed with HiPoCS^{TM} under a 0.1mW of constant power condition to avoid peak distortion, since the shear vibration could not be accurately traced with the laser Doppler vibrometer. The admittance / impedance near resonance and antiresonance frequencies were measured at 1Hz interval and the distortion of the half-circle was analyzed. Figure 6.2.5 shows the motional admittance and impedance in the range of 0.93 to 1.33MHz of rhombohedral with various polarization orientations. As indicated in the figure, the half circle with the least distortion was observed at γ = 60° and 75° for motional admittance and impedance, respectively.

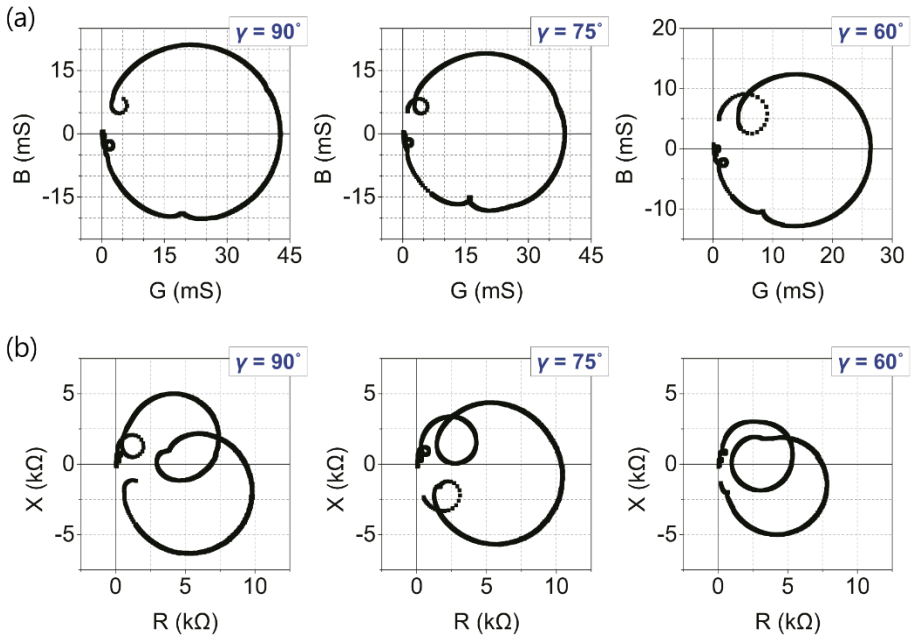

Figure 6.2.5. (a) Admittance and (b) impedance circle near effective k_{15} shear mode where the angle between polarization and applied electric field is 90, 75 or 60 degrees.

Table 6.2.2 shows the angle between the polarization and applied electric field for the most undistorted geometries for each structure and the resulting effective resonance frequencies and corresponding quality factors. For the admittance circle, the conductance of the frequencies where

the susceptance is maximum or minimum needs to be in a similar range when undistorted. For the impedance circle, the resistance of the frequencies where the reactance is maximum or minimum needs to be in a similar range when undistorted. Then, assigning an imaginary center of the circles, the standard deviation of the relative radius was checked, and the least distorted measurement data were taken from ten samples of each. The measured errors were 0.1%, 5%, 0.2% and 10% for f_A, Q_A, f_B and Q_B, respectively.

Table 6.2.2. The obtained effective shear mode properties of the least distorted geometries.

	Tetragonal		MPB		Rhombohedral	
	A-type	B-type	A-type	B-type	A-type	B-type
γ (degree)	90	60	90	90	60	75
Resonance frequency (kHz)	1027.4	1137.5	860.25	1136.5	994.38	1227.2
Quality factor	57.2	105	47.5	106	90.5	109

Consequently, the intensive elastic and piezoelectric loss factors for k_{33} and k_{15} mode could be obtained. The obtained independent parameters are shown in Table 6.2.3. Note the only remaining unknown parameter s_{12}^E and the corresponding elastic loss can be obtained from k_p mode structures with the standard method, if necessary.

Table 6.2.3. The independent parameters obtained with the proposed method.

Tetragonal	ε_{33}^{X}	1213	ε_{11}^{X}	1079	s_{13}^{E} (μm²/N)	-3.72
	tanδ'$_{33}$ (%)	1.11	tanδ'$_{11}$ (%)	1.46	tanϕ'$_{13}$ (%)	4.52
	s_{11}^{E} (μm²/N)	12.77	s_{33}^{E} (μm²/N)	12.84	s_{55}^{E} (μm²/N)	32.83
	tanϕ'$_{11}$ (%)	0.91	tanϕ'$_{33}$ (%)	0.90	tanϕ'$_{55}$ (%)	1.88
	d_{31} (pC/N)	-90	d_{33} (pC/N)	233	d_{15} (pC/N)	322
	tanθ'$_{31}$ (%)	1.51	tanθ'$_{33}$ (%)	3.03	tanθ'$_{15}$ (%)	3.10
MPB	ε_{33}^{X}	1455	ε_{11}^{X}	1516	s_{13}^{E} (μm²/N)	-8.01
	tanδ'$_{33}$ (%)	1.48	tanδ'$_{11}$ (%)	1.62	tanϕ'$_{13}$ (%)	4.40
	s_{11}^{E} (μm²/N)	16.09	s_{33}^{E} (μm²/N)	18.06	s_{55}^{E} (μm²/N)	51.41
	tanϕ'$_{11}$ (%)	0.96	tanϕ'$_{33}$ (%)	1.04	tanϕ'$_{55}$ (%)	2.19
	d_{31} (pC/N)	-148	d_{33} (pC/N)	391	d_{15} (pC/N)	593
	tanθ'$_{31}$ (%)	1.73	tanθ'$_{33}$ (%)	2.63	tanθ'$_{15}$ (%)	2.50
Rhombohedral	ε_{33}^{X}	604	ε_{11}^{X}	950	s_{13}^{E} (μm²/N)	-5.13
	tanδ'$_{33}$ (%)	2.11	tanδ'$_{11}$ (%)	2.67	tanϕ'$_{13}$ (%)	1.64
	s_{11}^{E} (μm²/N)	12.15	s_{33}^{E} (μm²/N)	14.75	s_{55}^{E} (μm²/N)	37.48
	tanϕ'$_{11}$ (%)	0.74	tanϕ'$_{33}$ (%)	0.89	tanϕ'$_{55}$ (%)	1.30
	d_{31} (pC/N)	-77	d_{33} (pC/N)	217	d_{15} (pC/N)	383
	tanθ'$_{31}$ (%)	2.04	tanθ'$_{33}$ (%)	1.28	tanθ'$_{15}$ (%)	2.24

Figure 6.2.6 shows the piezoelectric loss for different vibration modes. It is interesting to note that the piezoelectric loss appeared to be the smallest in rhombohedral and the largest in tetragonal PNZT in the k_{33} and k_{15} vibration modes. In contrast, the piezoelectric loss appeared to be the largest in rhombohedral and the smallest in tetragonal PNZT for the k_{31} vibration. According to the results, the vibration mode should be considered as an important variable to discuss the piezoelectric loss anisotropy.

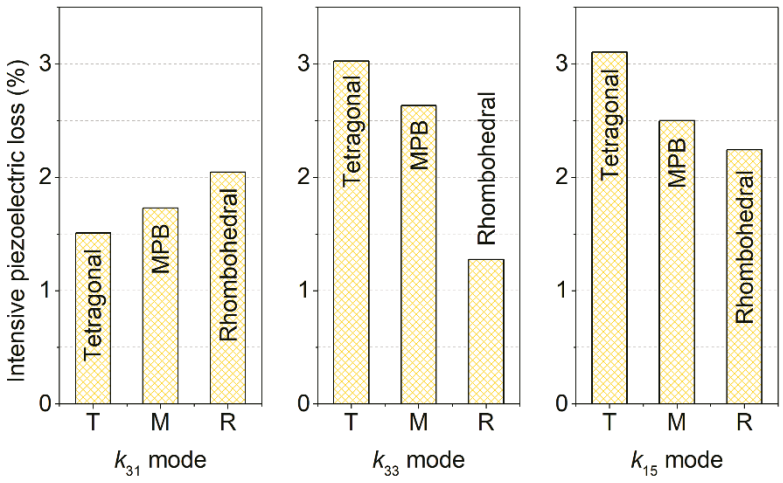

Figure 6.2.6. Piezoelectric loss in various PNZT crystal structures for k_{31}, k_{33} and k_{15} vibration modes.

Table 6.2.4 compares the piezoelectric loss of measured PNZT to the conventional studies. Note that the conventional studies contain large measurement error in k_{33} and k_{15} modes due to the small capacitance and spurious peaks. Miguel Alguero et al. reported the anisotropic piezoelectric loss in Navy type II (PZ27) ceramics by analyzing the admittance and impedance at length, shear, thickness and radial resonance [81]. Here, the larger piezoelectric loss was reported with larger piezoelectric *d* constant, similar to the tetragonal PNZT. The author noted an additional limitation of analysis due to the inconsistent poling in different geometries. Yuan Zhuang et al. reported the loss anisotropy in soft (APC850) [39] and hard (APC841) [82] piezoelectric ceramics using the 3dB method [38]. It is notable that in APC 841 and APC 850 ceramics have smaller piezoelectric loss under k_{33} vibration than k_{31} vibration, similar to the rhombohedral PNZT.

Table 6.2.4. The anisotropic piezoelectric parameters of PNZT, PZ27, APC850 and APC841.

	$-d_{31}$ (pC/N)	$\tan\theta'_{31}$ (%)	d_{33} (pC/N)	$\tan\theta'_{33}$ (%)	d_{15} (pC/N)	$\tan\theta'_{15}$ (%)
Tetragonal PNZT	90	1.51	233	3.03	322	3.10
Rhombohedral PNZT	77	2.04	217	1.28	383	2.24
MPB PNZT	148	1.73	391	2.63	593	2.50
PZ27 [81]	160	1.94	336	2.14	396	6.62
APC 850 [39]	196	1.84	416	1.78	649	2.96
APC 841 [82]	109	3.7	300	2.5	450	-

6.3 Polarization dependence of properties

From the obtained independent parameters, a transformation matrix was used to analyze the polarization dependence of the dielectric, elastic and piezoelectric properties. The intensive dielectric properties as a function of polarization orientation are shown in Figure 6.3.1. Note that the shear mode properties are plotted from 90 to 0 degrees since the 90 degree angled polarization from the applied field is the standard geometry for the shear vibration. The results of dielectric properties are in good agreement with the standard analysis in Chapter 3. The effective dielectric permittivity or loss gradually changes from ε_{33}^{X} or $\tan\delta'_{33}$ to ε_{11}^{X} or $\tan\delta'_{11}$ by increasing the angle between polarization and electric field.

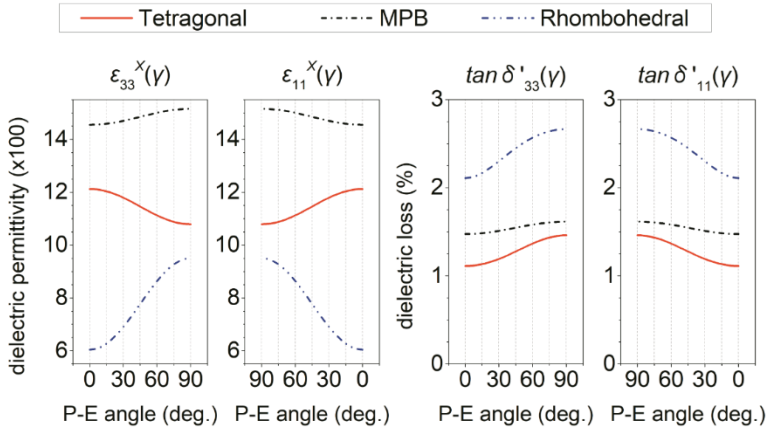

Figure 6.3.1. Intensive dielectric properties by polarization orientation.

In figure 6.3.2, the intensive elastic properties by polarization orientation are shown for the effective k_{31}, k_{33} and k_{15} vibration modes. The imaginary parameters of k_{33} mode differs from the preliminary analysis in chapter 3 by resolving the relative error and giving a physical picture that the intensive elastic compliance for linear vibration changes in between s_{11}^{E} to s_{33}^{E} depending on the polarization orientation. It is interesting to note that the elastic shear property becomes more compliant in tetragonal PNZT while it is stiffer in rhombohedral and MPB PNZT with a canted polarization. The major reason is from the property anisotropy where $(s_{11}^{E}+s_{33}^{E}-2s_{13}^{E})/s_{55}^{E}$ is larger than 1 in the tetragonal phase, while it is smaller than 1 in rhombohedral and MPB PNZT. It is also interesting to note that the elastic loss for transverse and longitudinal modes shows a maximum while the loss for the shear mode shows a minimum when the polarization angle is canted near 45 degrees.

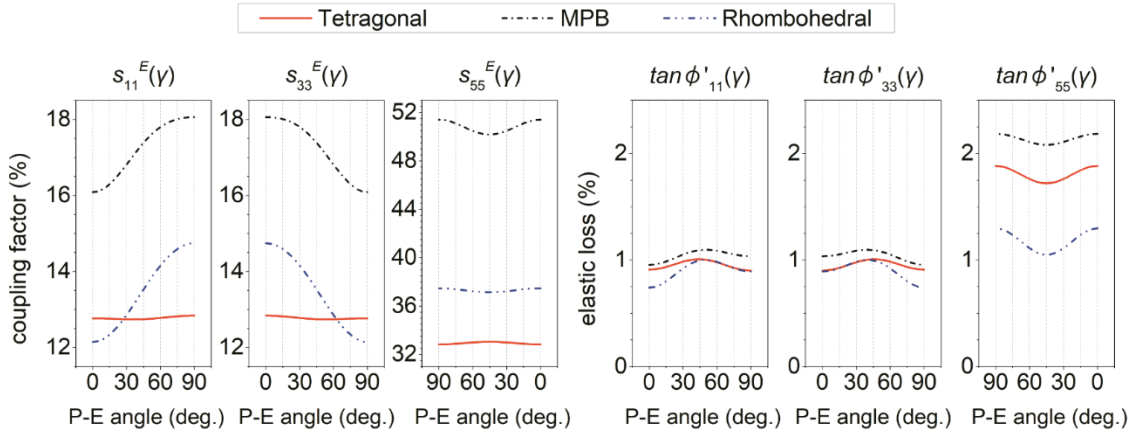

Figure 6.3.2. Intensive elastic properties by polarization orientation.

The degradation of piezoelectric *d* constants with angled polarization is shown in Figure 6.3.3. A slight enhancement of d_{31} was observed in rhombohedral PNZT due to the high value of $(d_{33}\text{-}d_{15})/d_{31}$. More piezoelectric loss was observed when the polarization is canted for linear vibration as opposed to the shear vibration mode. The change of piezoelectric loss was smallest in MPB PNZT, which is the most isotropic. Tetragonal PNZT showed the largest polarization orientation dependence of the piezoelectric loss for the k_{31} vibration mode, while rhombohedral PNZT showed the largest polarization orientation dependence of the piezoelectric loss for the k_{15} vibration mode.

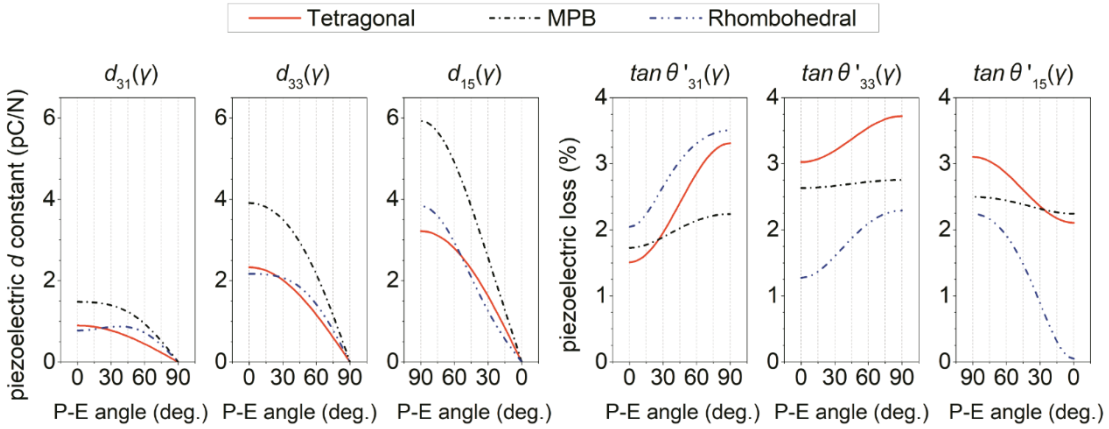

Figure 6.3.3. Intensive piezoelectric properties by polarization orientation.

Chapter 7

Polarization dependence of extensive loss factors

7.1 Introduction

Considering the internal state of ceramics, the boundary conditions are mechanically clamped (constant *x*) and electrically open-circuited (constant *D*), corresponding to the extensive parameters. Since the extensive loss parameters are occasionally employed to explain the origin of losses [83], it is important to understand the extensive loss behaviors with respect to the polarization orientation. As introduced in section 1.3, the extensive loss parameters in the k_{15} vibration mode is directly obtainable, while the extensive losses in the k_{31} mode could be calculated from the directly obtained intensive loss parameters assuming the 1-dimensional reciprocal relation, $c_{11}^{D}=1/s_{11}^{D}$. In k_{33} mode, the boundary condition is generally considered as strain constant along the polarization direction. However, the assumption is only valid when the coupling factor k_{33} is near 100%. Neither stress nor strain are constant in the k_{33} mode for a typical piezoelectric ceramic. Thus, the measurable parameters of the k_{33} mode are neither intensive nor extensive loss factors, but intermediate values. Therefore, only the extensive loss parameters in the k_{31} and k_{15} modes will be discussed.

7.2 Extensive loss parameters by polarization orientation

The extensive loss parameters were calculated using the *K* matrix consist of the effective intensive loss parameters and the effective electro-mechanical coupling factor, as shown in Figure

7.2.2. The maximum, minimum and average measured data for each geometry for effective k_{31} mode is plotted for comparison.

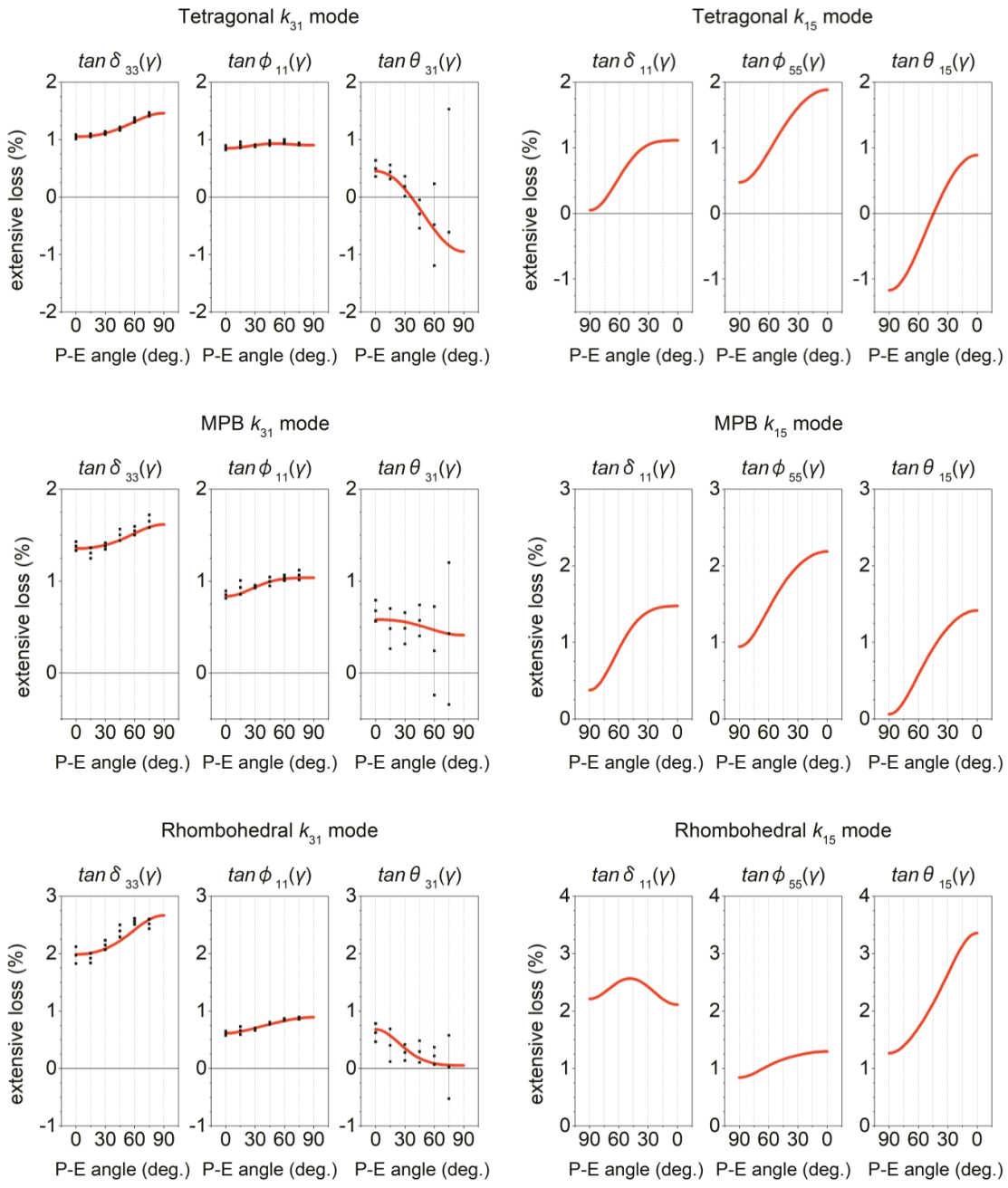

Figure 7.2.1. Extensive loss parameters for effective k_{31} and k_{15} vibration.

Considering an open-circuit condition, due to the different charge development in different vibration modes, the effective dielectric loss varies ($\tan\delta_{11}(\gamma)\neq\tan\delta_{33}(\pi/2-\gamma)$). Note that in the short-circuited condition where the charge could be well distributed, the effective dielectric loss is mode-independent ($\tan\delta'_{11}(\gamma)=\tan\delta'_{33}(\pi/2-\gamma)$). A similar phenomenon is observed for the elastic loss factor.

The extensive dielectric and elastic loss are mostly higher when the polarization is angled from the standard structure of each resonator, except for the shear mode in rhombohedral PNZT. The piezoelectric loss is more related with the angle between polarization and applied electric field. The piezoelectric loss is smaller when the angle is larger, meaning the compensation to the dielectric and elastic loss is smaller when the polarization is canted from the applied field. This phenomenon could be a very important point for further study on domain dynamics. The changes are least in MPB PNZT, which is the most isotropic. In the effective k_{31} mode, the change of extensive piezoelectric loss is the largest in tetragonal PNZT which is the least isotropic. In the effective k_{15} mode, the change of extensive piezoelectric loss is the largest in rhombohedral PNZT which has the strongest relative shear property, as indicated in Table 6.2.1.

It is interesting to note that the extensive piezoelectric loss becomes negative in tetragonal PNZT when the polarization is strongly canted with respect to the applied electric field. The negative piezoelectric loss will be discussed further in the following section.

7.3 Extensive loss contribution to intensive elastic loss

Dragan Damjanovic provided a thermodynamically possible explanation for a negative piezoelectric loss in [84]. Unlike dielectric or elastic hysteresis, which always rotates counterclockwise for a positive compliance, the piezoelectric hysteresis could rotate

counterclockwise or clockwise, since the hysteresis does not have energy-density units. The counterclockwise or clockwise hysteresis corresponds to the positive or negative piezoelectric loss. A schematic illustration of the hysteresis is shown in Figure 7.3.1.

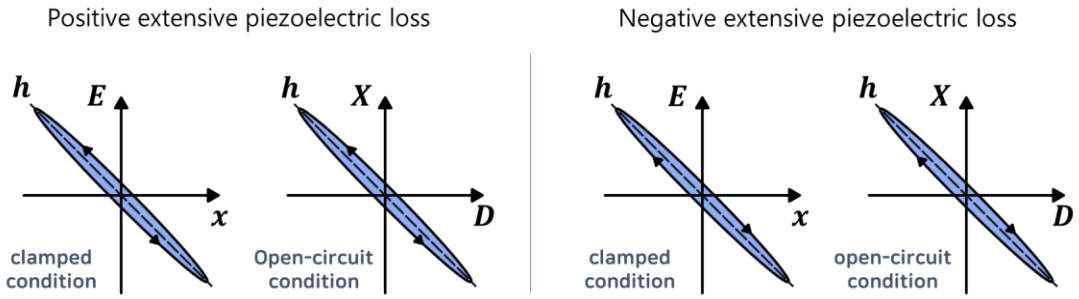

Figure 7.3.1. Hysteresis loop for positive and negative extensive piezoelectric loss.

A negative loss at low frequency model has been studied [85] through a bi-layer structure. However, this dissertation is the first report of a negative piezoelectric loss at high-frequencies near resonance (~100kHz for k_{31} mode and ~1MHz for k_{15} mode). From equation 1.1.7, the phase lag of the electro-mechanical coupling factor becomes:

$$\frac{k''}{k'} = \frac{-2\tan\theta + \tan\delta + \tan\phi}{2} \tag{7.3.1}$$

Here, k' and k'' are the real and imaginary parameters of the electro-mechanical coupling factor. This phase lag results in the difference of Q_A and Q_B in equations 1.3.8 and 1.3.9. Here, the piezoelectric loss compensates the elastic and dielectric loss when all parameters are positive. However when the piezoelectric loss is negative, the piezoelectric loss is added to the phase lag, resulting in an increase of the total loss. This phenomenon could be obtained by segmenting the

intensive elastic loss with extensive loss parameters using the *K* matrix. Figure 7.3.2 shows the contribution of extensive loss factors for the intensive elastic loss in effective k_{31} and k_{15} mode.

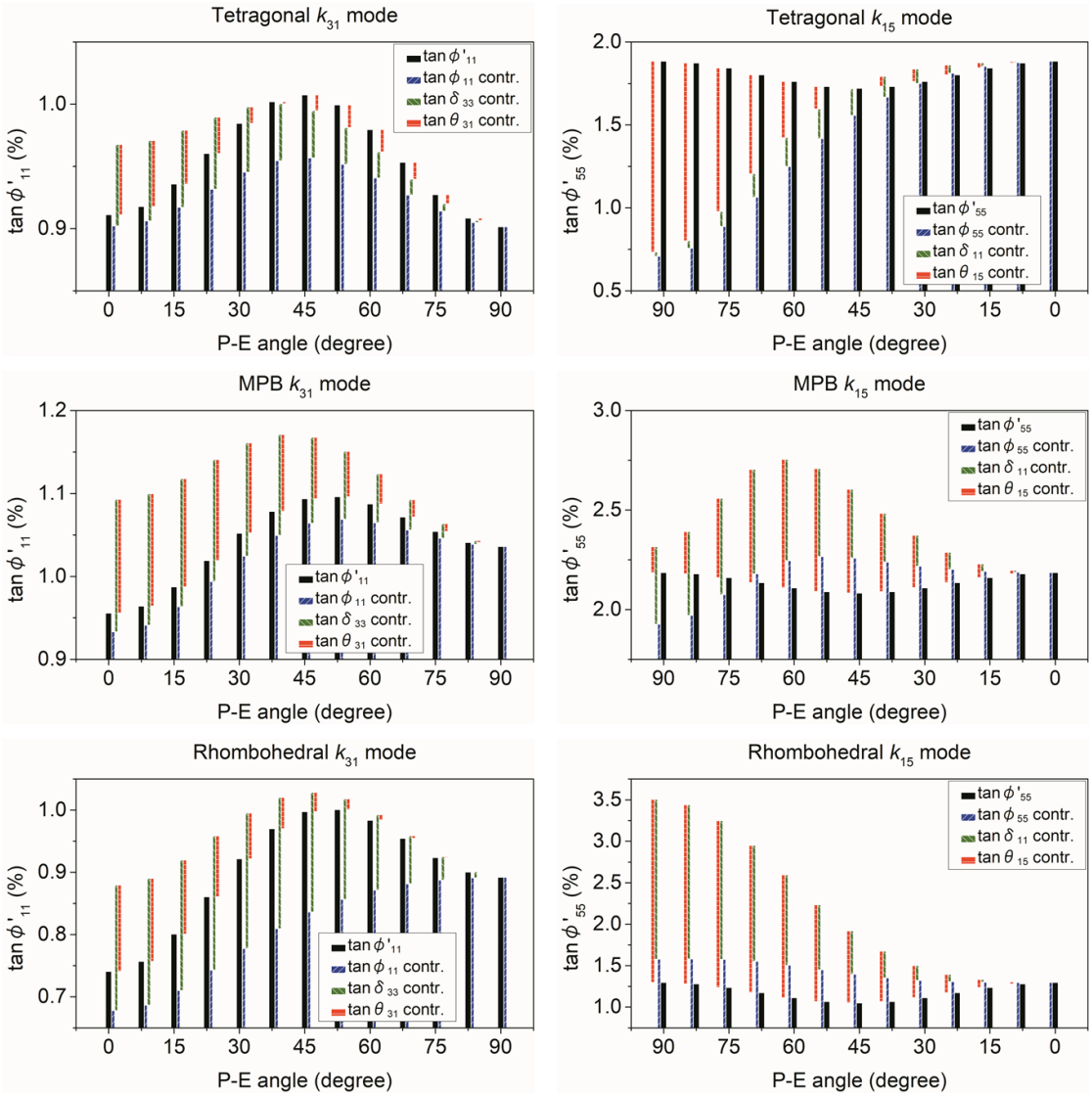

Figure 7.3.2. Extensive loss contribution to intensive elastic loss in effective k_{31} and k_{15} vibration.

It is shown in most structures that the piezoelectric loss tends to compensate other losses, acting to lower the overall intensive elastic loss. However in tetragonal PNZT with a strongly canted-polarization, the piezoelectric loss adds more phase lags to boost the overall intensive elastic

loss. With the diminishing electro-mechanical coupling, the intensive and extensive elastic loss becomes the same.

Chapter 8

Summary and future work

8.1 Summary

Loss in ferroelectric and piezoelectric media is a challenging topic which is still rather superficially quantified if not understood. Assuming the origin of loss is from domain dynamics, it is essential to understand the piezoelectric loss behavior by polarization orientation.

In this dissertation, the polarization orientation dependence of piezoelectric loss factors was studied for the k_{31}, k_{33} and k_{15} vibration modes from the phenomenological viewpoint. Tetragonal, MPB and rhombohedral PNZT ceramics were prepared in collaboration with PI Ceramic GmbH, Germany. Conventional ceramic processing was followed by angled dicing of poled blocks to build canted-polarization structures. It was verified with ATILA/GiD simulation that the post-dicing process has a negligible effect on the bulk property. By sputtering electrodes, ten of each effective k_{31}-k_{15} and k_{33}-k_{15} structures with canted polarization of 0, 15, 30, 45, 60, 75 and 90 degree angles were produced and analyzed [63].

Although a large change in the piezoelectric loss was observed as a function of the polarization angle, there are serious problems in the conventional characterization method (IEEE standard for real parameters and 3dB method for imaginary parameters) obstructing the reliability of the analysis. The first is a relative error from k_{33} mode structures due to the indirect calculation and large structural impedance. An approach using effective k_{31} mode vibration is suggested to obtain the elastic properties of the k_{33} mode since $s_{11}^{E}(\pi/2-\gamma)=s_{33}^{E}(\gamma)$. The feasibility of transformation matrix was verified for the elastic loss. As a result, highly reliable characterization could be made. Another shortcoming comes from the definition of quality factor using the 3dB

bandwidth as the half-power bandwidth. For the polarization-canted structures, the motional capacitance is relatively smaller than the standard samples and thus the damped capacitance cannot be neglected. The motional capacitance in piezoelectric ceramics with largely canted polarization is relatively smaller than the standard samples and thus damped capacitance cannot be neglected. Using only the motional part of admittance / impedance circle is suggested by taking quadrantal frequencies for the half-power bandwidth. The simulated results of ATILA/GiD simulation shows the extraordinary accuracy on loss calculations especially when the electro-mechanical coupling is small. Thus, the new definition of damping should be used for further research in loss.

Additionally, the shear mode could be separated from spurious modes, forming a clean half-circle of admittance / impedance with specific angle of polarization. The reason for this phenomenon is due to the change of effective compliance with polarization angle. Consequently, the effective shear mode properties could be analyzed without a concern of errors from spurious modes.

Using the aforementioned solutions, a new methodology to obtain anisotropic piezoelectric losses was proposed. Three effective k_{31}-k_{15} structures are essential for the method including selected angles of polarization for unaffected shear vibration. The proposed method is more reliable and not less convenient than analyzing the three samples of standard k_{31}, k_{33} and k_{15} structures. All independent dielectric, elastic and piezoelectric parameters including s_{13}^{E} and corresponding elastic loss are obtainable except s_{12}^{E} and $\tan\phi'_{12}$ which are irrelevant to the changes of piezoelectric loss factors by polarization orientation in polycrystalline samples.

To use the proposed method, the vibration modes were studied with ATILA/GiD FEA and compared to the measured impedance spectrum to assure that the effective k_{31} and k_{15} vibration modes are separated from other modes. Although the k_t mode and second order k_{32} mode appears at a much higher frequency range than fundamental shear mode, an additional coupled sub-mode of the k_t mode and second order k_{32} mode could be observed above the frequency range of shear

vibration. Thus, by choosing appropriate dimensions, the vibration mode separation was assured in all compositions. Consequently, all necessary anisotropic properties could be obtained. It was found that the anisotropy of piezoelectric loss is largest and elastic loss is the smallest. The dielectric loss is always smaller in the direction of polarization, regardless of the real parameter. However, the piezoelectric loss strongly depends on the vibration mode. The piezoelectric loss for the k_{31} mode is smallest in tetragonal and largest in rhombohedral PNZT. In contrast, the piezoelectric loss for k_{33} and k_{15} vibration is smallest in rhombohedral and largest in tetragonal PNZT. From the obtained anisotropic parameters, the polarization dependence of the loss factors is analyzed for k_{31}, k_{33} and k_{15} vibration modes. The dielectric loss gradually increases when the polarization is angled with respect to the applied electric field. The elastic loss is maximum in transverse or longitudinal vibration mode and minimum in the shear mode when the polarization angle is canted near 45 degrees. More piezoelectric loss was observed when the polarization is canted from the applied electric field, regardless of the vibration mode. The change of piezoelectric loss was smallest for the MPB PNZT, which is the most isotropic. It is noteworthy that in the standard vibration modes, the piezoelectric loss of the MPB PNZT is an interval value of the losses of the tetragonal and rhombohedral phases. Tetragonal PNZT showed the largest polarization orientation dependence of the piezoelectric loss for the k_{31} vibration mode while rhombohedral PNZT showed the largest for the k_{15} vibration mode.

The extensive loss parameters were calculated depicting the internal state of the material. Only k_{31} and k_{15} vibration modes were studied due to the boundary conditions to utilize the K matrix. Consequently, a negative extensive piezoelectric loss was discovered in tetragonal PNZT with strongly angled polarization with respect to the applied field. A schematic diagram of a clockwise hysteresis loop was shown to understand the negative loss. The negative loss has an important meaning that the piezoelectric loss does not compensate the elastic and dielectric losses but adds to the overall electro-mechanical coupling loss. The contribution of extensive dielectric, elastic and

piezoelectric losses on intensive elastic loss was studied. The extensive piezoelectric loss compensating or enhancing the intensive elastic loss is observed in tetragonal phase depending on the polarization orientation. The contribution of each loss factors differ by crystal structure and polarization orientation provides a scientific vista of loss mechanism.

8.2 Future work

In this dissertation, a methodology to obtain independent material properties were proposed using the effective k_{31} and k_{15} vibration modes. The effective shear parameters could be analyzed without concern about the spurious peaks. It could be achieved using a sample with a specific angle of polarization having resonance or antiresonance frequencies separated from unwanted modes. However, it solely depends on the measurement on one specific polarization orientation. The neglected error shown in Table 4.3.2 may result in an inaccurate analysis on the loss parameters in both k_{33} and k_{15} modes. Thus, additional samples with different polarization angle are needed. Another approach to separate the shear mode from the unwanted spurious peaks was indicated in the work in [86], which proposes to control the ratio of dimensions to improve the electro-mechanical coupling factor in the shear mode. A dimension optimization was conducted with changing the dimension ratios using a PZT-5A ceramic. Although the width (refer to Figure 3.1.3) does not influence the resonance and antiresonance frequencies of the shear mode, a suitable ratio of width-to-thickness or width-to-length is required to prevent mode coupling between the shear mode and unwanted modes. Combining the work into this dissertation, more reliable analysis on the anisotropic properties can be achieved. The width of each orientations with different polarization-canted angles can be controlled to separate the shear mode from the unwanted modes. Consequently, the effective shear properties for various polarization orientations could be measured and the reliability of the data could be improved. As a requisite, the dielectric permittivity should

be measured to assure consistent poling in different dimensions, especially for the rhombohedral PNZT which has the large permittivity anisotropy.

It is well known that the dielectric and piezoelectric constant is enhanced near the MPB due to the high degree of alignment and enhanced polarizability [57]. Using the proposed methodology in this dissertation, the anisotropic properties of the tetragonal, MPB and rhombohedral PNZT were obtained. An enhancement of the dielectric and piezoelectric constants could be observed in the MPB PNZT. However, the dielectric and piezoelectric losses in MPB PNZT showed an intermediate value between the losses in tetragonal and rhombohedral phases. A similar phenomenon for the dielectric properties was reported for a PZT ceramic by Takashi Yamamoto in [87], as shown in Figure 8.2.1. Here, the $\varepsilon_{33}^{T}/\varepsilon_0$ is the free dielectric permittivity after poling, ε_r the permittivity before poling, and tanδ the intensive dielectric loss. The author pointed out the different coercive field value for the tetragonal and rhombohedral phases. Small coercive field values result in a more compliant movements of domains by the applied electric field, which is accompanied by dielectric loss. A hypothesis can be made that the piezoelectric loss near the MPB is directly related to the content of tetragonal and rhombohedral phases. Additional PNZT samples with various PZ to PT ratio near MPB can be studied to verify the hypothesis. The intensity of XRD peaks should be studied to clarify the content of tetragonal and rhombohedral phases. It is necessary to consider the piezoelectric loss as a function of vibration modes. The changes of piezoelectric loss with respect to the PZ/PT ratio would be the largest in the k_{33} mode as indicated in Figure 6.3.3. It is also notable that the maximum d_{31} and d_{33} constants are known to occur in different PZ/PT ratios [88].

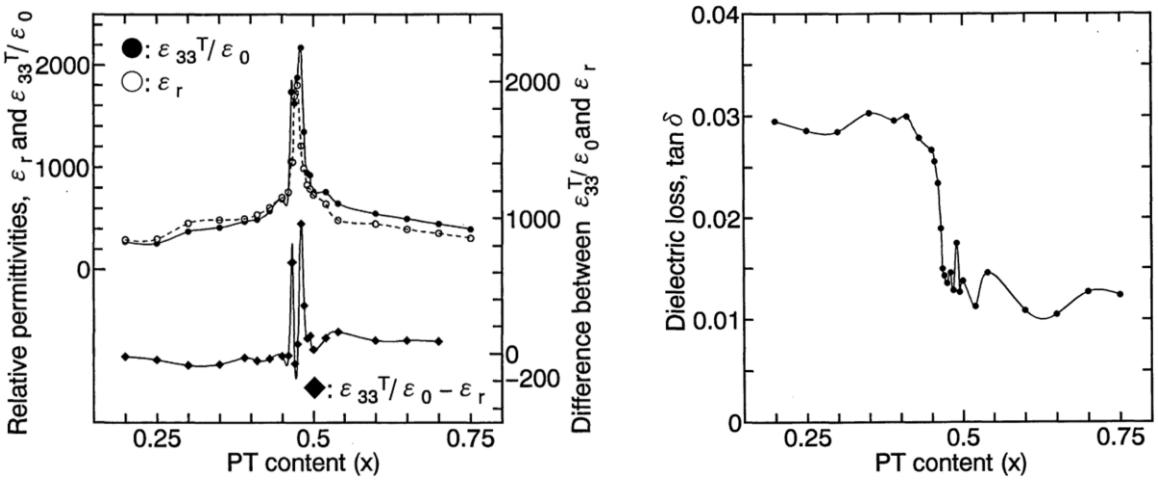

Figure 8.2.1. Compositional dependence of dielectric permittivity and the corresponding loss of a PZT ceramic reported in [87].

The loss factors analyzed in this dissertation is limited to the low power regime assuming no heat generation. However, it is essential to know the high-power characteristics to utilize the resonators in high-power devices such as ultrasonic motors or underwater transducers. It is challenging to characterize the high-power properties due to the changes in temperature [89]. Recently, a burst methodology was developed by Husain Shekhani et al. to separate the effects of the temperature rise and characterize the piezoelectric loss as a function of the vibration level [53]. A large excitation voltage is applied to the sample at its resonance frequency for a couple of cycles. Leaving the sample electrically short- or open-circuited, the oscillation rings down at the resonance or antiresonance frequencies. The signal decays of the current and vibration velocity can be measured in the short-circuited condition, which are proportional to each other. The signal decay of the voltage and vibration amplitude can be measured in the open-circuited condition, which are proportional to each other. Then, using the rates of signal decay, the loss factors can be analyzed with respect to the vibration level. Note that the few cycles of excitation doesn't induce heat generation in the system, thus the temperature rise can be neglected. Figure 8.2.2 shows the preliminary results on the Q_A of MPB PNZT in effective k_{31} mode. Similar to the result in section

6.3, the Q_A is minimum (the maximum intensive elastic loss) where the polarization angle is canted near 45 degrees at the high vibration level. The problem of this method is the large measurement error in the small vibration level. Thus, the data should be combined with results of the low-power characterization proposed in this dissertation. In addition, the large burst excitation can incur a possible change of the remanent polarization. Hence, the effective polarization should be checked before and after the measurement. The dielectric permittivity can be used for the analysis since it gradually changes from ε_{33} to ε_{11} depending on the effective polarization.

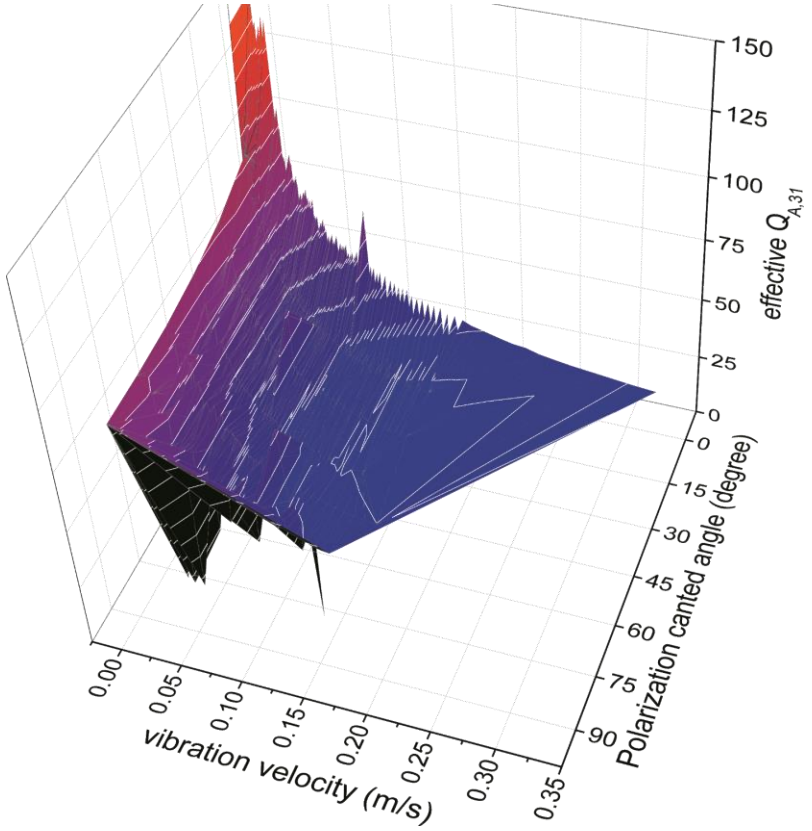

Figure 8.2.2. Changes of the effective Q_A with respect to the polarization-canted angle and vibration velocity measured with the burst method.

In Chapter 7, the extensive loss parameters in the effective k_{31} mode was calculated using the K matrix assuming $c_{11}^D=1/s_{11}^D$ near resonance frequency. The relation of elastic stiffness and

elastic compliance in k_{31} is shown in equation 8.2.1. Here, the elastic compliance s_{12} and s_{13} is an order smaller than s_{11} and s_{33}. Thus, the reciprocal relation can be assumed in the k_{31} mode.

$$c_{11} = \frac{s_{11}s_{33} - s_{13}^2}{s_{11}^2 s_{33} - s_{12}^2 s_{33} + 2s_{12}s_{13}^2 - 2s_{11}s_{13}^2} \approx \frac{1}{s_{11}} \tag{8.2.1}$$

The assumption was validated in [90], [91], with a PIC144 ceramic. A new methodology using a partially electroded k_{31} sample shown in Figure 8.2.3 was suggested to directly measure the extensive elastic loss in the k_{31} mode. A small portion of electrode, which is 10% of the total length, was applied in the center to mechanically actuate the ceramic. ATILA/GiD FEA simulations were conducted to verify that the partial electrode configuration is tolerably equivalent to the fully non-electroded condition. Using the sample, the extensive elastic loss could be calculated from the mechanical quality factor at the antiresonance frequency ($1/Q_{B,31}=\tan\phi_{11}$). The results showed good agreement to the parameters calculated with the *K* matrix using a standard k_{31} mode sample. Thus, the *K* matrix is applicable in the k_{31} vibration mode. Due to the boundary condition of the k_{33} mode, neither intensive nor extensive loss parameters can be directly measured. However, the intensive loss parameters of the k_{33} mode obtained in this dissertation is independent to the boundary condition of the standard k_{33} mode samples. It is notable that equation 8.2.2 could be assumed in the k_{33} mode.

$$c_{33} = \frac{s_{11} + s_{12}}{s_{11}s_{33} + s_{12}s_{33} - 2s_{13}^2} \approx \frac{1}{s_{33}} \tag{8.2.2}$$

An analytical review should be made to determine if the *K* matrix can be utilized to calculate the fundamental extensive loss parameters of the k_{33} mode. If possible, the complete set of extensive loss behaviors could be analyzed and aid the future study on piezoelectric loss mechanism.

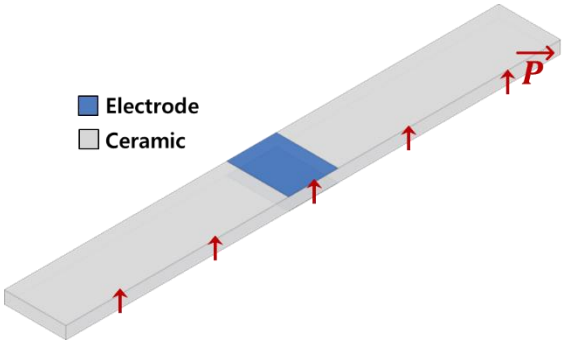

Figure 8.2.3. Partial electrode configurations of a k_{31} mode sample to directly obtain the extensive loss parameters.

Appendix A

Noise treatment for the electrical measurements

The electrical characterization in low power level induces large measurement error. 17 loops of wire was used to measure the small current more accurately. A wire holder is 3D-printed with nonconductive materials as shown in Figure A1.1 to support the wire loops. The improvements are shown in Figure A1.2.

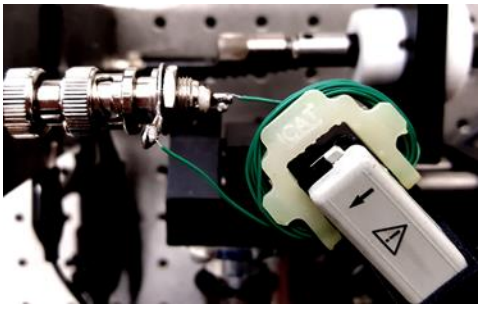

Figure A1.1. 3D-printed wire holder.

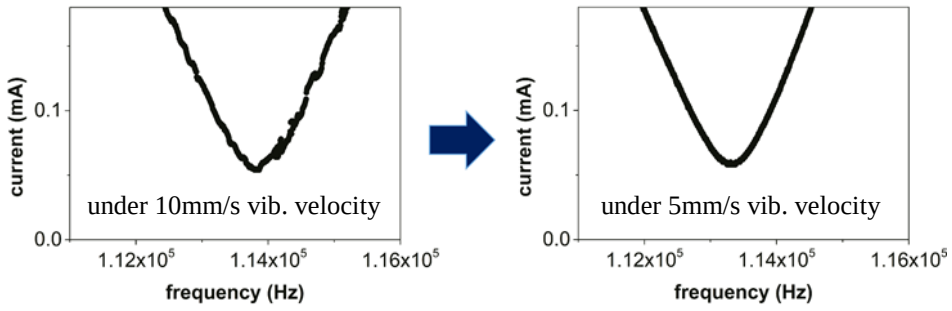

Figure A1.2. Improved current signal with the wire loops.

The measurement interval for effective k_{31} mode and effective k_{15} mode was set to 1Hz and 10Hz, respectively. Figure A1.3 shows an example of the VBA code to determine the resonance frequency and the corresponding half-power bandwidth. Cell G and H are filled with Conductance and Susceptance, respectively.

```
maxG_Y = Application.WorksheetFunction.max(ws.Range("G:G"))
maxB_Y = Application.WorksheetFunction.max(ws.Range("H:H"))
minB_Y = Application.WorksheetFunction.min(ws.Range("H:H"))


lrgG_Y = Application.WorksheetFunction.Large(ws.Range("G:G"), 50)
lrgB_Y = Application.WorksheetFunction.Large(ws.Range("H:H"), 50)
smlB_Y = Application.WorksheetFunction.Small(ws.Range("H:H"), 50)


'Res freq ############################################################
i = 1
For j = 2 To RowCount
If ws.Cells(j, 7) > lrgG_Y Then
Sheet2.Cells(i, 1) = ws.Cells(j, 1)
i = i + 1
End If
Next j
Sheet1.Cells(n, 2) = Application.Average(Sheet2.Range("A:A")) 'average 8.18.2017
Sheet2.Cells.Clear

i = 1
For j = 2 To RowCount
If ws.Cells(j, 8) < smlB_Y Then
Sheet2.Cells(i, 1) = ws.Cells(j, 1)
i = i + 1
End If
Next j
Sheet1.Cells(n, 3) = Application.Average(Sheet2.Range("A:A"))
Sheet2.Cells.Clear

i = 1
For j = 2 To RowCount
If ws.Cells(j, 8) > lrgB_Y Then
Sheet2.Cells(i, 1) = ws.Cells(j, 1)
i = i + 1
End If
Next j
Sheet1.Cells(n, 4) = Application.Average(Sheet2.Range("A:A"))
Sheet2.Cells.Clear
```

Figure A1.3. Part of VBA code used to calculate the quality factors.

Appendix B

Electro-mechanical coupling loss

Although the electro-mechanical coupling loss has not been introduced, there could be a possibility to consider it as the origin of losses in piezoelectricity. The electro-mechanical coupling loss is expressed with extensive loss parameters in equation 7.3.1. However, using equation 1.1.6, the coupling loss can be also introduced with the intensive loss parameters as:

$$\frac{k''}{k'} = \frac{2\tan\theta' - \tan\delta' - \tan\phi'}{2} \tag{A2.1}$$

Figure A2.1 is the polar plot of the coupling loss in effective k_{31} mode, showing the possible relation with crystal anisotropy.

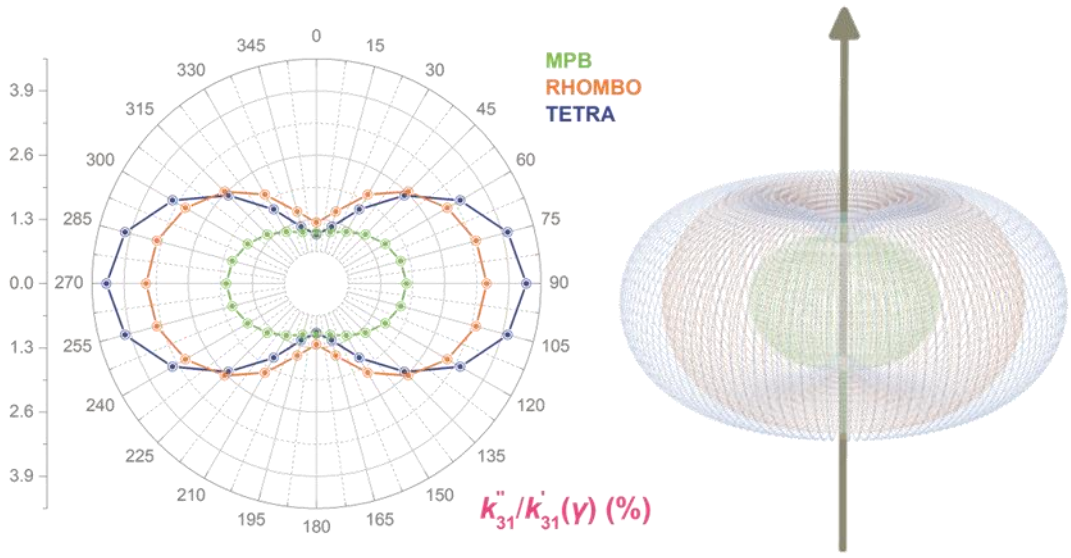

Figure A2.1. Electro-mechanical coupling loss in effective k_{31} mode.

Bibliography

[1] J. Curie and P. Curie, “Development, via compression, of electric polarization in hemihedral crystals with inclined faces,” *Bull. la Soc. Minerol. Fr.*, vol. 3, pp. 90–93, 1880.

[2] G. Lippmann, “On the principle of the conservation of electricity,” *London, Edinburgh, Dublin Philos. Mag. J. Sci.*, vol. 12, no. 73, pp. 151–154, 1881.

[3] S. Roberts, “Dielectric and piezoelectric properties of barium titanate,” *Phys. Rev.*, vol. 71, no. 12, pp. 890–895, 1947.

[4] B. Jaffe, R. S. Roth, and S. Marzullo, “Piezoelectric properties of lead zirconate-lead titanate solid-solution ceramics,” *J. Appl. Phys.*, vol. 25, no. 6, pp. 809–810, 1954.

[5] Y. Sugawara, K. Onitsuka, S. Yoshikawa, Q. Xu, R. E. Newnham, and K. Uchino, “Metal–ceramic composite actuators,” *J. Am. Ceram. Soc.*, vol. 75, no. 4, pp. 996–998, 1992.

[6] M. Umeda, K. Nakamura, and S. Ueha, “Energy storage characteristics of a piezo-generator using impact induced vibration,” *Jpn. J. Appl. Phys.*, vol. 36, no. 5S, pp. 3146–3151, 1997.

[7] J. K. Lee, J. Kim, C. J. Rhee, C. H. Jo, and S. B. Choi, “Noise reduction of passive and active hybrid panels,” *Smart Mater. Struct.*, vol. 11, no. 6, p. 940, 2002.

[8] P. Laoratanakul, A. Vázquez Carazo, P. Bouchilloux, and K. Uchino, “Unipoled disk-type piezoelectric transformers,” *Jpn. J. Appl. Phys.*, vol. 41, no. 3R, pp. 1446–1450, 2002.

[9] B. H. Son *et al.*, “Design of ultrasonic vibrator for conformal coating spray in LED packaging,” *Adv. Mater. Res.*, vol. 79, pp. 715–718, 2009.

[10] J. Jeon, S. M. Hong, M. Choi, and S. B. Choi, “Design and performance evaluation of a new jetting dispenser system using two piezostack actuators,” *Smart Mater. Struct.*, vol. 24, no. 1, p. 015020, 2015.

[11] Y. S. Kang, J. W. Lee, J. W. Kim, S. H. Han, and M. Choi, “Inertial sensor,” U.S. Patent 8,508,105 B2, 2013.

[12] "IEEE standard on piezoelectricity," *ANSI/IEEE Standard*. Institute of Electrical and Electronic Engineers, NY, p. 176, 1987.

[13] M. E. Lines and A. M. Glass, *Principles and applications of ferroelectrics and related materials*. New York: Oxford University Press, 1977.

[14] K. Uchino, *Ferroelectric devices 2nd edition*. New York: CRC Press, 2009.

[15] K. Uchirio and S. Hirosc, "Loss mechanisms in piezoelectrics: How to measure different losses separately," *IEEE Trans. Ultrason. Ferroelectr. Freq. Control*, vol. 48, no. 1, pp. 307–321, 2001.

[16] H. N. Shekhani and K. Uchino, "Characterization of mechanical loss in piezoelectric materials using temperature and vibration measurements," *J. Am. Ceram. Soc.*, vol. 97, no. 9, pp. 2810–2814, 2014.

[17] K. H. Härdtl, "Electrical and mechanical losses in ferroelectric ceramics," *Ceram. Int.*, vol. 8, no. 4, pp. 121–127, 1982.

[18] D. Damjanovic, "Ferroelectric, dielectric and piezoelectric properties of ferroelectric thin films and ceramics," *Reports Prog. Phys.*, vol. 61, pp. 1267–1324, 1998.

[19] G. Arlt and H. Dederichs, "Complex elastic, dielectric and piezoelectric constants by domain wall damping in ferroelectric ceramics," *Ferroelectrics*, vol. 29, no. 1, pp. 47–50, 1980.

[20] M. Hagiwara, T. Hoshina, H. Takeda, and T. Tsurumi, "Identicalness between piezoelectric loss and dielectric loss in converse effect of piezoelectric ceramic resonators," *Jpn. J. Appl. Phys.*, vol. 51, no. 9S1, p. 09LD10, 2012.

[21] R. E. Eitel, T. R. Shrout, and C. A. Randall, "Nonlinear contributions to the dielectric permittivity and converse piezoelectric coefficient in piezoelectric ceramics," *J. Appl. Phys.*, vol. 99, no. 12, p. 124110, 2006.

[22] S. Trolier-McKinstry, N. B. Gharb, and D. Damjanovic, “Piezoelectric nonlinearity due to motion of 180˚ domain walls in ferroelectric materials at subcoercive fields: A dynamic poling model,” *Appl. Phys. Lett.*, vol. 88, no. 20, p. 202901, 2006.

[23] R. Holland, “Representation of dielectric, elastic, and piezoelectric losses by complex coefficients,” *IEEE Trans. Sonics Ultrason.*, vol. 14, no. 1, pp. 18–20, 1967.

[24] S. Sherrit, H. D. Wiederick, and B. K. Mukherjee, “PdP135. Nun-iterative evaluation of the real and imaginary material constants of piezoelectric resonators,” *Ferroelectrics*, vol. 134, no. 1, pp. 111–119, 1992.

[25] G. Arlt, “The role of domain walls on the dielectric, elastic and piezoelectric properties of ferroelectric ceramics,” *Ferroelectrics*, vol. 76, no. 1, pp. 451–458, 1987.

[26] G. E. Martin, “Dielectric, elastic and piezoelectric losses in piezoelectric materials,” in *1974 Ultrasonics Symposium*, 1974, pp. 613–617.

[27] A. V. Mezheritsky, “Elastic, dielectric, and piezoelectric losses in piezoceramics: how it works all together,” *IEEE Trans. Ultrason. Ferroelectr. Freq. Control*, vol. 51, no. 6, pp. 695–707, 2004.

[28] T. Ikeda, *Fundamentals of piezoelectricity*. New York: Oxford University Press, 1990.

[29] T. Ikeda, “Mechanical loss and depolarizing field in a piezoelectric medium,” *Jpn. J. Appl. Phys.*, vol. 24, no. Supplement 24-1, pp. 3–6, 1985.

[30] D. Damjanovic, T. R. Gururaja, S. J. Jang, and L. E. Cross, “Temperature behavior of the complex piezoelectric d_{31} coefficient in modified lead titanate ceramics,” *Mater. Lett.*, vol. 4, no. 10, pp. 414–419, 1986.

[31] S. Hirose, Y. Yamayoshi, M. Taga, and H. Shimizu, “A method of measuring the vibration level dependence of impedance-type equivalent circuit constants,” *Jpn. J. Appl. Phys.*, vol. 30, no. 1, pp. 117–119, 1991.

[32] A. V. Mezheritsky, “Quality factor of piezoceramics,” *Ferroelectrics*, vol. 266, no. 1, pp. 277–304, 2002.

[33] D. Damjanovic, “An equivalent electric-circuit of a piezoelectric bar resonator with a large piezoelectric phase-angle,” *Ferroelectrics*, vol. 110, pp. 129–135, 1990.

[34] W. Shi, H. N. Shekhani, H. Zhao, J. Ma, Y. Yao, and K. Uchino, “Losses in piezoelectrics derived from a new equivalent circuit,” *J. Electroceramics*, vol. 35, no. 1–4, pp. 1–10, 2015.

[35] A. V. Mezheritsky, “Efficiency of excitation of piezoceramic transducers at antiresonance frequency,” *IEEE Trans. Ultrason. Ferroelectr. Freq. Control*, vol. 49, no. 4, pp. 484–494, 2002.

[36] H. Shekhani, W. Shi, M. Majzoubi, M. Choi, A. Bansal, and K. Uchino, “Should we drive transducers at their resonance frequency?,” *Proc. 15th Int. Conf. New Actuators (Actuator 2016)*, 2016, pp. 60–64.

[37] Y. Zhuang, S. O. Ural, A. Rajapurkar, S. Tuncdemir, A. Amin, and K. Uchino, “Derivation of piezoelectric losses from admittance spectra,” *Jpn. J. Appl. Phys.*, vol. 48, no. 4, p. 041401, 2009.

[38] K. Uchino, Y. Zhuang, and S. O. Ural, “Loss determination methodology for a piezoelectric ceramic : new phenomenological theory and experimental proposals,” *J. Adv. Dielectr.*, vol. 1, no. 1, pp. 17–31, 2011.

[39] Y. Zhuang, S. O. Ural, and K. Uchino, “Methodology for characterizing loss factors of piezoelectric ceramics,” *Ferroelectrics*, vol. 470, no. 1, pp. 260–271, 2014.

[40] J. Kuwata, K. Uchino, and S. Nomura, “Dielectric and piezoelectric properties of $0.91Pb(Zn_{1/3}Nb_{2/3})O_3$-$0.09PbTiO_3$ single crystals,” *Jpn. J. Appl. Phys.*, vol. 21, no. 9R, pp. 1298–1302, 1982.

[41] X. Du, J. Zheng, U. Belegundu, and K. Uchino, "Crystal orientation dependence of piezoelectric properties of lead zirconate titanate near the morphotropic phase boundary," *Appl. Phys. Lett.*, vol. 72, no. 19, pp. 2421–2423, 1998.

[42] X. Du, Q. Wang, U. Belegundu, and K. Uchino, "Piezoelectric property enhancement in polycrystalline lead zirconate titanate by changing cutting angle," *J. Ceram. Soc. Japan*, vol. 107, no. 1242, pp. 190–191, 1999.

[43] X. Du, Q. Wang, U. Belegundu, A. Bhalla, and K. Uchino, "Crystal orientation dependence of piezoelectric properties of single crystal barium titanate," *Mater. Lett.*, vol. 40, no. 3, pp. 109–113, 1999.

[44] T. Liu and C. S. Lynch, "Ferroelectric properties of [110], [001] and [111] poled relaxor single crystals: measurements and modeling," *Acta Mater.*, vol. 51, no. 2, pp. 407–416, 2003.

[45] R. Zhang, B. Jiang, and W. Cao, "Elastic, piezoelectric, and dielectric properties of multidomain $0.67Pb(Mg_{1/3}Nb_{2/3})O_3$-$0.33PbTiO_3$ single crystals," *J. Appl. Phys.*, vol. 90, no. 7, pp. 3471–3475, 2001.

[46] R. Zhang, B. Jiang, and W. Cao, "Superior d_{32}^* and k_{32}^* coefficients in $0.955Pb(Zn_{1/3}Nb_{2/3})O_3$-$0.045PbTiO_3$ and $0.92Pb(Zn_{1/3}Nb_{2/3})O_3$-$0.08PbTiO_3$ single crystals poled along [011]," *J. Phys. Chem. Solids*, vol. 65, no. 6, pp. 1083–1086, 2004.

[47] X. Huo *et al.*, "Complete set of elastic, dielectric, and piezoelectric constants of $[011]_C$ poled rhombohedral $Pb(In_{0.5}Nb_{0.5})O_3$-$Pb(Mg_{1/3}Nb_{2/3})O_3$-$PbTiO_3$:Mn single crystals," *J. Appl. Phys.*, vol. 113, no. 7, p. 074106, 2013.

[48] S. Zhang, N. P. Sherlock, R. J. Meyer, and T. R. Shrout, "Crystallographic dependence of loss in domain engineered relaxor-PT single crystals," *Appl. Phys. Lett.*, vol. 94, no. 16, pp. 110–112, 2009.

[49] J. L. Jones, “The use of diffraction in the characterization of piezoelectric materials,” *J. Electroceramics*, vol. 19, no. 1, pp. 69–81, 2007.

[50] T. L. Jordan and Z. Ounaies, “Piezoelectric Ceramics Characterization,” *Inst. Comput. Appl. Sci. Eng. Hampt. VA*, no. 2001–28, 2001.

[51] P. J. Petersan and S. M. Anlage, “Measurement of resonant frequency and quality factor of microwave resonators: comparison of methods,” *Journal of Applied Physics*, vol. 84, no. 6. pp. 3392–3402, 1998.

[52] S. Priya, D. Viehland, A. V. Carazo, J. Ryu, and K. Uchino, “High-power resonant measurements of piezoelectric materials: Importance of elastic nonlinearities,” *J. Appl. Phys.*, vol. 90, no. 3, pp. 1469–1479, 2001.

[53] H. Shekhani, T. Scholehwar, E. Hennig, and K. Uchino, “Characterization of piezoelectric ceramics using the burst/transient method with resonance and antiresonance analysis,” *J. Am. Ceram. Soc.*, vol. 100, no. 3, pp. 998–1010, 2017.

[54] A. Mezheritsky, “Q-factor spectrum of a piezoceramic resonator and method for piezoelectric loss factor determination,” *IEEE Trans. Ultrason. Ferroelectr. Freq. Control*, vol. 64, no. 12, pp. 1849–1856, 2017.

[55] H. Daneshpajooh, H. N. Shekhani, M. Choi, and K. Uchino, “New methodology for determining the dielectric constant of a piezoelectric material at the resonance frequency range,” *J. Am. Ceram. Soc.*, vol. 101, no. 5, pp. 1940–1948, 2018.

[56] B. Jaffe, R. S. Roth, and S. Marzullo, “Properties of piezoelectric ceramics in the solid-solution series lead titanate-lead zirconate-lead oxide: tin oxide and lead titanate-lead hafnate,” *J. Res. Natl. Bur. Stand. (1934).*, vol. 55, no. 5, pp. 239–254, 1955.

[57] B. Jaffe, W. R. Cook, and H. Jaffe, “Piezoelectric ceramics,” London and New York: Academic Press, 1971.

[58] D. A. Berlincourt, C. Cmolik, and H. Jaffe, “Piezoelectric properties of polycrystalline lead titanate zirconate compositions,” *Proc. IRE*, vol. 48, no. 2, pp. 220–229, 1960.

[59] G. Robert, “Extrinsic contributions to the piezoelectric response of lead-based ferroelectrics,” Ecole polytechnique fédérale de Lausanne, 2001.

[60] D. Berlincourt, “Recent developments in ferroelectric transducer materials,” *IRE Trans. Ultrason. Eng.*, vol. PGUE-4, pp. 53–65, 1956.

[61] M. Marutake and T. Ikeda, “Anisotropy in polarized barium titanate ceramics,” *J. Phys. Soc. Japan*, vol. 12, no. 3, pp. 233–240, 1957.

[62] M. E. Drougard and D. R. Young, “Domain clamping effect in barium titanate single crystals,” *Phys. Rev.*, vol. 94, no. 6, p. 1561, 1954.

[63] M. Choi, K. Uchino, E. Hennig, and T. Scholehwar, “Polarization orientation dependence of piezoelectric losses in soft lead zirconate-titanate ceramics,” *J. Electroceramics*, vol. 40, no. 1, pp. 16–22, 2018.

[64] E. Heinonen, J. Juuti, and S. Leppävuori, “Characterization and modelling of 3D piezoelectric ceramic structures with ATILA software,” *J. Eur. Ceram. Soc.*, vol. 25, no. 12, pp. 2467–2470, 2005.

[65] Y. Zuo-Guang, *Handbook of advanced dielectric, piezoelectric and ferroelectric materials*. Cambridge: Woodhead Publishing Limited, 2008.

[66] W. Jiang, R. Zhang, B. Jiang, and W. Cao, “Characterization of piezoelectric materials with large piezoelectric and electro-mechanical coupling coefficients,” *Ultrasonics*, vol. 41, no. 2, pp. 55–63, 2003.

[67] M. Choi, T. Scholehwar, E. Hennig, and K. Uchino, “Crystallographic approach to obtain intensive elastic parameters of k_{33} mode piezoelectric ceramics,” *J. Eur. Ceram. Soc.*, vol. 37, no. 15, pp. 5109–5112, 2017.

[68] N. Aurelle, D. Guyomar, C. Richard, P. Gonnard, and L. Eyraud, “Nonlinear behavior of an ultrasonic transducer,” *Ultrasonics*, vol. 34, no. 2–5, pp. 187–191, 1996.

[69] S. O. Ural, S. Tuncdemir, Y. Zhuang, and K. Uchino, “Development of a high power piezoelectric characterization system and its application for resonance/antiresonance mode characterization,” *Jpn. J. Appl. Phys.*, vol. 48, no. 5R, p. 056509, 2009.

[70] H. B. Miller, “Handbook for the Analysis of Piezoelectric Transducers (Using Electrical Equivalent Circuits). Part 1. The Untuned Transducer,” *Nav. Underw. Syst. Cent. new London ct.*, no. NUSC-TD-6029-PT-1, 1978.

[71] Y. Roh, V. V. Varadan, and V. K. Varadan, “Characterization of all the elastic, dielectric, and piezoelectric constants of uniaxially oriented poled PVDF films,” *IEEE Trans. Ultrason. Ferroelectr. Freq. Control*, vol. 49, no. 6, pp. 836–847, 2002.

[72] H. Al-Budairi, M. Lucas, and P. Harkness, “A design approach for longitudinal-torsional ultrasonic transducers,” *Sensors Actuators, A Phys.*, vol. 49, no. 6, pp. 836–847, 2013.

[73] T. Meurisse and D. Damjanovic, “Modeling losses of a piezoelectric resonator: analytical vs finite elements analysis,” *Proc. 2017 Joint IEEE ISAF/ IWATMD/PFM*, pp. 71-74, 2017.

[74] E. Hafner, “The piezoelectric crystal unit - definitions and methods of measurement,” *Proc. IEEE*, vol. 57, no. 2, pp. 179–201, 1969.

[75] M. Kim, J. Kim, and W. Cao, “Aspect ratio dependence of electro-mechanical coupling coefficient of piezoelectric resonators,” *Appl. Phys. Lett.*, vol. 87, no. 13, p. 132901, 2005.

[76] M. Kim, J. Kim, and W. Cao, “Experimental technique for characterizing arbitrary aspect ratio piezoelectric resonators,” *Appl. Phys. Lett.*, vol. 89, no. 16, p. 162910, 2006.

[77] J. Fialka and P. Beneš, “Measurement of piezoelectric ceramic parameters: A characterization of the elastic, dielectric and piezoelectric properties of NCE51 PZT,” *Proc. ICCC*, pp. 147–152, 2012.

[78] D. Berlincourt, H. A. Krueger, and C. Near, “Properties of Morgan electro ceramic ceramics,” *Morgan Electro Ceramics*, Report No. TP-226, 1959.

[79] I. Franke, K. Roleder, L. Mitoseriu, R. Piticescu, and Z. Ujma, “High-temperature macroscopic piezoelectricity in Nb-doped $PbZr_{1-x}Ti_xO_3$ ceramics driven by the existence of polar regions,” *Phys. Rev. B*, vol. 73, no. 14, p. 144114, 2006.

[80] I. Lazar, M. Adamczyk-Habrajska, M. Pawełczyk, M. Górny, A. Zawada, and K. Roleder, “Piezoelectric and elastic properties of relaxor-like PZT:Ba ceramics,” *J. Electroceramics*, vol. 40, pp. 203–210, 2018.

[81] M. Algueró, C. Alemany, L. Pardo, and A. M. González, “Method for obtaining the full set of linear electric, mechanical, and electro-mechanical coefficients and all related losses of a piezoelectric ceramic,” *J. Am. Ceram. Soc.*, vol. 87, no. 2, pp. 209–215, 2004.

[82] Y. Zhuang, S. O. Ural, S. Tuncdemir, A. Amin, and K. Uchino, “Analysis on loss anisotropy of piezoelectrics with ∞ mm crystal symmetry,” *Jpn. J. Appl. Phys.*, vol. 49, no. 2R, p. 021503, 2010.

[83] K. Uchino *et al.*, “Loss mechanisms and high power piezoelectrics,” *J. Mater. Sci.*, vol. 41, no. 1, pp. 217–228, 2006.

[84] G. Bertotti and I. D. Mayergoyz, *The Science of Hysteresis vol. III*. Gulf Professional Publishing, 2006.

[85] A. V. Turik and G. S. Radchenko, “Maxwell-Wagner relaxation in piezoactive media,” *J. Phys. D. Appl. Phys.*, vol. 35, no. 11, pp. 1188–1192, 2002.

[86] L. Qin, J. Jia, M. Choi, and K. Uchino, “Improvement of electro-mechanical coupling coefficient in shear-mode of piezoelectric ceramics,” *Ceram. Int.*, p. In Press: https://doi.org/10.1016/j.ceramint.2018., 2018.

[87] T. Yamamoto, “Ferroelectric properties of the $PbZrO_3$–$PbTiO_3$ system,” *Jpn. J. Appl. Phys.*, vol. 35, no. 9B, pp. 5104–5108, 1996.

[88] R. Steinhausen *et al.*, “Properties of fine scale piezoelectric PZT fibers with different Zr content,” *J. Eur. Ceram. Soc.*, vol. 21, no. 10–11, pp. 1459–1462, 2001.

[89] S. Takahashi, Y. Sasaki, M. Umeda, K. Nakamura, and S. Uhea, “Characteristics of piezoelectric ceramics at high vibration levels,” *MRS Online Proc. Libr. Arch.*, vol. 604, pp. 15–24, 1999.

[90] M. Majzoubi, H. N. Shekhani, A. Bansal, E. Hennig, T. Scholehwar, and K. Uchino, “Advanced methodology for measuring the extensive elastic compliance and mechanical loss directly in k_{31}mode piezoelectric ceramic plates,” *J. Appl. Phys.*, vol. 120, no. 22, p. 225113, 2016.

[91] X. Dong *et al.*, “A new equivalent circuit for piezoelectrics with three losses and external loads,” *Sensors Actuators, A Phys.*, vol. 256, pp. 77–83, 2017.

VITA

Minkyu Choi

Minkyu Choi was born in Busan, Republic of Korea. He received his B.S. in Materials Science and Engineering at Korea University in 2007. At the end of his junior year, he joined the Electro-ceramics Laboratory in Korea University to study synthesis of lead-free piezoelectric ceramics. He continued his graduate study in the lab under Dr. Sahn Nahm's supervision and received his M.Sc in Advanced Materials Science and Engineering in 2009 with a thesis entitled "Piezoelectric Properties of CuO-Added $[(Na_{0.5}K_{0.5})_{1-x}Li_x](Nb_{0.96}Sb_{0.04})O_3$ Lead-free Piezoelectric Ceramics". In February 2009, he was employed by Protec (Korea) as an assistant research engineer. He worked on developing dispenser head system with piezoelectric module. Then, he moved to Samsung Electro-mechanics (Korea) in October 2010, as a research engineer. He worked on developing a 6-axis inertial MEMS sensor for mobile phone application using piezoelectric thin films.

Starting from August 2013, he got a chance to work in the International Center for Actuators and Transducers, MRI as a visiting researcher. After a semester, he began his doctorate degree in Materials Science and Engineering at the Pennsylvania State University under the guidance of Dr. Kenji Uchino. He initially worked on abnormal cut single crystal transformers. He proposed an oval-shaped electrode design to enhance both power density and efficiency of the ring-dot transformer. However, he pointed out the large loss factors in abnormal cut single crystals and pursued the study on polarization dependence of losses. As a result, he has published several journal articles on piezoelectric loss and characterization method. One of his paper was honored as a Key Scientific Article by Advances in Engineering in May 2018. In May 2016, he got the student poster award in "2016 International Workshop on Acoustic Transduction Materials and Devices" held in State College. In May 2018, he got the Robert E. Newnham Award for research excellence, granted by the Penn State Materials Science and Engineering department.